OPEN-OCEAN CONVECTION: OBSERVATIONS, THEORY, AND MODELS

John Marshall
Department of Earth, Atmospheric, and Planetary Sciences
Massachusetts Institute of Technology, Cambridge

Friedrich Schott
Institut für Meereskunde an der Universität Kiel
Kiel, Germany

Abstract. We review what is known about the convective process in the open ocean, in which the properties of large volumes of water are changed by intermittent, deep-reaching convection, triggered by winter storms. Observational, laboratory, and modeling studies reveal a fascinating and complex interplay of convective and geostrophic scales, the large-scale circulation of the ocean, and the prevailing meteorology. Two aspects make ocean convection interesting from a theoretical point of view. First, the timescales of the convective process in the ocean are sufficiently long that it may be modified by the Earth's rotation; second, the convective process is localized in space so that vertical buoyancy transfer by upright convection can give way to slantwise transfer by baroclinic instability. Moreover, the convective and geostrophic scales are not very disparate from one another. Detailed observations of the process in the Labrador, Greenland, and Mediterranean Seas are described, which were made possible by new observing technology. When interpreted in terms of underlying dynamics and theory and the context provided by laboratory and numerical experiments of rotating convection, great progress in our description and understanding of the processes at work is being made.

CONTENTS

1. INTRODUCTION

1.1. Background and Scope

The strong vertical density gradients of the thermocline of the ocean inhibit the vertical exchange of fluid and fluid properties between the surface and the abyss, insulating the deep ocean from variations in surface meteorology. However, in a few special regions (see Figure 1) characterized by weak stratification and, in winter, exposed to intense buoyancy loss to the atmosphere, violent and deep-reaching convection mixes surface waters to great depth, setting and maintaining the properties of the abyss. This paper reviews observational, modeling, laboratory, and theoretical studies that have elucidated the physics of the convective process and its effect on its larger-scale environment.

In the present climate, open-ocean deep convection occurs only in the Atlantic Ocean: the Labrador, Greenland, and Mediterranean Seas (Figure 1), and occasion-

Reviews of Geophysics, 37, 1 / *February 1999*
pages 1–64
8755-1209/99/98RG-02739$15.00
Paper number 98RG02739

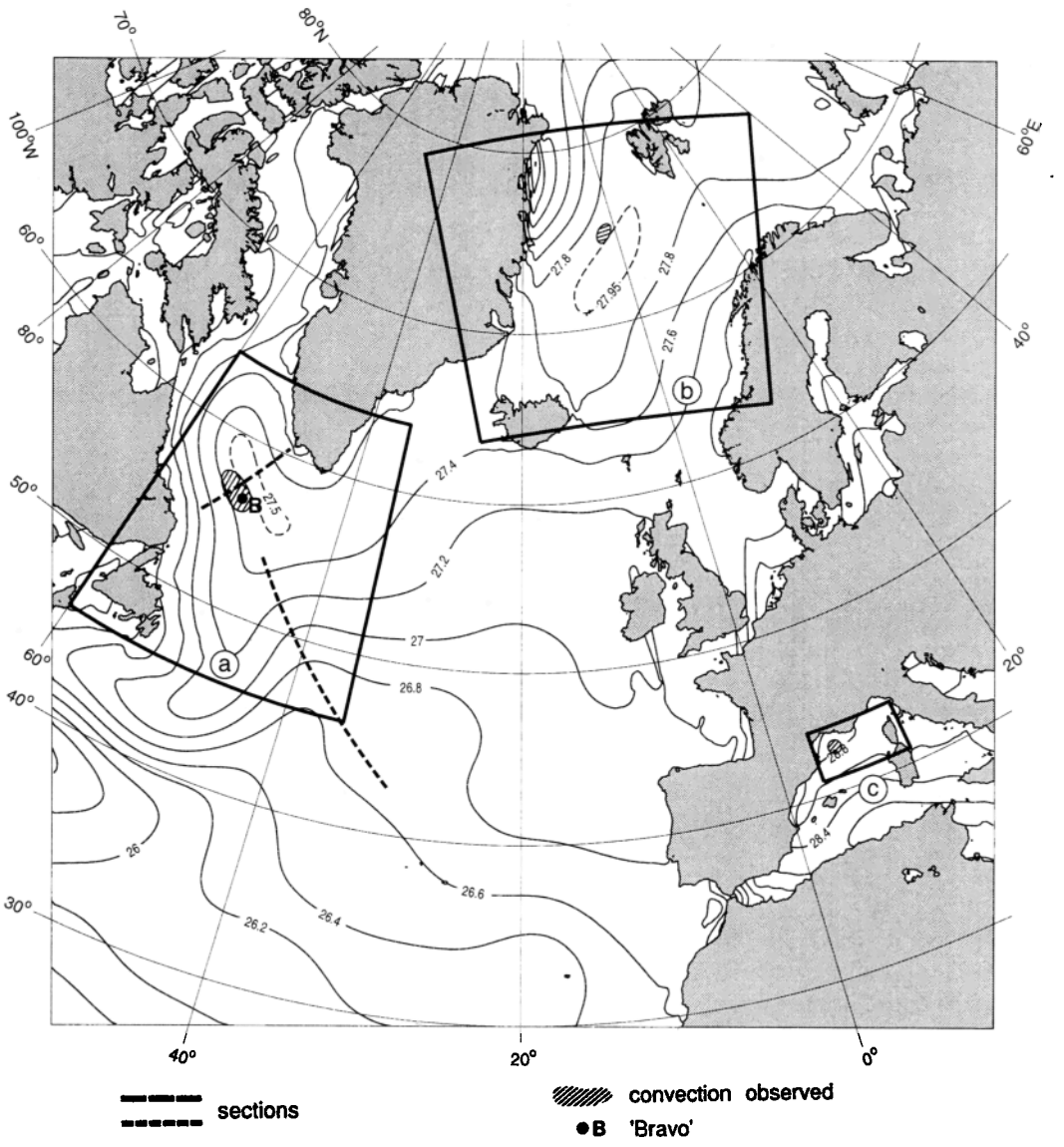

Figure 1. The major deep convection sites of the North Atlantic sector: the Labrador Sea (box a), the Greenland Sea (box b), and the western Mediterranean (box c). Detailed descriptions and discussions of the water mass transformation process occurring in the three "boxes" are reviewed here. To indicate the preconditioned state of early winter, the potential density at a depth of 100 m is shown for November from the climatological data of *Levitus et al.* [1994b] and *Levitus and Boyer* [1994]. Deep-reaching convection has been observed in the shaded regions.

ally also in the Weddell Sea [see *Gordon*, 1982]. Convection in these regions feeds the thermohaline circulation, the global meridional-overturning circulation of the ocean responsible for roughly half of the poleward heat transport demanded of the atmosphere-ocean system [see *Macdonald and Wunsch*, 1996]. Warm, salty water is drawn poleward, becomes dense in polar seas, and then sinks to depth and flows equatorward. Water masses modified by deep convection in these small regions are tagged with temperature and salinity values characteristic of them (together with other tracers such as tritium from the atomic weapon tests and freons from industrial and household use), allowing them to be tracked far from their formation region.

Geologists speculate about possible North Pacific Deep Water formation in past climates (for example, see *Mammerickx* [1985]). There is some evidence for enhanced convection in the North Pacific at the last glacial maximum (the ^{14}C age reduction observed by *Duplessy et al.* [1989], for example). However, the patterns of evidence are contradictory, and as yet, there is no consensus [see *Keigwin*, 1987; *Curry et al.*, 1988; *Boyle*, 1992; *Adkins and Boyle*, 1997].

In this review we discuss the dynamics of the water mass transformation process itself, and its effect on the stratification and circulation of its immediate environment. Some of the relevant fluid mechanics, that of convection in "open" domains, is reviewed by *Maxworthy*

[1997]. Our scope here is more specifically oceanographic and similar to that of *Killworth* [1983]. Since Killworth's review, however, there has been much progress in our understanding of the kinematics and dynamics of ocean convection through new results from field experiments, through focused laboratory experiments, and through numerical simulation. We bring things up to date and draw together threads from new observations, theory, and models.

Observations of the processes involved in open-ocean deep convection began with the now classical Mediterranean Ocean Convection (MEDOC) experiment in the Gulf of Lions, northwestern Mediterranean [*MEDOC Group*, 1970]. Rapid (in a day or so) mixing of the water column down to 2000 m was observed. Strong vertical currents, of the order of 10 cm s^{-1}, associated with convective elements were observed for the first time [*Stommel et al.*, 1971]. Observations of convection prior to MEDOC were limited to descriptions of hydrostatic changes and timescales estimated from changes in the inventory of water mass properties. Since MEDOC, and particularly in the past decade, new technologies have led to different kinds of observations and deeper insights into the processes at work. Moored acoustic Doppler current profilers (ADCPs) were deployed in a convection regime over a winter period to document the three-dimensional (3-D) currents occurring in conjunction with deep mixing. From a first ADCP experiment, *Schott and Leaman* [1991] determined the existence of small-scale plumes during an intense cooling phase in the Gulf of Lions convection regime. The downward velocities in these plumes ranged up to 10 cm s^{-1}, and the horizontal plume scale was only about 1 km. Subsequently, experiments in the Greenland Sea [*Schott et al.*, 1993] and again in the Gulf of Lions [*Schott et al.*, 1996] substantiated the existence, scales, and physical role of the plumes. These recent observations of plumes (reviewed in detail in section 3) have served to narrow down the time and space scales involved in water mass transformation and the nature of the processes at work.

Along with, and in large part inspired by these new observations, there has been renewed interest in laboratory and numerical studies of rotating convection [see *Jones and Marshall*, 1993; *Maxworthy and Narimousa*, 1994]. Two aspects make ocean convection interesting from a theoretical point of view. First, the timescales of the convective process in the ocean are sufficiently long that it may be modified by the Earth's rotation; second, the convective process is localized in space so that vertical buoyancy transfer by upright convection can give way to slantwise transfer by baroclinic instability. Laboratory and numerical studies of rotating convection motivated by the oceanographic problem have led to advances in our understanding of the general problem (see section 3). Numerical experiments are presented in this review in the same spirit as those in the laboratory except that a numerical fluid is used rather than a real one. Both approaches have their limitations. Unless extraordinary measures are taken, only Rayleigh numbers in the range 10^9–10^{16} are attainable in the laboratory or in the computer, compared with 10^{26} in the ocean [see *Whitehead et al.*, 1996]. However, when laboratory and numerical experiments have been used in concert and scaled for comparison with the observations, they have led to great insight.

It is interesting to note how little the developments that will be described here have been influenced by "classical convection studies" that trace their lineage back to "Rayleigh-Benard" convection [*Rayleigh*, 1916; *Benard*, 1900]. In the ocean the Rayleigh number in convecting regions is many orders of magnitude greater than the critical value, and the convection is fully turbulent with transfer properties that do not depend, we believe, on molecular viscosities and diffusivities (see section 3.3). Even more importantly, the convective process in the ocean is localized in space, making it distinct from the myriad classical studies of convection rooted in the Rayleigh problem (convection between two plates extending laterally to $\pm\infty$). As one might anticipate, edge effects and baroclinic instability come to dominate the evolving flow fields and, as described in section 4, are a distinctive and controlling factor in ocean convection.

Finally, one of the goals of the research reviewed here is to improve the parametric representation of convection in large-scale models used in climate research, in which one cannot, and does not wish to, explicitly resolve the process. Such models are used to study the general circulation of the ocean and, when coupled to atmospheric models, the climate of the Earth. Thus in section 5 we review progress being made in that area. Concluding remarks are made in section 6.

1.2. Some Preliminaries

The ocean is, in most places and at most times, a stably stratified fluid driven at its upper surface by patterns of momentum and buoyancy flux associated with the prevailing winds. The buoyancy force acting on a water parcel in a column is determined by its anomaly in buoyancy:

$$b = -g(\rho'/\rho_0) \tag{1}$$

where g is the acceleration due to gravity and

$$\rho' = \rho - \rho_{amb}$$

is the difference in the density of the particle relative to that of its surroundings, ρ_{amb}, and ρ_0 is a constant reference density equal to 1000 kg m^{-3}. In the ocean, complications arise because the density of seawater can depend in subtle ways on (potential) temperature ϑ, salinity S, and pressure p [see *Veronis*, 1972]:

$$\rho = \rho(\vartheta, S, p) \tag{2}$$

However, often in theoretical studies a simplified equation of state is adopted of the form:

TABLE 1. Typical Values of α_ϑ and β_S as a Function of Potential Temperature ϑ, Salinity S, and Pressure p for Seawater

	Labrador Sea	*Greenland Sea*	*Mediterranean Sea*
	Surface		
ϑ_0, °C	3.4	−1.4	13.7
α_ϑ, $\times 10^{-4}$ K^{-1}	0.9	0.3	2.0
S_0, psu	34.83	34.88	38.35
β_S, $\times 10^{-4}$ psu^{-1}	7.8	7.9	7.6
	Depth of 1 km		
ϑ_0, °C	2.7	−1.2	12.8
α_ϑ, $\times 10^{-4}$ K^{-1}	1.2	0.7	2.3
S_0, psu	34.84	34.89	38.4
β_S, $\times 10^{-4}$ psu^{-1}	9.0	9.2	8.5

See equation (3).

$$\rho = \rho_0[1 - \alpha_\vartheta(\vartheta - \vartheta_0) + \beta_S(S - S_0)] \quad (3)$$

where α_ϑ and β_S are thermal expansion and haline contraction coefficients, respectively, and ϑ_0 and S_0 are reference temperature and salinities. Typical values of α_ϑ and β_S are given in Table 1 as a function of ϑ_0, S_0, and pressure. To the extent that they can be taken as constant, the governing equations can be entirely reformulated in terms of a buoyancy variable and buoyancy forcing. However, particularly at low temperatures the thermal expansion coefficient varies strongly with ϑ and p; it becomes smaller at lower temperatures and increases with depth, especially in the Greenland Sea (see the middle column of Table 1). The excess acceleration of a parcel resulting from the increase in α with depth, the thermobaric effect (see section 3.7), can result in a destabilization of the water column if the displacement of a fluid parcel (as a result of gravity waves, turbulence, or convection) is sufficiently large. Thermobaric effects may be an important factor, particularly in the Greenland and Weddell Seas.

The vertical stability of the water column is given by the Brunt-Väisälä frequency

$$N^2 = \partial b/\partial z \quad (4)$$

a measure of the frequency of internal gravity waves. In stably stratified conditions, $N^2 > 0$; if $N^2 < 0$, convective overturning ensues. Profiles of N typical of the convection sites (together with ϑ and S) are shown in Figure 2. It is useful to normalize N by $f_0 = 10^{-4}$ s^{-1}, a typical value of the Coriolis parameter, a measure of the frequency of inertial waves. We see that N is positive at all levels in the column, that N/f falls to about 5 in the deep ocean, but that in the near surface layers N/f can exceed 100. In the upper kilometer of the ocean, N/f is 30–50, corresponding to a gravity wave period of 30 min or so and a gravity wave phase speed of a few meters per second.

The distance a gravity wave travels in an inertial period, as measured by the Rossby radius of deformation, is given by

$$L_\rho = NH/f_0 \quad (5)$$

where H is the depth of the ocean. In the northern North Atlantic, L_ρ takes on a mean value of 10 km or so [e.g., see *Emery et al.*, 1994]. In deep convection sites where, as a result of recurring convection, the ambient stratification is much reduced, L_ρ is as small as a few kilometers and sets the scale of the often vigorous geostrophic eddy field that is commonly observed. At scales greater than L_ρ the Earth's rotation controls the dynamics and

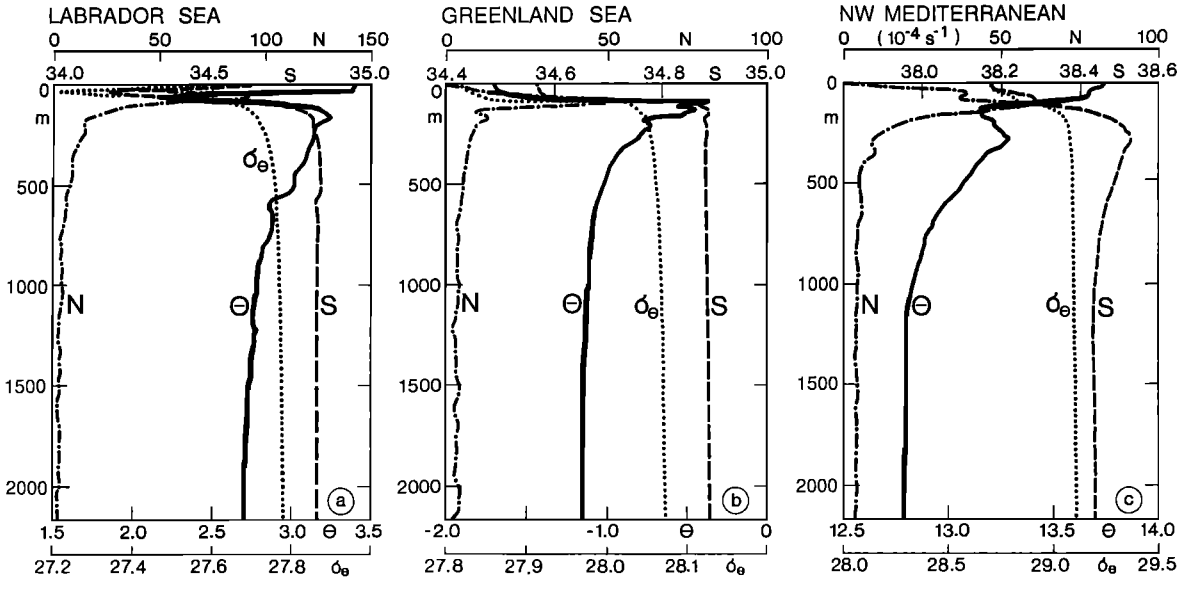

Figure 2. Climatological profiles of potential temperature, salinity, potential density, and Brunt-Väisälä frequency from the convection sites shown in Figure 1. (a) Labrador Sea, station *Bravo*. (b) Greenland Sea, near 75°N, 5°W. (c) Gulf of Lions, near 42°N, 5°E.

geostrophic balance pertains. On scales much smaller than L_ρ, however, balanced dynamics break down (see *Marshall et al.* [1997a] for a discussion of the breakdown of the hydrostatic approximation).

The surface layers of the ocean are stirred by the winds and undergo a regular cycle of convection and restratification in response to the annual cycle of buoyancy fluxes at the sea surface (see the detailed discussion in section 2.3). The buoyancy flux is expressed in terms of heat and fresh water fluxes as

$$\mathcal{B} = \frac{g}{\rho_0}\left(\frac{\alpha_\vartheta}{c_w}\mathcal{H} + \rho_0\beta_S S(E-P)\right) \qquad (6)$$

where c_w is the heat capacity of water (3900 J Kg^{-1} K^{-1}), $\mathcal{H}$ is the surface heat loss, and $E - P$ represents the net fresh water flux (evaporation minus precipitation). The magnitude of the buoyancy flux $\mathcal{B}$ plays an important role in the development of dynamical ideas presented in this review; it has units of meters squared per second cubed, that of a velocity times an acceleration. Over the interior of the ocean basin, heat fluxes rise to perhaps 100 W m^{-2} in winter, and $E - P$ is perhaps 1 m yr^{-1}, implying a buoyancy flux of $\sim 10^{-8}$ m^2 s^{-3}. For stratification typical of the upper regions of the main thermocline, mixed layers do not reach great depth when exposed to buoyancy loss of these magnitudes, perhaps to several hundred meters or so (see the contours of winter mixed-layer depth in the North Atlantic presented by *Marshall et al.* [1993]). At the convection sites shaded in Figure 1, however, the stratification is sufficiently weak, $N/f \approx 5$–10, and the buoyancy forcing is sufficiently strong, often greater than 10^{-7} m^2 s^{-3}, corresponding to heat fluxes as high as 1000 W m^{-2}, that convection may reach much greater depths, sometimes greater than 2 km. This review is concerned with the dynamical processes that occur in these special regions, which result in the transformation of the properties of large volumes of fluid and set the properties of the abyssal ocean.

In section 2 we review the observational background; each convection site has its own special character, but we emphasize common aspects that are indicative of mechanism. In section 3 we discuss the convective process itself, and in section 4 we discuss the dynamics of the resulting homogeneous volumes of water. Finally, in section 5, we discuss how one might parameterize the water mass transformation process in large-scale models.

2. OBSERVATIONAL BACKGROUND

2.1. Phases and Scales of Deep Convection

Observations of deep convection in the northwestern Mediterranean, the most intensively studied site (see, for example, the *MEDOC Group* [1970], *Gascard* [1978], and *Schott and Leaman* [1991]), suggest that the convective process is intermittent and involves a hierarchy of scales. Three phases can be identified and are sketched schematically in Figure 3: "preconditioning" on the large-scale (order of 100 km), "deep convection" occurring in localized, intense plumes (on scales of the order of 1 km), and "lateral exchange" between the convection site and the ambient fluid through advective processes (on a scale of a few tens of kilometers). The last two phases are not necessarily sequential and often occur concurrently.

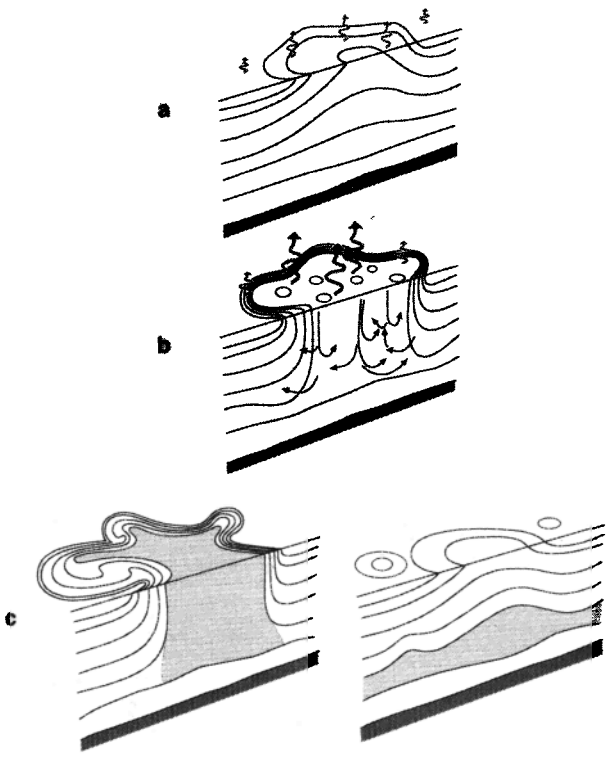

Figure 3. Schematic diagram of the three phases of open-ocean deep convection: (a) preconditioning, (b) deep convection, and (c) lateral exchange and spreading. Buoyancy flux through the sea surface is represented by curly arrows, and the underlying stratification/outcrops is shown by continuous lines. The volume of fluid mixed by convection is shaded.

During preconditioning (Figure 3a) the gyre-scale cyclonic circulation with its "doming" isopycnals, brings weakly stratified waters of the interior close to the surface. The potential density at a depth of 100 m in a November climatology is contoured in Figure 1, showing the preconditioned state over the North Atlantic. Buoyancy forcing associated with the prevailing meteorology then triggers convection. As the winter season sets in, vigorous buoyancy loss erodes the near-surface stratification of the cyclonic dome, over an area of perhaps several hundred kilometers across, exposing the very weakly stratified water mass beneath directly to the surface forcing [*Swallow and Caston*, 1973]. Subsequent cooling events may then initiate deep convection in which a substantial part of the fluid column overturns in numerous plumes (Figure 3b) that distribute the dense surface water in the vertical. The plumes have a horizontal scale of the order of their lateral scale, $\leq$1 km,

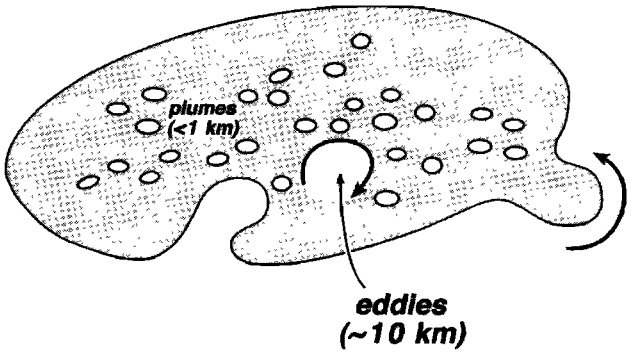

Figure 4. Lateral scales of the key phenomena in the water mass transformation process: the mixed patch on the preconditioned scale created by plumes together with eddies that orchestrate the exchange of fluid and properties between the mixed patch and the stratified fluid of the periphery. The fluid being mixed is shaded; the stratified fluid is unshaded.

with vertical velocities of up to 10 cm s^{-1} [*Schott and Leaman*, 1991; *Schott et al.*, 1996]. In concert the plumes are thought to rapidly mix properties over the preconditioned site, forming a deep "mixed patch" ranging in scale from several tens of kilometers to >100 km in diameter. (The *MEDOC Group* [1970] called the mixed patch a "chimney," a name that is still in common use today. However, the analogy between a deep mixed patch and a chimney is misleading because, as we shall see, there is very little vertical mass flux within the patch. For this reason we prefer not to use the name chimney.)

With the cessation of strong forcing, or if the cooling continues for many days, the predominantly vertical heat transfer on the convective scale gives way to horizontal transfer associated with eddying on geostrophic scales [*Gascard*, 1978] as the mixed patch laterally exchanges fluid with its surroundings (see Figure 3c). Individual eddies tend to organize the convected water in to coherent lenses in geostrophic balance. The mixed fluid disperses under the influence of gravity and rotation, spreading out at its neutrally buoyant level and leading, on a timescale of weeks to months, to the disintegration of the mixed patch and reoccupation of the convection site by the stratified fluid of the periphery. The hierarchy of processes and scales involved in the water mass transformation process are summarized in Figure 4.

2.2. Major Ocean Convection Sites

The observations suggest that there are certain features and conditions that predispose a region to deep-reaching convection. First, there must be strong atmospheric forcing because of thermal and/or haline surface fluxes. Thus open-ocean regions adjacent to boundaries are favored, where cold and dry winds from land or ice surfaces blow over water, inducing large sensible heat, latent heat and moisture fluxes. Second, the stratification beneath the surface-mixed layer must be weak (made weak perhaps by previous convection). And third, the weakly stratified underlying waters must be brought up toward the surface so that they can be readily and directly exposed to intense surface forcing. This latter condition is favored by cyclonic circulation associated with density surface, which "dome up" to the surface (see Figures 3a and 1).

Whether and when deep convection then occurs depends on the seasonal development of the surface buoyancy flux with respect to the initial stratification at the beginning of the winter period and on the role of lateral advection. Not only is the integral buoyancy supply important, but so is its timing. An integral buoyancy loss that may have resulted in deep convection when concentrated in a few intense winter storms may not yield deep mixed layers if distributed evenly over the winter months. In the latter case, lateral advection may have time to draw stratified water into the potential convection site from the periphery and stabilize it.

It is perhaps not surprising, then, that as the instrumental record of the interior ocean lengthens, it is becoming clear that deep-water formation is not a steady state process that recurs every year with certainty and regularity. The intensity of convection shows great variability from one year to the next and from one decade to another [see *Dickson et al.*, 1996].

We now briefly review the main features of the three major open-ocean convection regimes: the Mediterranean, Greenland and Labrador Seas.

2.2.1. Labrador Sea. The cyclonic circulation of the Labrador near-surface circulation is set by the West Greenland Current and the Labrador Current, shallow currents carrying cold, low-salinity water around the Labrador Sea (Figure 5). Below, higher-salinity Irminger Sea Water enters in the north on a cyclonic path, as is indicated schematically in Figure 5. The doming of the upper layer, as expressed in the topography of the σ_ϑ = 27.5 surface, is also shown in Figure 5. In the southeast, the northwestern loop of the North Atlantic Current transports warm water past the exit of the Labrador Sea. It is associated with a deepening of the σ_ϑ = 27.5 isopycnal of some 300 m toward the southeast, and it occasionally sheds eddies that leave their water mass properties in the region. Below 3000 m the deep western boundary current (DWBC), supplied in the main by Denmark Strait overflow waters, passes through the Labrador Sea steered by topography.

The stratification of the preconditioned state is three-layered (a vertical profile at ocean weather ship *Bravo* is shown in Figure 2a, and a salinity section is shown in Figure 6). The surface layer is fresh, perhaps the result of lateral eddy transport from the shallow boundary currents on the periphery (see section 4.4). Below, at ~200–700 m, Irminger Sea Water causes a weak interim temperature and salinity maximum (Figure 2a), stronger in the northern than the southern Labrador Sea (Figure 6). Underneath, down to 2000 m, there is a layer of near-homogeneous Labrador Sea Water (LSW), formed in previous winter convection, which recirculates in the western basin (Figure 6). The bottom is covered by cold

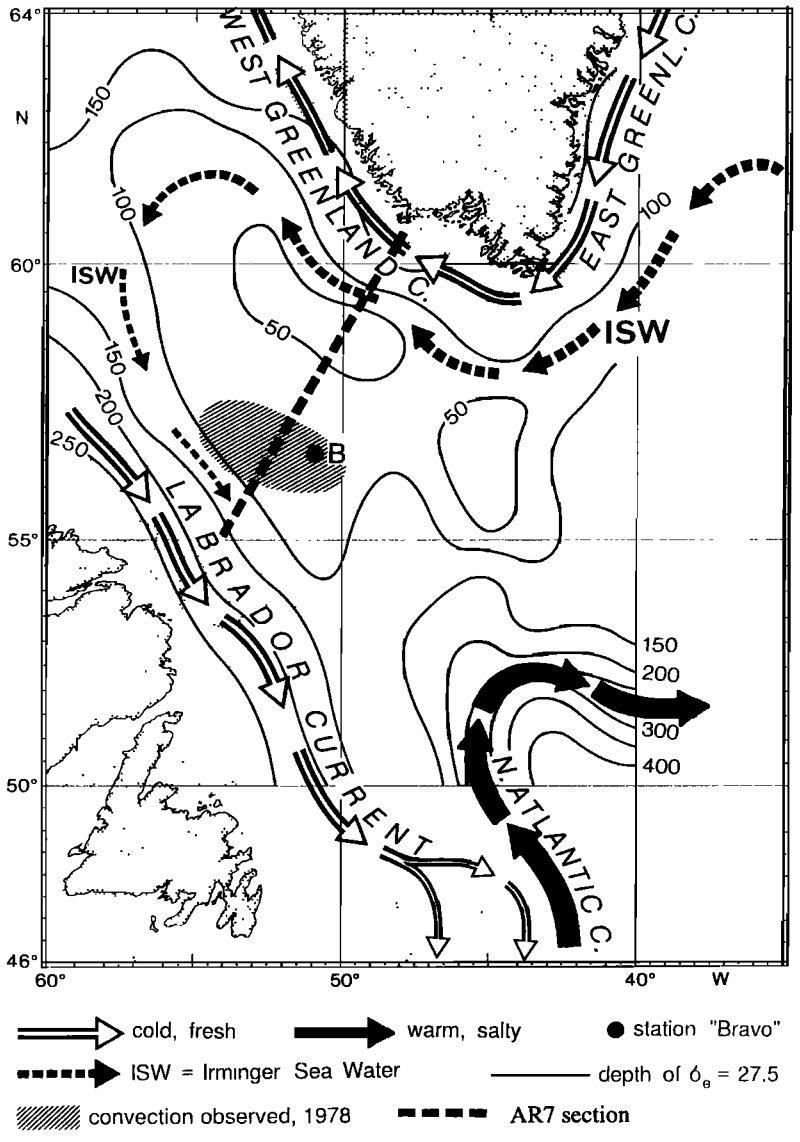

Figure 5. Circulation schematic showing the cyclonic circulation and preconditioning of the Labrador Sea convection regime. The depth of the σ_θ = 27.5 isopycnal in the early winter is contoured in meters. The warm circulation branches of the North Atlantic Current and Irminger Sea Water (ISW), and the near-surface, cold, and fresh East/West Greenland and Labrador Currents are also indicated. The position of *Bravo* is labeled "B." It is important to emphasize that this is a circulation schematic; in reality, the circulation is highly time dependent and comprises a vigorous eddy field on the deformation radius (~7 km).

and relatively fresh Denmark Strait Overflow Water that circulates cyclonically around the Labrador Sea, leaning against the deep topographic slope. At 2500–3200 m an intermediate salinity maximum (also apparent in Figure 6 far out into the Atlantic) is indicative of water from the Gibbs Fracture Zone with Eastern Basin Mediterranean Water admixtures.

Deep convection in the central Labrador Sea in late winter has been deduced from the continuous hydrographic observations of weather ship *Bravo* [*Lazier*, 1973] and observed in the shaded region in Figure 5 by *Clarke and Gascard* [1983]. The "products" of deep convection are evident in Figure 7, which shows data from a hydrographic section taken during summer 1990, running through *Bravo*, across the Labrador Sea to Greenland. We see an extensive mixed patch of fluid extending down to a depth of 2 km, presumably stirred by convection in the previous winter, but "capped" at the surface by a shallow stratified layer of a few hundred meters in depth. However, little is known about the lateral extent of the convection regime during the convective process itself, at the height of winter. The central Labrador Sea is ice-free in winter, and so ice and brine release probably do not play a primary role in the generation of deep convection. However, the ice plays an indirect role because it is carried into the preconditioning cyclonic flow, either from the East Greenland Current or through the Barents Sea, and may modify the preconditioning stability (Figure 6).

The water masses entering the upper part of the DWBC suggest a second Labrador Sea source, located in the vicinity of the southwestern margin [*Pickart*, 1992]. Its high anthropogenic tracer content relative to LSW suggests that this water mass drains into the DWBC more quickly than the LSW, where it forms the shallowest layer. Direct evidence for its formation, however, has not yet been found.

Water masses formed in the Labrador Sea can be traced in to the North Atlantic at depths down to 2000 m. The salinity minimum created in Labrador Sea

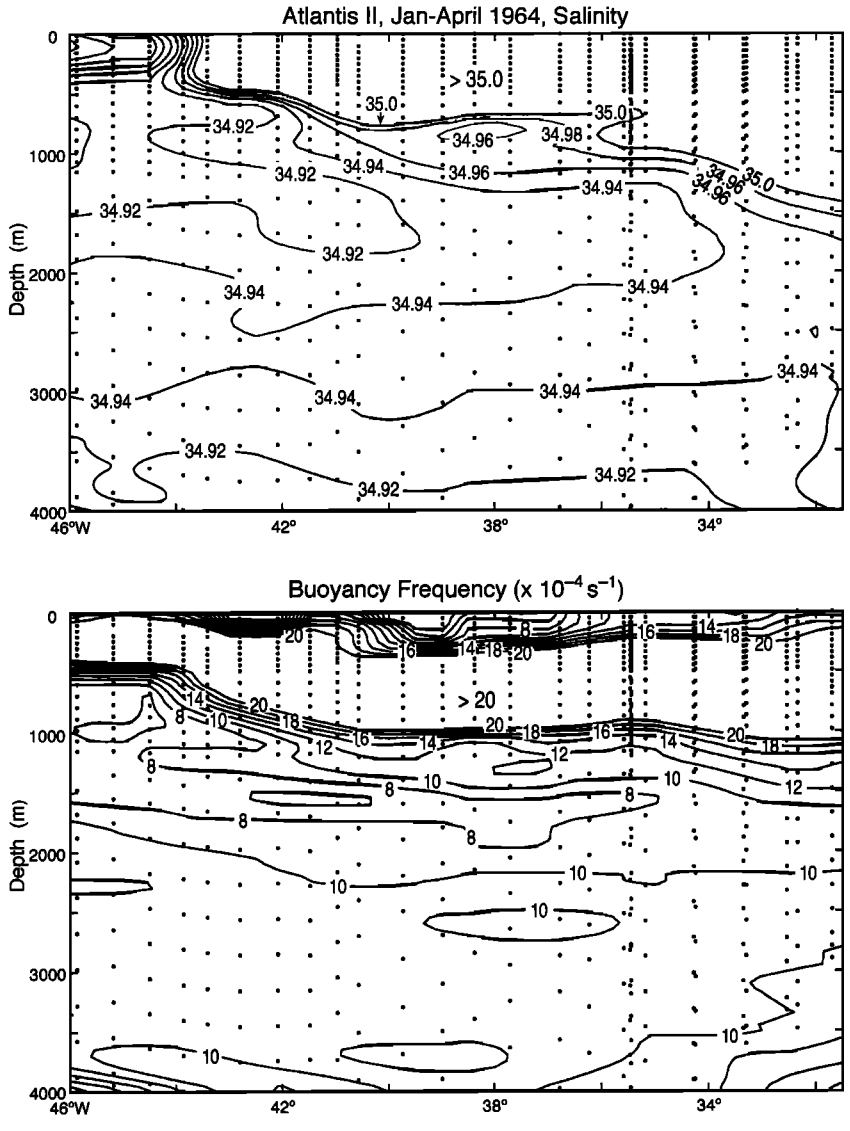

Figure 6. (top) Salinity distribution and (bottom) Brunt-Väisälä frequency, N along a section made by *Atlantis II* in February 1964, running from the exit of the Labrador Sea to the central North Atlantic (as marked in Figure 1). The section reveals a minimum of salinity and stability in the depth range 1100–1800 m, a consequence of Labrador Sea convection.

convection can be seen sliding down from approximately 1200 to 1800 m along the extent of the section in Figure 6. Toward the east, salinity increases as a result of the influence of Mediterranean waters. The core of the salinity minimum is marked by low stability of only about $N \approx 5f$ and correspondingly low potential vorticity [*Talley and McCartney*, 1982].

Finally, it should be emphasized that the properties of Labrador Sea Water are far from constant [see *Lazier*, 1988, 1995; *Dickson et al.*, 1996]. It appears that LSW was cold and fresh at the start of the century, characteristic of the then prevailing cold conditions. After warming through the 1930s, LSW reached its twentieth century extreme in the early 1970s. Since then we have seen increasingly intense winters, and the ϑ-S trajectory of LSW has moved toward colder, fresher conditions, yet nearly without change in potential density! The early 1990s presented us with, once again, wonderfully deep convection, which appears now to be on the wane (mixed layers only reached a few hundred meters in the winter of 1998). At the end of the twentieth century the system resembles the Labrador Sea of the beginning of the century [see *LabSea Group*, 1998].

2.2.2. Greenland Sea. The Greenland Sea has aspects in common with other convecting seas but also differs because of the important role of ice in preconditioning. The warm water branch of the cyclonic circulation in the Greenland Sea (Figure 8) is composed of the northward flow of warm, saline Atlantic Water in the Norwegian-Atlantic Current that sends branches westward into the interior and then continues as the Spitsbergen Current through Fram Strait into the Arctic Ocean. The southward flow of cold, fresh water out of the Arctic Ocean is carried by the East Greenland Current, which sends an eastward branch out into the interior, the Jan Mayen Current along the Jan Mayen Ridge, and a second branch further south, the East Iceland Current. The cyclonic circulation is associated with doming indicated in Figure 8 by the depth of the $\sigma_\vartheta = 27.9$ surface; it rises from >200 m at the periphery to <50 m in the central Greenland Sea. The stratification in the center (Figure 2b) is three-layered: on top, there is a thin

layer of Arctic Surface Water originating from the East Greenland Current. Underneath, a layer of Atlantic Intermediate Water exists supplied from the southeast, below which resides the weakly stratified Greenland Sea Deep Water, the product of previous convection events.

The role of ice appears to be decisive in the preconditioning of Greenland Sea convection: in early winter the ice first spreads eastward across the central Greenland Sea, and brine rejection under the ice increases the surface layer density [*Roach et al.*, 1993]. The mixed layer under the ice cools to the freezing temperature of -1.9°C and deepens by about 1 m d^{-1} [*Schott et al.*, 1993] to about 150 m in mid-January. Later in the winter season, typically late January, the ice forms a wedge (the Is Odden [*Vinje*, 1977; *Wadhams et al.*, 1996]) extending far out toward the northeast, and enclosing an ice-free bay, the "Nord Bukta" (Figure 8). This ice-free bay is thought to be largely a result of southward ice export that is due to strong northerly winds [*Visbeck et al.*, 1995].

Preconditioning continues through February with mixed-layer deepening in the Nord Bukta, to 300–400 m, induced by strong winds that blow over the ice. Finally, typically in March, preconditioning is far enough advanced that deep convection in the Nord Bukta may develop when the meteorological conditions are favorable. However, during the past decade, deep convective activity in the Greenland Sea was weak, so this sequence of events is based on the evidence of only a few occurrences. The lateral scale of deep, mixed regimes in the Greenland Sea appears to be coupled to that of the Is Odden. Only once, in 1988, has a mixed patch been observed [*Sandven et al.*, 1991] when the Is Odden was closed. When observations of convection were available in the past decade, convection went down only to ~1500-m depth [*Rudels et al.*, 1989; *Schott et al.*, 1993]. However, tracer evidence [*Smethie et al.*, 1986] indicates that deep water (>2000 m) ventilation of the Greenland Sea from the surface must have occurred at previous times.

2.2.3. Northwestern Mediterranean. The cyclonic circulation around the northwestern Mediterranean basin, marked schematically in Figure 9, originates as boundary currents on both sides of Corsica [*Astraldi and Gasparini*, 1992] and follows the topography westward as the Northern Mediterranean Current, feeding into the Catalan Current east of Spain. South of the dome there is sluggish eastward flow, marked by the Baleares Front during part of the year [*Millot*, 1987].

The water mass distribution in the western Mediterranean comprises three layers (Figure 2c). At the surface the water is of modified Atlantic type, originating from the inflow through the Strait of Gibraltar. At 150- to 500-m depth a warm, salty layer is found, Levantine Intermediate Water (LIW). LIW is formed by shallow convection in the eastern Mediterranean Basin and then slowly propagates into the western basin through the Strait of Sicily. Below the LIW layer, the basin is filled with near-homogeneous Western Mediterranean Deep

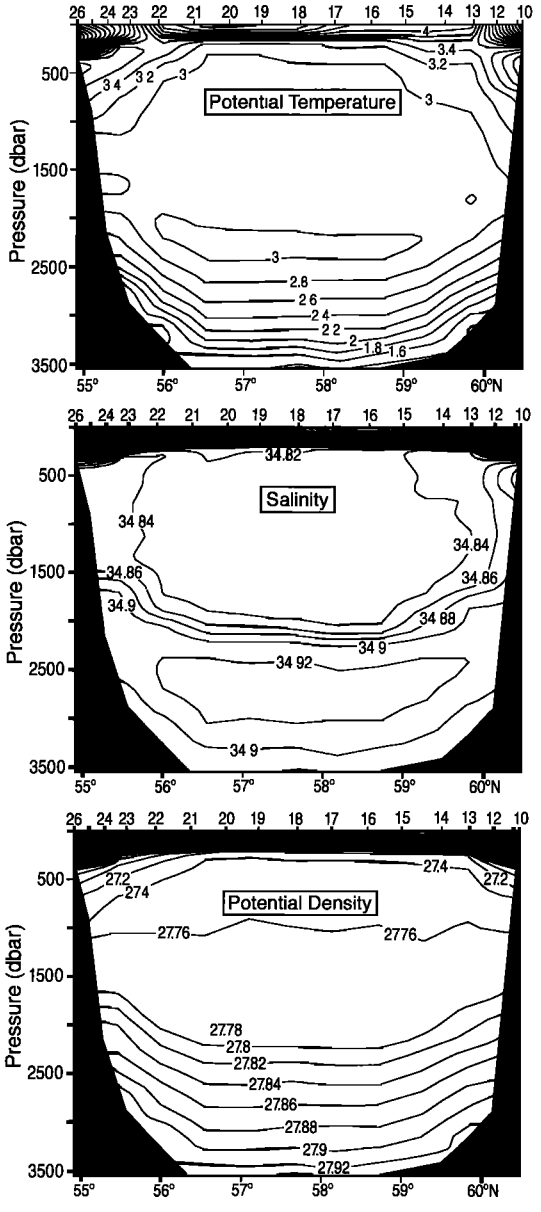

Figure 7. Sections of (top) potential temperature, (middle) salinity, and (bottom) potential density along the section in the Labrador Sea marked in Figure 5. Data from R/V *Dawson*, July 1990. Courtesy of Bedford Institute of Oceanography (A. Clarke, personal communication).

Water (WMDW). The cyclonic circulation of the region is indicated by the doming of the $\sigma_\vartheta = 28.8$ isopycnal as derived from historical data (Figure 9). The cyclonic circulation has maximum transport in winter and is thought to be largely driven by the curl of the wind stress [e.g., *Heburn*, 1987]. The winter transport maximum could also be a consequence of widespread cooling, inducing density gradients that enhance the baroclinic cyclonic flow. Similarly, enhanced coastal fresh water input in late winter can further enhance density gradients and thence cyclonic flow. There are two strong, cold, dry offshore winds in winter: the tramontane originating from the Pyrenees to the northwest, and the

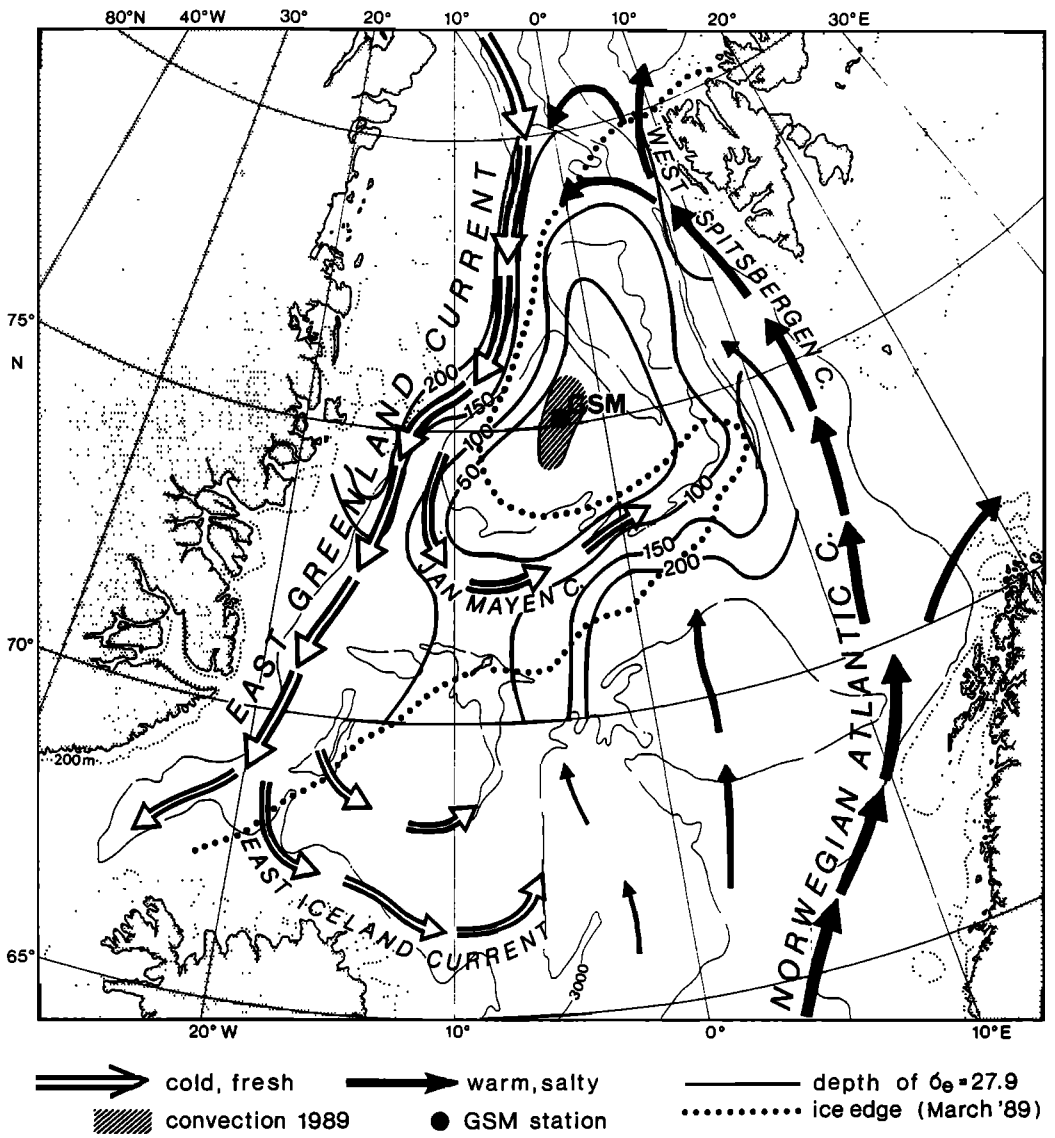

Figure 8. Schematic of the circulation of the Greenland Sea, showing the warm water flow of the Norwegian Atlantic Current and its recirculation, and cold water flows of the East Greenland Current and Jan Mayen Current that constitute the cyclonic circulation. Doming is indicated by the depth of isopycnal σ_θ = 27.9, and the Is Odden is marked by the position of the ice edge (dotted) in March 1989 (see text for details). "GSM" is the location of repeated moored deployments.

mistral, blowing out of the Rhone valley. The center of the preconditioning dome (Figure 9) lies directly in the path of the mistral, and tramontane outbursts can reach there also. An additional factor that might help localize the preconditioned dome may be the generation of Taylor columns over the "Rhone fan," a topographic feature protruding from the continental slope far out in to the Gulf of Lions [*Hogg*, 1973].

Typically, the integrated heat loss over the course of winter has erased the buoyancy of the surface layer by about mid-February. The horizontal extent of mixed patches for 1969, 1987, and 1992 are marked in Figure 9. They were all observed during the second half of February. However, in 1987 an earlier strong mistral on January 10–11 had already induced a first deep convection event [*Leaman and Schott*, 1991], which was in the process of being "capped" (see section 4.4) when the mid-February mistral triggered deep convection a second time. Figure 10 shows the doming in the density distribution along a meridional section through the Gulf of Lions during preconditioning of winter 1991–1992 convection and the homogeneous patch throughout the upper 1500 m after the onset of deep convection in February 1992. The near-surface density gradients at the northern and southern limits of the patch indicate the presence of a rim current around it [*Schott et al.*, 1996], as is discussed in section 4.4.

Convection to somewhat shallower depths occasionally occurs in the elongated dome to the east of the Gulf of Lions, as was recently reported by *Sparnocchia et al.*

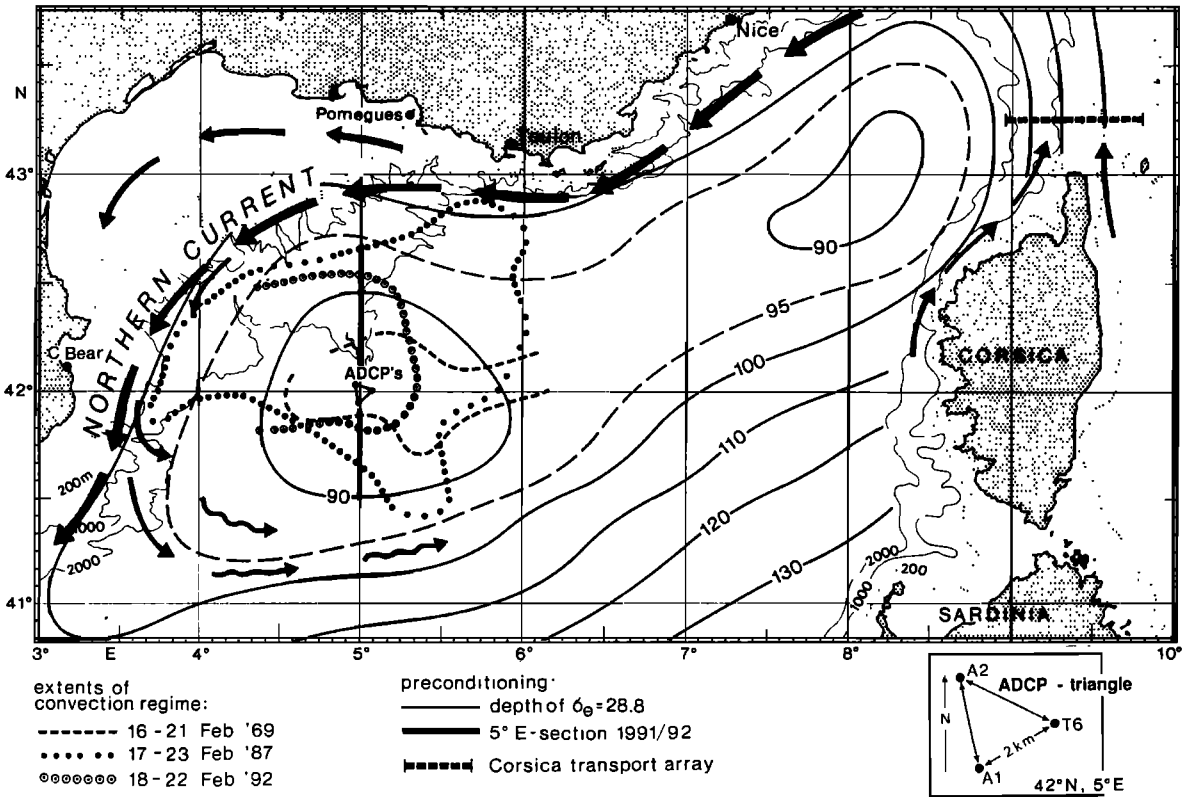

Figure 9. Circulation and convection conditions of the northwestern Mediterranean. Shown are depths of the isopycnal surface σ_θ = 28.8 kg m^{-3} (courtesy G. Krahmann) for the beginning of winter, indicating the cyclonic doming; the resulting boundary circulation by schematic current vectors, including the weaker offshore branching to the southwest; and extents of deep mixed patches as observed in February 1969 (dashed), 1987 (large dots), and 1992 (circled small dots). Also marked are positions of the triangular array of moored ADCP stations (see also inset) and of the repeated 5°E section.

[1995]. Reanalyzing data from the MEDOC 1969 experiment, they determined deep mixing down to 1200 m in the Ligurian Sea, southeast of Nice, and from moored instruments found convection depths between 500 and 800 m in the winter of 1991–1992.

Interannual variability of convection in the Gulf of Lions has been observed since the first convection experiments: 1969, the year of the first MEDOC experiment [*MEDOC Group*, 1970], was a year of strong convection, but 1971 was not [*Gascard*, 1978]. Vigorous deep convection (to 2200 m) returned in 1987, causing a very homogeneous water body of σ_θ = 12.79°C, S = 38.45 psu (practical salinity units) [*Leaman and Schott*, 1991]. Convection in 1991 did not reach as deep (only to 1700 m), nor did it mix the water column as thoroughly.

2.3. Meteorological Forcing

Direct measurements of air-sea fluxes are difficult to obtain. One way to estimate them is by using climatological formulae applied to routine meteorological observations. Latent and sensible heat fluxes are determined from bulk formulae that involve wind speed and air-sea moisture and temperature difference, respectively. Long- and short-wave radiative fluxes can also be estimated using climatological formulae and measurements of sea surface temperature and cloud cover. In the central Labrador Sea these standard observations were available for several decades from weather ship *Bravo*, until it was withdrawn in 1974. Since then, time series of even a minimal set of meteorological parameters have rarely been available, with the notable exception of the Labrador Sea Deep Convection Experiment [see *LabSea Group*, 1998].

Even when standard meteorological observations are available, the derived fluxes are sensitive to the choice of parameterization. *Smith and Dobson* [1984] applied coefficients tuned to conditions in the central Labrador Sea and found that the annual mean heat loss at station *Bravo* was 70 W m^{-2}, or about 60% smaller than that obtained by, for example, *Bunker* [1976] using global bulk parameters. Such large differences may significantly contribute to uncertainties about the evaluation of mixed-layer models in describing the development of deep convection.

Much profitable use can now be made of the vastly improved fluxes derived from meteorological operational models. European Centre for Medium-Range Weather Forecasts (ECMWF) analyzed fields have

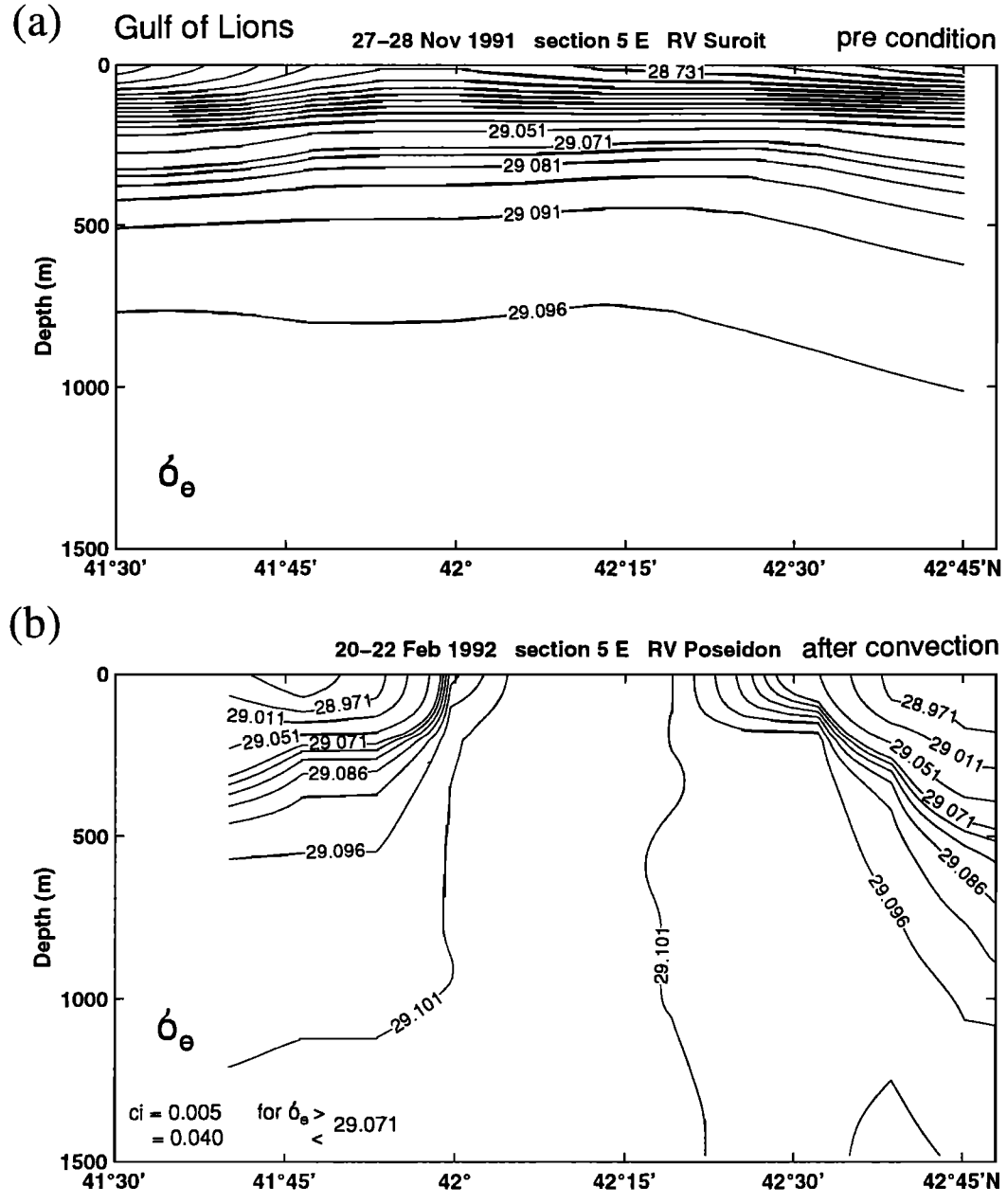

Figure 10. Meridional sections along 5°E through the Gulf of Lions convection regime (see Figure 9 for location): (a) November 27–28, 1991, preconditioning; (b) February 20–22, 1992, after deep convection to 1500 m.

proved to be very useful in the interpretation of observations of Labrador Sea and Greenland Sea convection. In the northwestern Mediterranean, fluxes of the French model Prévision à Echéance Rapprochée Integrant des Données Observées et Télédétectées (PERIDOT) have been evaluated and found to be of good quality when compared with estimates from research vessel observations using bulk formulae [e.g., *Mertens*, 1994]. Some relevant observations and model data are now briefly summarized; fluxes typical of individual deep convection cases described elsewhere in this paper are presented in Tables 2a and 2b, where estimates of corresponding buoyancy fluxes are also included.

2.3.1. Labrador Sea. In winter months, cold, dry air streams out of the arctic over the relatively warm surface waters of the Labrador Sea. Large fluxes of sensible and latent heat result from the strong winds and large air-sea temperature contrasts associated with these outbreaks. Over the region the magnitude and distribution of the fluxes are modulated by both synoptic-scale and mesoscale weather systems [*LabSea Group*, 1998]. The strong northwesterly flow that occurs after the passage of an extratropical cyclone can result in heat fluxes as large as 700 W m^{-2}. One also often observes the development of short-lived polar lows in the region.

TABLE 2a. Heat and Buoyancy Fluxes During Specific Convection Events in the Labrador Sea, the Greenland Sea, and the Mediterranean

	Heat Flux, W m^{-2}				
	Incoming Solar	*Back Radiation*	*Latent*	*Sensible*	*Total*
Labrador Sea March 1–8, 1995 (ECMWF)	89	−115	−167	−220	−412
Greenland Sea March 3–6, 1989 (ECMWF)	22	−130	−136	−252	−495
Mediterranean Feb. 14–18, 1992 (PERIDOT)	133	−112	−250	−38	−268
Mediterranean Feb. 18–22, 1992 *Poseidon** (all)	128	−98	−188	−46	−204
Mediterranean Feb. 18–22, 1992 *Poseidon** (nights)	0	−98	−196	−48	−342
Mediterranean Feb. 16–20, 1987 (PERIDOT)	180	−123	−297	−108	−348

	Buoyancy Flux, 10^{-8} m^2 s^{-3}		
	Thermal	*Haline*	*Total*
Labrador Sea March 1–8, 1995 (ECMWF)	−8.4	−1.7	−10.1
Greenland Sea March 3–6, 1989 (ECMWF)	−4.3	−1.4	−5.7
Mediterranean Feb. 14–18, 1992 (PERIDOT)	−13.5	−2.8	−16.4
Mediterranean Feb. 18–22, 1992 *Poseidon** (all)	−10.3	−2.1	−12.4
Mediterranean Feb. 18–22, 1992 *Poseidon** (nights)	−17.3	−2.2	−19.5
Mediterranean Feb. 16–20, 1987 (PERIDOT)	−17.6	−3.3	−20.9

* *Poseidon* with coefficients from *Smith* [1988, 1989] for latent and sensible heat loss; and from *Schiano et al.* [1993] and *Bignami et al.* [1995] for longwave radiation.

Little is known about the spatial distribution and the temporal variability of surface heat fluxes at high latitudes. This is primarily because conventional heat flux climatologies (such as those of *Bunker* [1976] and *Cayan* [1992]) are based directly on ship reports, of which there are very few at high latitudes, particularly in the Labrador Sea since the withdrawal of OWS *Bravo*. The horizontal distribution of heat flux during February 1995 from ECMWF analyzed fields is shown in Figure 11a, suggesting that the highest heat loss is located to the northwest of OWS *Bravo*, near the ice edge (marked by the large gradients in Figure 11a).

The standard deviation of the monthly mean total heat flux (not shown) in the Labrador Sea region is of the order of 150 W m^{-2}. The variability of the monthly means is sensitive to the location and intensity of the Icelandic Low. This in turn is associated with the North Atlantic Oscillation [*van Loon and Rogers*, 1978; *Wallace and Gutzler*, 1981] and concomitant changes in the major North Atlantic storm track [see *Rogers*, 1990]. A time series of ECMWF fluxes at the *Bravo* position, shown in Figure 11b, reveals several maxima over the winter and particularly intense cooling in early March 1995. This triggered deep convection observed by moored temper-

TABLE 2b. Typical Winter Meteorological Conditions and Fluxes at the Three Convection Sites

Parameter	*Labrador Sea*	*Greenland Sea*	*Mediterranean*
Air temperature (dry), °C	−9	−14	8
Air temperature (wet), °C	−7	−13	5
Wind speed u_{10}, m s^{-1}	13	13	15
Cloud cover, %	60	60	40
Precipitation, mm d^{-1}	7	3	5
Evaporation, mm d^{-1}	6	4	13
Heat fluxes			
Sensible heat flux, W m^{-2}	−370	−400	−150
Latent heat flux, W m^{-2}	−140	−140	−400
Shortwave radiation, W m^{-2}	80	40	120
Longwave radiation, W m^{-2}	−60	−30	−80
Net heat flux, W m^{-2}	−490	−530	−500
Buoyancy fluxes			
Thermal buoyancy flux, 10^{-8} m^2 s^{-3}	10	5	25
Haline buoyancy flux, 10^{-8} m^2 s^{-3}	2	1	5
Total buoyancy flux, 10^{-8} m^2 s^{-3}	12	5	30

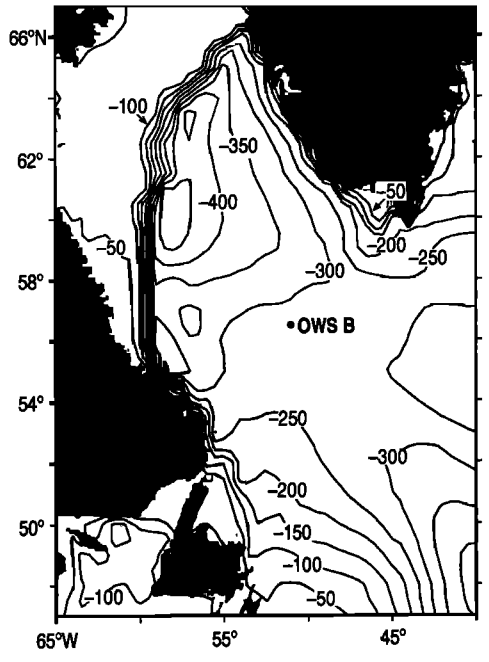

Figure 11a. Spatial distribution of total heat flux in the Labrador Sea from the ECMWF model for February 15 to March 1, 1995.

ature sensors and an ADCP. The heat flux for March 1–7, 1995, averaged ~400 W m^{-2}, with more than half of it by sensible fluxes. The buoyancy flux of 10^{-7} m^{-2} s^{-3} is dominated by the thermal component (see Table 2). From this time series, one can see the episodic and quasi-periodic nature of the fluxes that gives rise to great variability. Compared with the magnitude of the heat flux variations over short periods of time during the winter, the buoyancy contribution of precipitation is rather small.

2.3.2. Greenland Sea. The central Greenland Sea, where convection may occur in late winter, is covered by ice during November–January. ECMWF heat flux and wind stress fields are presented in Figures 12a and 12b during a period of in situ observations of convection in the central Greenland Sea during 1988–1989. The evolution of the stratification in the underlying ocean, together with the periods of ice cover over the station as deduced from the ADCP surface backscatter [*Schott et al.*, 1993], is presented in Figure 12c. It is clear that convection does not occur when the area is covered by ice. Brine rejection by ice into the mixed layer during November–January plays an important role in preconditioning [*Roach et al.*, 1993; *Visbeck et al.*, 1995] and in the convective process itself [see *Rudels*, 1990]. Under the ice the mixed layer deepens slowly as the density increases (Figure 12c). Southward winds are instrumental in exporting the ice and opening the ice-free bay (the Nord Bukta, evident in Figure 8). In February, dramatic mixed-layer deepening due to strong wind bursts and cooling occurs, and deep convection is initiated by the large heat loss maximum in early March [*Schott et al.*, 1993; *Morawitz et al.*, 1996]. The major cooling event of March 3–6, 1989, that triggered deep convection amounted to a total heat loss of about 500 W m^{-2}, of which half was in sensible form (Table 2a). The corresponding buoyancy flux was 5.7×10^{-7} m^{-2} s^{-3}. The haline fraction of the buoyancy flux is large in the low-temperature conditions of the Greenland Sea and amounts to about one quarter of the total.

2.3.3. Northwestern Mediterranean. Meteorological forcing over the Gulf of Lions is primarily a consequence of the cold and dry mistral winds that blow out of the Rhone valley over the preconditioned cyclonic dome (Figure 9) and, to a lesser degree, of the tramontane from the northwest. Because the water temperature is about 12°C and the air temperature only 5°C or so, latent and sensible heat fluxes are enormous. Cooling rates in excess of 1000 W m^{-2} have been estimated during mistral events [*Leaman and Schott*, 1991].

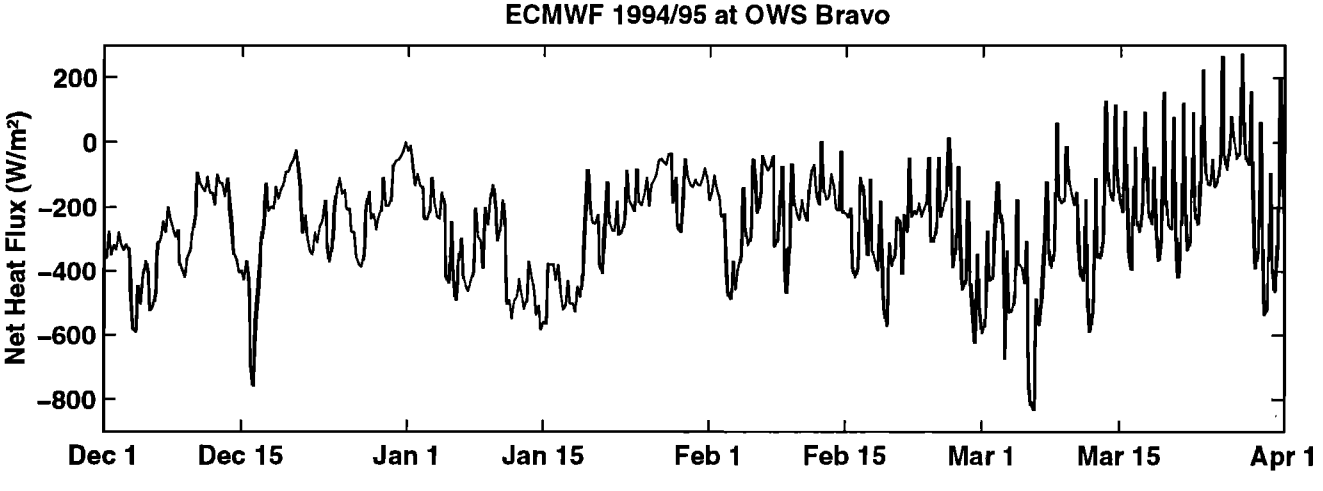

Figure 11b. Time series of ECMWF total heat flux during winter 1994–1995 at position *Bravo* in the Labrador Sea.

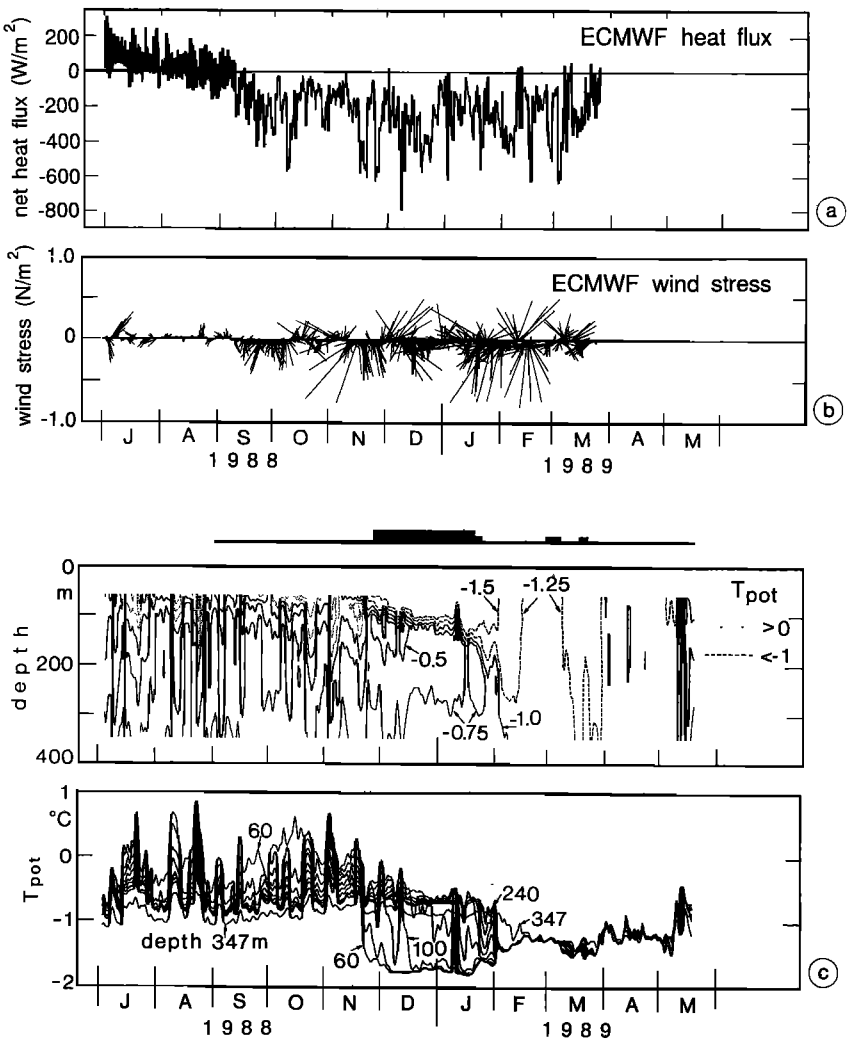

Figure 12. Greenland Sea: (a) Heat flux from the ECMWF model near 75°N, 5°W, during November 1988 to April 1989, (b) the wind vector time series corresponding to Figure 12a, and (c) temperature distribution recorded at moored station near 74.9°N, 5°W, at 60–350 m, showing gradual mixed-layer deepening during the period of ice cover and drastic deepening after the opening of the Nord Bukta. The bar graph on top indicates the presence of ice. After *Schott et al.* [1993].

Figures 13a and 13b show the evolution of heat flux components and winds from the PERIDOT model, during the 1991–1992 convection event [*Schott et al.*, 1996]. The observed winds at coastal stations Pomegues are a good indicator of the mistral and those at Cape Bear (for location, see Figure 9) monitor the tramontane. Typically, the first cooling period occurs during late December. The mixed layer deepens and, at first, it warms before cooling because of higher-salinity, warm water being mixed upward (Figure 13c). Several weaker cooling events followed, completing the preconditioning, so that by mid-February the integrated buoyancy loss was sufficiently large that the second strong cooling event of the season induced deep convection (Figure 13c).

The integrated heat fluxes during 1987, when a very large patch was generated [*Leaman and Schott*, 1991] (Figure 10b) together with fluxes during 1992, are shown in Table 2a. In the period from February 14 to February 18, 1992 (the largest cooling phase during the convection period (Figure 13)) the average heat loss was 286 W m^{-2}. During the 1987 convection period, the mean heat loss suggested by the PERIDOT model was 348 W m^{-2}, corresponding to a buoyancy flux of 2.1×10^{-7} m^2 s^{-3}, 85% of which was due to cooling.

Shortly after the onset of convection, the R/V *Poseidon* was in the region and bulk fluxes were derived from meteorological ship observations. In contrast to other winter convection sites, the northwestern Mediterranean gains heat during the daytime at rates of up to 500 W m^{-2} (even in February). Thus in Table 2a the heat fluxes for the end of that forcing period, February 18–22, are given separately for the night periods, when plumes were more vigorously generated, and for the total time period. The nighttime heat loss was 342 W m^{-2} compared with only 204 W m^2 for the total period February 18–23, 1992.

In summary then, typical buoyancy fluxes during deep convection in the western Mediterranean are $1–2 \times 10^{-7}$ m^2 s^{-3}. Extremely high heat losses have been reported, exceeding 1000 W m^{-2}, but not during periods that coincided with the in situ measurements reviewed here. The flux estimates are clearly incomplete because they do not include precipitation. The direct contribution of precipitation to buoyancy flux, however, is generally considered small on the timescale of a few days. It is

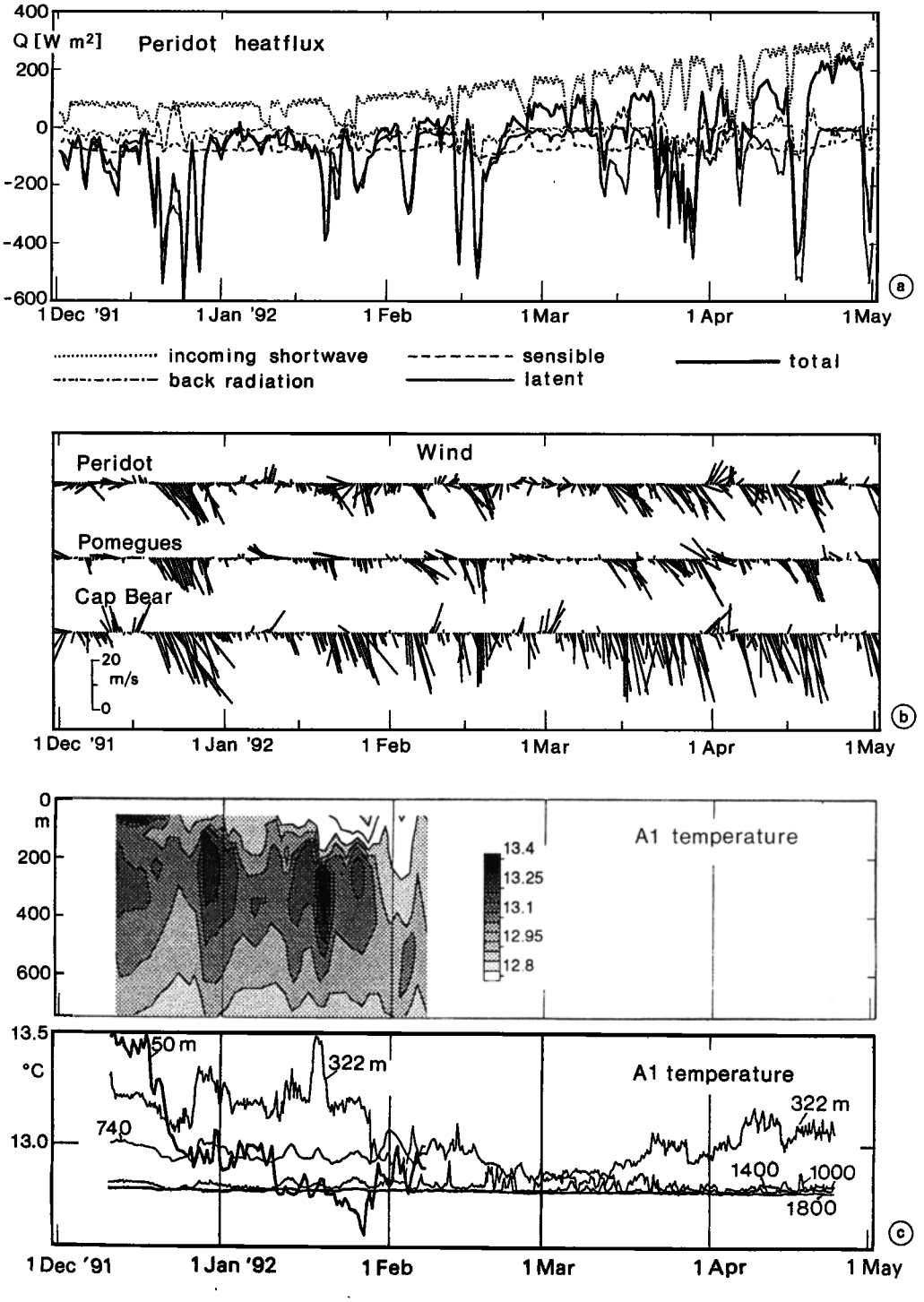

Figure 13. Mediterranean: (a) heat flux (incoming shortwave, sensible, latent, and total) from the PERIDOT model near 42°N, 5°E, during December 1991 to April 1992, (b) the corresponding wind vector time series from PERIDOT and coastal stations Pomegues and Cap Bear (for positions, see Figure 9), and (c) temperature distribution recorded at moored station near 42°N, 5°E, showing mixed-layer deepening, deep convection, and restratification. After *Schott et al.* [1996].

certainly important, however, on the preconditioning timescale (several months), and it is a factor in interannual variability [*Mertens and Schott*, 1998].

Meteorological conditions and fluxes at all three convection sites are drawn together in Table 2b.

3. CONVECTIVE SCALE

We now review what is known about the underlying hydrodynamics of the convective process in which a column of ocean is overturned by convection induced by

widespread buoyancy loss at its surface (the "deep convection" phase in the schematic diagram, Figure 3b). The details of the process are inherently complicated but may not be crucial for understanding the integral effect of convection on the large scale. Thus here we emphasize the benefit of thinking about the ensemble properties of convection rather than the individual elements. We argue that the gross transfer properties of the plumes are dictated by demands placed upon them by the large scale: that they draw buoyancy from depth at a rate sufficient to offset the loss imposed by the meteorology at the surface. This leads to simple and very useful scaling laws and the identification of key nondimensional parameters that have been very successful in bringing order to observations as well as and to laboratory and numerical experiments.

3.1. Gravitational Instability; "Upright" Convection

Consider a resting ocean of constant stratification N_{th} (subscript "th" for thermocline) subject to uniform and widespread buoyancy loss from its upper surface as shown in Figure 14. On the large scale the flow is under geostrophic control and is therefore almost horizontally nondivergent, so the fluid cannot simultaneously overturn on these scales; rather, the qualitative description must be that the response to widespread cooling is one in which relatively small convection cells (plumes) develop. Fluid parcels in contact with the surface (in the "thermal boundary layer" sketched in Figure 14) will become dense and sink under gravity, driving the "free convective layer" below. Buoyancy is drawn upward, across the convective layer, offsetting its loss from the surface.

The thermal boundary layer may be thought of as being analogous to *Howard*'s [1964] conductive layer in laboratory convection between parallel plates, which communicates the boundary conditions from the plates to the interior of the fluid. However, unlike the classical problem, the thermal layer in the open ocean is not the rate-controlling one. *Jones and Marshall* [1993] argue that its depth δ, measured against h, that of the free convective layer, is given by

$$\delta/h \approx 1/Pe^{1/2}$$

where Pe is a Peclet number measuring the efficiency of buoyancy transfer on the plume scale relative to turbulent processes in the thermal boundary layer.

In the ocean the thermal Peclet number is large ($\sim$100); that is, the plumes in the interior are much more efficient at transporting properties vertically than the turbulent elements that make up the thermal boundary layer near the surface. Thus the boundary layer is shallow (perhaps 100 or 200 m deep; see section 3.2.1) relative to the scale of the convective cells occupying the interior of the fluid.

3.1.1. Transfer properties of "free convection." Many competing effects collude together to control the detailed dynamics of the convective layer. However, it is important to realize that irrespective of these details, the gross transfer properties of the population of convective cells must be controlled by the large scale; the raison d'être for the overturning is that it must flux buoyancy vertically to offset loss at the surface. A useful "law" of vertical buoyancy transport can be developed using parcel theory as follows.

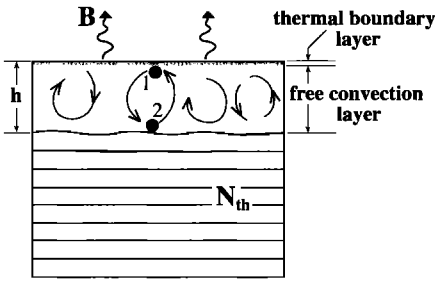

Figure 14. A schematic diagram showing the convective deepening of a mixed layer. An initially resting stratified fluid is subject to widespread and uniform buoyancy loss from the surface; fluid in the "thermal boundary layer" is directly influenced by buoyancy loss at the surface, becomes dense, sinks, and drives the deepening layer of free convection below. The "free convective layer" draws buoyancy from depth at a rate that offsets its loss from the sea surface.

Suppose that the net effect of overturning is to exchange particles of fluid, of buoyancy b_1 and b_2, over a depth Δz; the particles are labeled 1 and 2 in Figure 14. Water made dense by buoyancy loss at the surface sinks, displacing lighter water below and releasing potential energy to power the convective motion and buoyancy flux vertically.

The change in potential energy ΔP consequent on the idealized rearrangement of particles is given by

$$\Delta P = \rho_0 \Delta b \Delta z$$

where $\Delta b = b_1 - b_2$ is the buoyancy difference of the exchanged particles and ρ_0 is a representative value of the density. Equating the released potential energy to the acquired kinetic energy of the ensuing convective motion $K = 2(\frac{3}{2}\rho_0 w^2)$ (there are two particles and isotropy has been assumed with velocity scale w), we then find

$$w^2 \approx \tfrac{1}{3}\Delta b \Delta z \qquad (7)$$

The implied "law" of vertical heat flux on the plume scale is then, using (7),

$$\mathcal{B}_p = w\Delta b = (\Delta z/3)^{1/2}(\Delta b)^{3/2} \qquad (8)$$

where w is the vertical velocity in the plume, Δb is the difference in buoyancy of the rising and sinking fluid, and Δz is the vertical scale over which particles are transported by the convective motion.

Now if, acting in concert, the plumes achieve a vertical buoyancy flux sufficient to balance loss from the

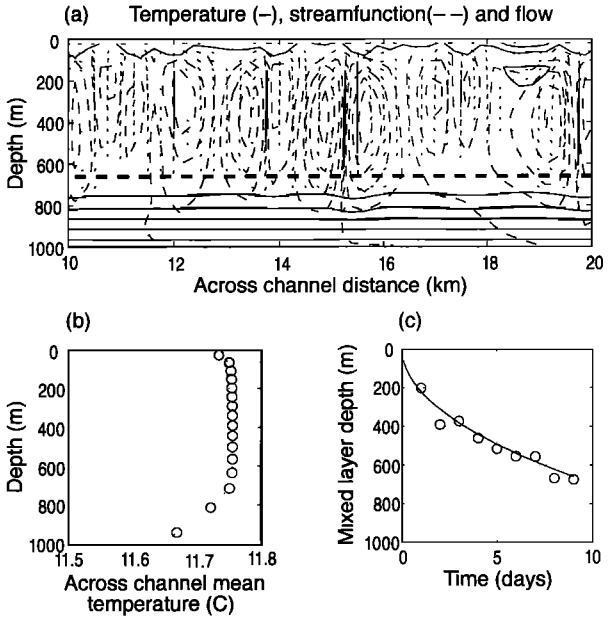

Figure 15. Deepening by upright convection in a numerical simulation: (a) Vertical section showing isotherms (solid), overturning stream function (dashed) and flow indicated by small dashes giving particle displacements during a 30-min period. The peak speeds are (0.069, 0.024) m s^{-1} in the horizontal and vertical directions; the thick dashed line is the prediction of the 1-D law for the depth of the mixed layer (equation (10)). (b) Mean vertical temperature profile corresponding to Figure 15a, showing the stratified layer below, the almost vertically homogeneous layer of vigorous convective activity, and the adverse gradient at the surface. (c) Time series of mixed layer depth. The solid line is the 1-D prediction using (10), and circles are model results.

surface, then $\mathcal{B}_p = \mathcal{B}_0$. Typically, in the Labrador Sea during convection, for example (see Table 2b),

$$\Delta z = 1000 \text{ m} \qquad \mathcal{B}_0 = 10^{-7} \text{ m}^2 \text{ s}^{-3}$$

(equivalent to a heat loss of ~500 W m^{-2} inducing convection over the top kilometer). Equation (8) then implies (solving for Δb) that the temperature difference between upward and downward moving particles (assuming for simplicity that all the buoyancy loss manifests itself in temperature change) is only $\Delta T \approx 10^{-2}$°C and that the intensity of the convective motion is $w \approx 10$ cm s^{-1}, not untypical of the observations (see section 3.4). It is notable that such a tiny temperature difference between rising and sinking fluid parcels can drive vigorous convective motion and achieve such a large heat (and buoyancy) flux. With temperature differences across it of only a few hundredths of a degree, the convective layer is indeed well mixed and stratification within it vanishingly small, yet it can still easily provide the required buoyancy flux.

3.1.2. Rate of deepening. In the limit that the convective layer is vertically homogeneous, and to the extent that entrainment of stratified fluid from the base of the mixed layer can be neglected (see discussion by *Turner* [1973]), then integration of the buoyancy equation

$$Db/Dt = B \tag{9}$$

(where b is the buoyancy and $B = \partial\mathcal{B}/\partial z$ is the buoyancy forcing, the divergence of the buoyancy flux $\mathcal{B}$) tells us that its depth h must increase according to

$$h = \frac{\left[2 \int \mathcal{B}_0 \, dt\right]^{1/2}}{N_{\text{th}}} \tag{10}$$

assuming that N_{th} is constant.

The erosion by convection of a resting, stratified fluid considered above can be readily studied in two dimensions using a nonhydrostatic (incompressible Navier-Stokes) numerical model (see Figure 15). The model used here is described by *Marshall et al.* [1997a, b]. Convection is induced by a steady and spatially uniform buoyancy loss of $\mathcal{B}_0 = 2 \times 10^{-7}$ m^2 s^{-3} from the surface. There are no Coriolis effects. Energetic vertical overturning can be seen in a convecting layer several hundred meters thick, with much weaker flow below. The convection cells are vertical and maintain the layer close to neutral, apart from an inversion (the "thermal boundary layer") close to the surface. The interior of this mixed layer has a temperature contrast of only a few hundredths of a degree over its depth, in accord with that implied by the flux law (8). We estimate a depth for the mixed layer from the mean temperature profile (Figure 15b) and plot its time series in Figure 15c along with the prediction (equation (10)). The agreement is very close.

We will return to this example in section 3.6 when we consider the influence of angular momentum and rotational constraints on convection and the "switch-over" from convection to baroclinic instability.

3.2. The Convection Layer

3.2.1. Mixed patches. Observations of deep, mixed patches are sparse because ship surveys are seldom carried out under the very adverse conditions of winter cooling periods. More frequent are observations of homogeneous water bodies in the spring or summer periods following convection, underneath the newly stratified surface layer.

Several examples of open, deep mixed regimes have been documented from winter observations in the Gulf of Lions, for example, in 1969, 1987, and 1992 (Figure 9) when deep convection occurred in the second half of February of each year. The hydrographic observations within these convection regimes reveal characteristic features that we now discuss in turn.

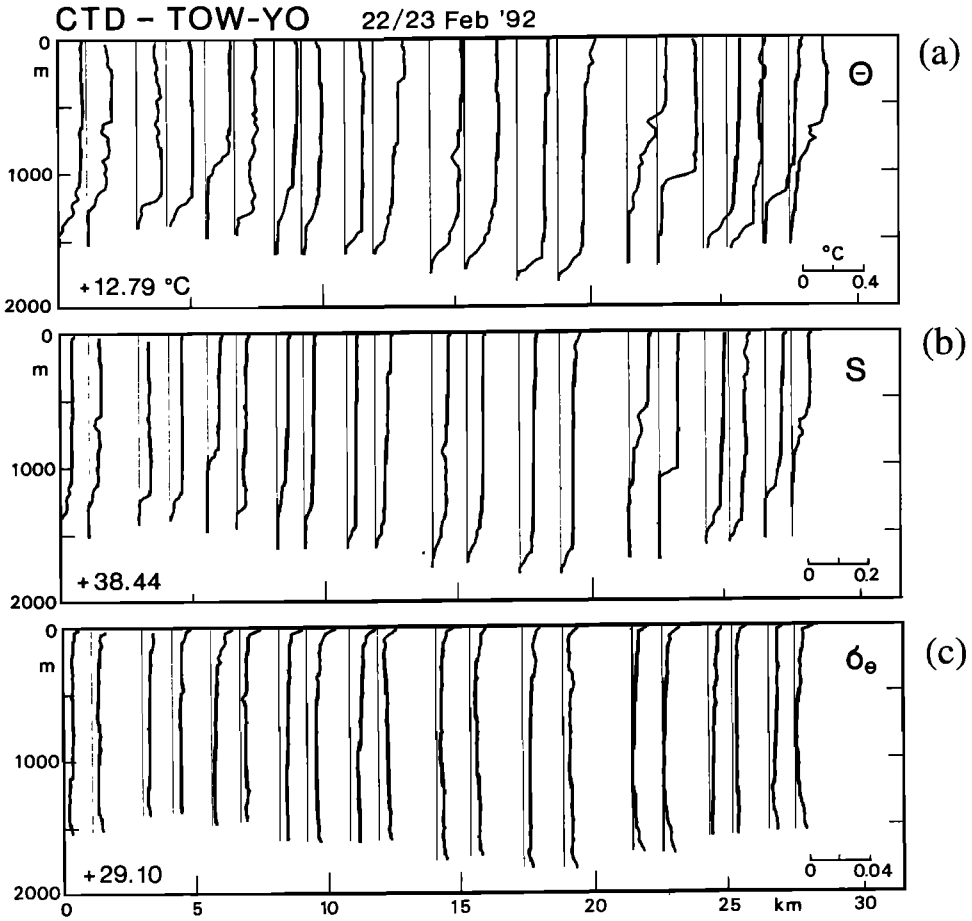

Figure 16. Closely spaced profiles of (a) potential temperature (relative to 12.79°C), (b) salinity (relative to 38.44), (c) potential density (relative to 29.10) from a CTD–Tow Yo section along 5°E through the deep mixed regime of 1992. For position, see Figure 9. From *Schott et al.* [1996].

3.2.1.1. Homogeneity of the "mixed" regime: The degree of horizontal homogeneity of the convection patch can be very variable. While in the 1987 observations of *Leaman and Schott* [1991] the homogeneity was nearly complete, significant vertical and horizontal temperature and salinity inhomogeneities remained in the deep convection patch of 1992 [*Schott et al.*, 1996], as can be seen from closely spaced conductivity-temperature-depth (CTD) profiles in Figure 16. Horizontal standard deviations in the patch were 0.015°C and 0.002 psu, broadly consistent with the scaling arguments introduced in section 3.1.1. The mean profiles were warmer by 0.06°C and saltier by 0.004 psu at 1500 m than in the upper few hundred meters. In density, however, these water mass inhomogeneities were nearly compensated (Figure 16c), both for the individual anomalies and for the profile-mean gradients. It seems that in 1987 a very intense mistral in early January mixed the regime thoroughly and then a second convection event in February mixed it again. By contrast, the 1992 convection event was briefer and weaker, and plumes did not have the time to homogenize the water to the same degree. One might call that latter case incompletely mixed, compared with the completely mixed case of 1987.

In the Labrador Sea, extensive and deep mixed regimes, but capped by newly stratified surface waters, have been observed in summers many months after convection periods (e.g., *Lazier* [1980, 1995] and Figure 7), with horizontal homogeneities to better than 0.02°C and 0.002 psu in the core. However it is not possible to know the degree of homogeneity at the time of, or shortly after, convection. In the Greenland Sea, extensive deep mixed layers have not been reported, perhaps because of the shutdown of Greenland Sea convection over the past decade. In 1989, deep convection was triggered in the preconditioned region of the Nord Bukta and was mapped by towed undulating fish CTD measurements [*Sandven et al.*, 1991] (Figure 8). Individual deep mixed profiles were observed within the stratified environment by conventional shipboard hydrographic profiling [*Rhein*, 1991; *Schott et al.*, 1993]. Similarly, a CTD survey in the preceding winter, 1987–1988, yielded only one homogeneous (to middepth) profile [*Rudels et al.*, 1989]. On the other hand, inverse analysis of integral measurements by acoustic tomography across the central Greenland Sea in winter 1988–1989 revealed a cooling anomaly that reached to deeper than 1000 m [*Morawitz et al.*, 1996]. The coarse horizon-

tal resolution of the acoustic array yielded a lateral scale estimate of 50 km or so. Hence the winter 1988–1989 convection event must have been an incompletely mixed case with significant horizontal inhomogeneities.

3.2.1.2. Deep convection, penetrative or nonpenetrative?: At the bottom of deep mixed patches, steps are often found in the temperature and salinity profiles (Figures 16a and 16b) but they are compensated in density (Figure 16c), at least as suggested by observations available in the Mediterranean. Similarly, steps seem to be absent in deep mixed profiles of the Greenland Sea. Profiles taken during the spring in the Labrador Sea and summer after wintertime convection do not show density steps at the bottom of the deep mixed regime. The evidence then suggests that deep mixing by convective plumes is, to zero order, nonpenetrative. Possible dynamical explanations are discussed in section 3.5.

3.2.1.3. Thermal boundary layer: During active convection, density inversions have been observed at the top of the mixed layer, the thermal boundary layer sketched schematically in Figure 14 and discussed theoretically in section 3.1. *Leaman and Schott* [1991] found that the existence of inversions in the CTD surveys of 1987 was associated with periods of strong surface cooling. Density differences between the surface and the homogeneous part of the profile ranged up to about 10^{-2} kg m^{-3} with some indication that the magnitude of the inversion was inversely related to the layer thickness (as seen in Figure 16c). Unlike in the classical problem where convection occurs between two perfectly smooth plates, we do not believe that the physics of this layer is a central factor in controlling the transfer properties of the convective layer as a whole.

3.2.2. Observed and modeled mixed-layer evolution. Time sequences of mixed-layer development are sparse because observations from ships are infrequent and seldom occur during the winter. Moored instruments can yield time series records throughout a convection season but are not always in an optimum position and often do not have sufficient vertical resolution to accurately chart the development of the mixed layer. However, the development of the depth of the mixed layer in the Gulf of Lions was successfully observed during winter 1991–1992, using CTD casts and moored stations. During this period air-sea flux and stratification measurements were also available (see Figure 13), enabling one to drive a 1-D mixed-layer model and compare the results.

We have argued in section 3.1.1 that free convection is a very efficient transferring agent and does not require large vertical buoyancy gradients to support it. A simple model that assumes that the convective layer is vertically homogeneous, such as that of *Kraus and Turner* [1967] (see also *Niiler and Kraus* [1977] and, briefly, section 5.1.2 for a review), might then be expected to capture many of the gross effects of the convection on the large scale (see, for example, *Lascaratos et al.* [1993]), at least in the initial phase of the process. Here we compare observations of mixed-layer deepening over a convection season with the evolution of the layer as predicted by this simple 1-D model (due to *Rahmstorf* [1991] but conceptually similar to that of *Kraus and Turner* [1967]). Should the column become statically unstable as a result of buoyancy loss at the surface, convective adjustment is performed until the layer is vertically mixed with no density gradient at the base. In addition, mixed-layer deepening due to wind stirring is also taken in to account through a turbulent kinetic energy equation. The model was initialized with CTD casts obtained in mid-December 1991 and stepped forward using fluxes from the French PERIDOT weather-forecasting model. Broadly similar fluxes were obtained when calibrating coastal meteorological station data against ship measurements [*Mertens*, 1994].

The density changes are calculated from temperature and salinity using a linearized equation of state of the form of (3). A series of temperature and salinity profiles from near 42°N, 5°E in the center of the deep mixed patch is shown in Figure 17a, along with model predictions. The development of mixed-layer salinity in the model for the upper 150 m and for the Levantine Intermediate Water layer of 150–500 m also compares favorably with the CTD observations (Figure 17a). When the mixed layer reaches into the salinity maximum of the LIW layer (see Figure 2c), the surface salinity (and temperature) increases.

Model runs have been compared with observations of the depth of the mixed layer assuming static erosion of the stratification due to surface buoyancy loss alone (i.e., when all entrainment terms are set to zero). Departures occur when the mixed layer is shallow, and wind mixing is important, but the ultimate depth reached by convection depends solely on the surface buoyancy flux and is independent of entrainment. As was discussed above, observations show that deep convection below the wind-affected layers is typically nonpenetrative.

Visbeck et al. [1995] used the same model to study mixed-layer development during the Greenland Sea Experiment of 1988–1989, when intermediate-depth convection was observed [*Schott et al.*, 1993]. The model was driven by ECMWF fluxes (Figure 12) and initialized with the November 1988 stratification from observations. Only a fraction of the surface cooling is now felt, through ice-free areas and conduction through the ice, by the underlying ocean. Moreover, an additional buoyancy flux must be included that represents the effect of brine rejection on ice formation and subsequent ice export. Comparison with the observations were most favorable (Figure 18) when an ice export of 8 mm d^{-1} over the winter period was taken into account and the cooling rate below the ice was reduced by 40%. The observed interannual variability in the depth of convection, in particular that no convection below 400 m occurred in 1990–1991, could then be reproduced by the simple model. Such modeling work suggests that ice, and then ice export, is a key player in the convective process

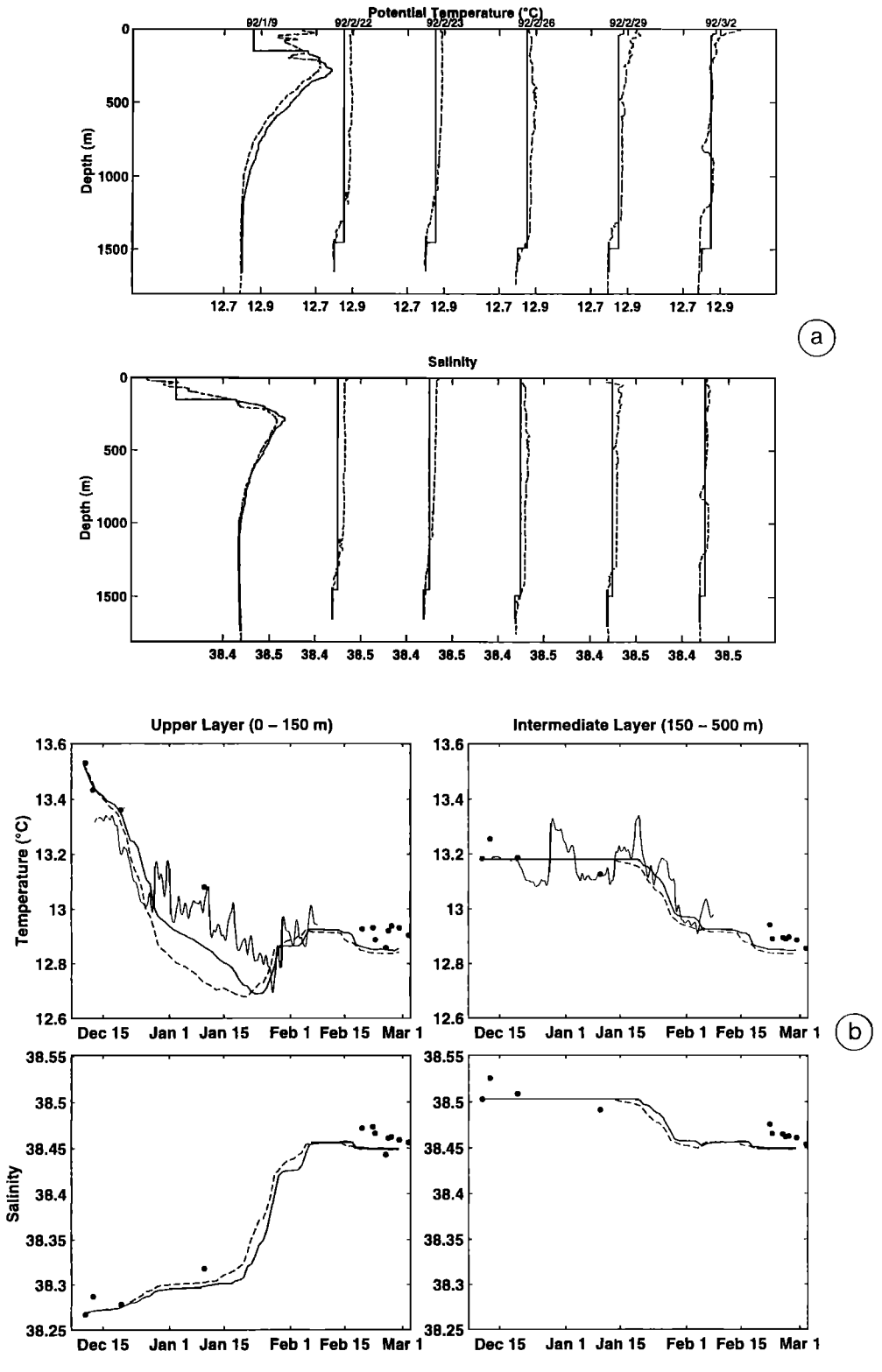

Figure 17. Mixed-layer depth development in the northwestern Mediterranean convection regime during winter 1991–1992: (a) individual CTD casts near 42°N, 5°E (dashed) and from mixed-layer model, driven by PERIDOT model fluxes; (b) averaged (top) temperature and (bottom) salinity for the (left) upper (0–150 m) and (right) Levantine Intermediate Water (150–500 m) layers in the Gulf of Lions during winter 1991–1992 from model run (PERIDOT fluxes, solid) and from moored thermistor string records (dashed) and CTD casts (dots). (After *Mertens* [1994]).

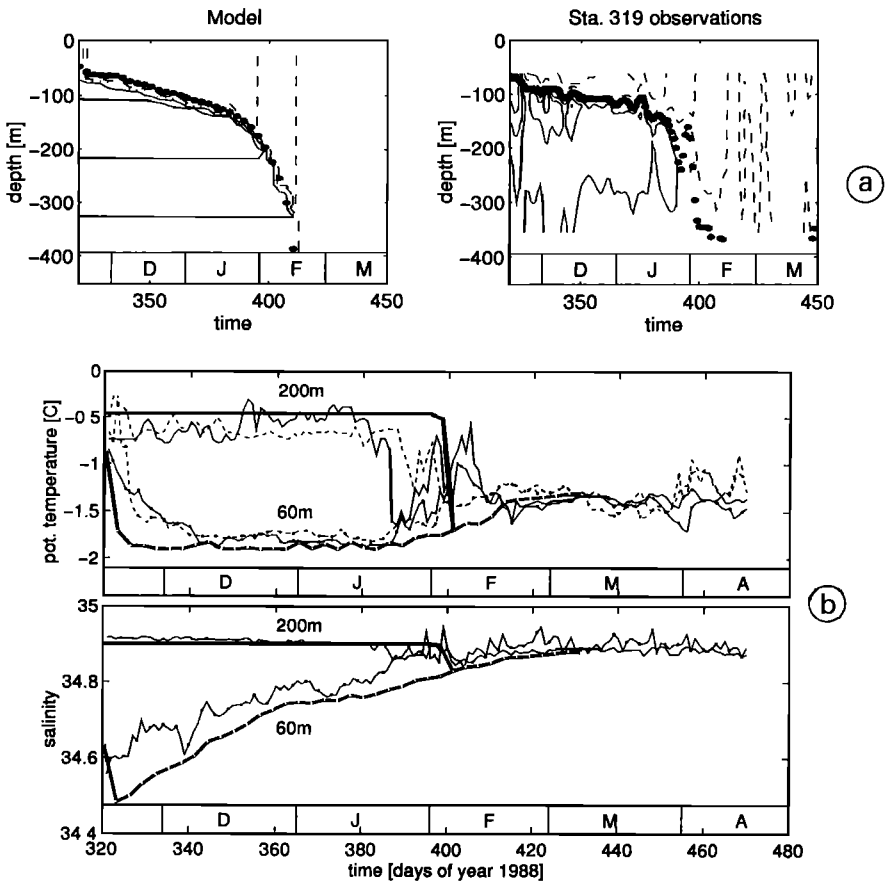

Figure 18. (a) Mixed-layer deepening in the Greenland Sea during the winter of 1988–1989 (from *Visbeck et al.* [1995]): for a station at the southern margin (position 319, Figure 8), (left) as predicted by the model driven by ECMWF model fluxes that are reduced by 40% during times of ice cover and include a brine rejection term that is due to an ice export of 8 mm d^{-1} and (right) as observed by moored thermistor string temperatures. (b) Observed (top) temperatures and (bottom) salinities at depths of 60 m and 200 m at the southern (light dashed) and central (light solid) compared to those obtained from the mixed-layer model for 60-m (heavy dashed) and 200-m depth (heavy solid).

in the central Greenland Sea by facilitating the necessary reduction of mixed-layer stability.

In summary, simple mixed-layer models can be successfully used to represent the evolving mixed layer and interior mixed patch properties on short timescales. However, lateral advection plays an increasingly important role as time progresses and can dominate over seasonal and interannual timescales.

3.3. Plume Dynamics

Once a mixed layer is established, subsequent convection occurs into fluid in which $N^2 \approx 0$. Accordingly, we now consider convection into a neutral fluid of depth h, and review physically motivated scaling ideas that have been very influential in the development of our understanding of ocean convection and have provided organizing principles. We draw out two particular aspects that are of considerable theoretical interest. First, the Earth's rotation may have an influence on the convective process itself in the ocean. If convection reaches very deep and the associated timescales are sufficiently long, then the "stiffening" of the fluid by the Earth's rotation could be felt by the convective elements, the plumes, themselves. Second, the convective process is spatially localized in the ocean, and lateral as well as vertical exchange of buoyancy and fluid is important: convection can give way to baroclinic instability. This latter theme, that of the role of baroclinic instability, will be introduced toward the end of this chapter but will be the central focus of attention in section 4.

3.3.1. Scaling ideas. Imagine that loss of buoyancy associated with a sustained surface flux of magnitude $\mathcal{B}_0$ drives convection in to a homogeneous fluid of depth h as illustrated schematically in Figure 19. A layer of 3-D, buoyancy-driven turbulence will deepen as the plumes that make it up evolve in time, penetrating into the fluid below. Ultimately, the convection will extend down to the depth h. Let us suppose that in the initial stages, plumes extending into the convective layer are so small in scale that they cannot feel the finite depth h. Furthermore, for times $t \ll f^{-1}$, rotation is unimportant; only $\mathcal{B}_0$ remains as the controlling parameter. It is

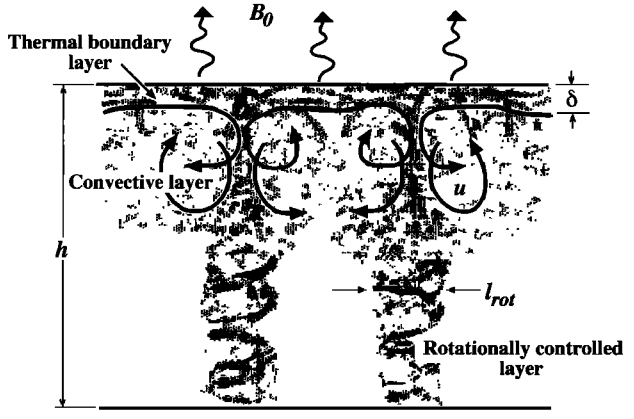

Figure 19. A schematic representation of the evolution of a population of plumes under rotational control sinking in to a homogeneous fluid of depth h, at a latitude where the Coriolis parameter is f, triggered by buoyancy loss $\mathcal{B}_0$. If the fluid is sufficiently deep (as drawn here) the plumes that make up the convective layer will come under rotational control on the scale l_{rot}.

then not possible to construct scales for the depth, buoyancy, or velocity of the plumes. The convective process must evolve in time, and we suppose that it proceeds in a self-similar way. The following scales can be formed from $\mathcal{B}_0$ and t (a more detailed account is given by *Jones and Marshall* [1993] and *Maxworthy and Narimousa* [1994]):

$$l \sim (\mathcal{B}_0 t^3)^{1/2} \tag{11a}$$

$$u \sim w \sim (\mathcal{B}_0 t)^{1/2} \tag{11b}$$

$$b \sim (\mathcal{B}_0/t)^{1/2} \tag{11c}$$

where l is a measure of the scale of the convective elements.

3.3.1.1. Scale constrained by the depth: If it is the depth h that ultimately limits the scale of the cells then putting $l = h$ in (11a), the following scaling is suggested [*Deardorff*, 1985], independent of rotation:

$$l \sim l_{\text{norot}} = h \tag{12a}$$

$$u \sim u_{\text{norot}} = (\mathcal{B}_0 h)^{1/3} \tag{12b}$$

$$b \sim b_{\text{norot}} = (\mathcal{B}_0^2/h)^{1/3} \tag{12c}$$

The subscript "norot" indicates that these are the scales adopted in the absence of rotation; these are the scales implicit in the flux law equation (8).

3.3.1.2. Scale constrained by the Earth's rotation: If h is sufficiently large then the evolving convection will come under geostrophic control before it arrives at the depth h. The transition from 3-D buoyancy-driven plumes to quasi-2-D, rotationally dominated motions (represented schematically in Figure 19) will occur as t approaches f^{-1} at which point, replacing t by f^{-1} in equation (11), the following scales pertain [see *Fernando et al.*, 1991]:

$$l \sim l_{\text{rot}} = (\mathcal{B}_0/f^3)^{1/2} \tag{13a}$$

$$u \sim u_{\text{rot}} = (\mathcal{B}_0/f)^{1/2} \tag{13b}$$

$$b \sim b_{\text{rot}} = (\mathcal{B}_0 f)^{1/2} \tag{13c}$$

where the subscript "rot" (for "rotation") has been used to denote the scales at which rotation begins to be important. *Golytsin* [1980] appears to have been the first to write down the scales (13). Relations (12) and (13) are enumerated in Table 3 for a range of buoyancy fluxes typical of deep convection.

At these scales the plume Rossby number is unity:

$$Ro = \frac{u}{fl} \sim \frac{u_{\text{rot}}}{fl_{\text{rot}}} = 1$$

It should be noted that the foregoing scales are independent of assumptions concerning eddy viscosity and diffusivity, provided that they are sufficiently small; they are the velocity, space, and buoyancy scales that can be constructed from the "external" parameters $\mathcal{B}_0$, f, and h. However, the constants of proportionality in (12) and (13) will be dependent on viscous/diffusive processes and can be determined experimentally from laboratory and numerical experiments (see section 3.5.1 and equation (18)).

Helfrich [1994] has vividly illustrated possible rotational constraints on convective plumes in the laboratory. Figure 20 shows a sequence of photographs from an experiment in which a salt solution, dyed for flow

TABLE 3. Velocity, Buoyancy, and Space Scaling in the Open-Ocean Deep Convection Regime

	Scaling	*Heat Flux = 100 W m^{-2}; Buoyancy Flux = 5.00 × 10^{-8} m^2 s^{-3}*	*Heat Flux = 500 W m^{-2}; Buoyancy Flux = 2.25 × 10^{-7} m^2 s^{-3}*	*Heat Flux = 1000 W m^{-2}; Buoyancy Flux = 5.00 × 10^{-7} m^2 s^{-3}*	*Heat Flux = 1500 W m^{-2}; Buoyancy Flux = 7.25 × 10^{-7} m^2 s^{-3}*
l_{rot}, km	$(\mathcal{B}_0/f^3)^{1/2}$	0.22	0.47	0.71	0.85
u_{rot}, m s^{-1}	$(\mathcal{B}_0/f)^{1/2}$	0.02	0.05	0.07	0.09
u_{norot}, m s^{-1}	$(\mathcal{B}_0 h)^{1/3}$	0.04	0.08	0.09	0.12
Ro^*	$\mathcal{B}_0^{1/2}/f^{3/2}h$	0.11	0.24	0.35	0.43
l_ρ, km	$h\sqrt{Ro^*}$	0.67	0.97	1.19	1.31

Here h = 2 km and $f = 10^{-4}$ s^{-1}.

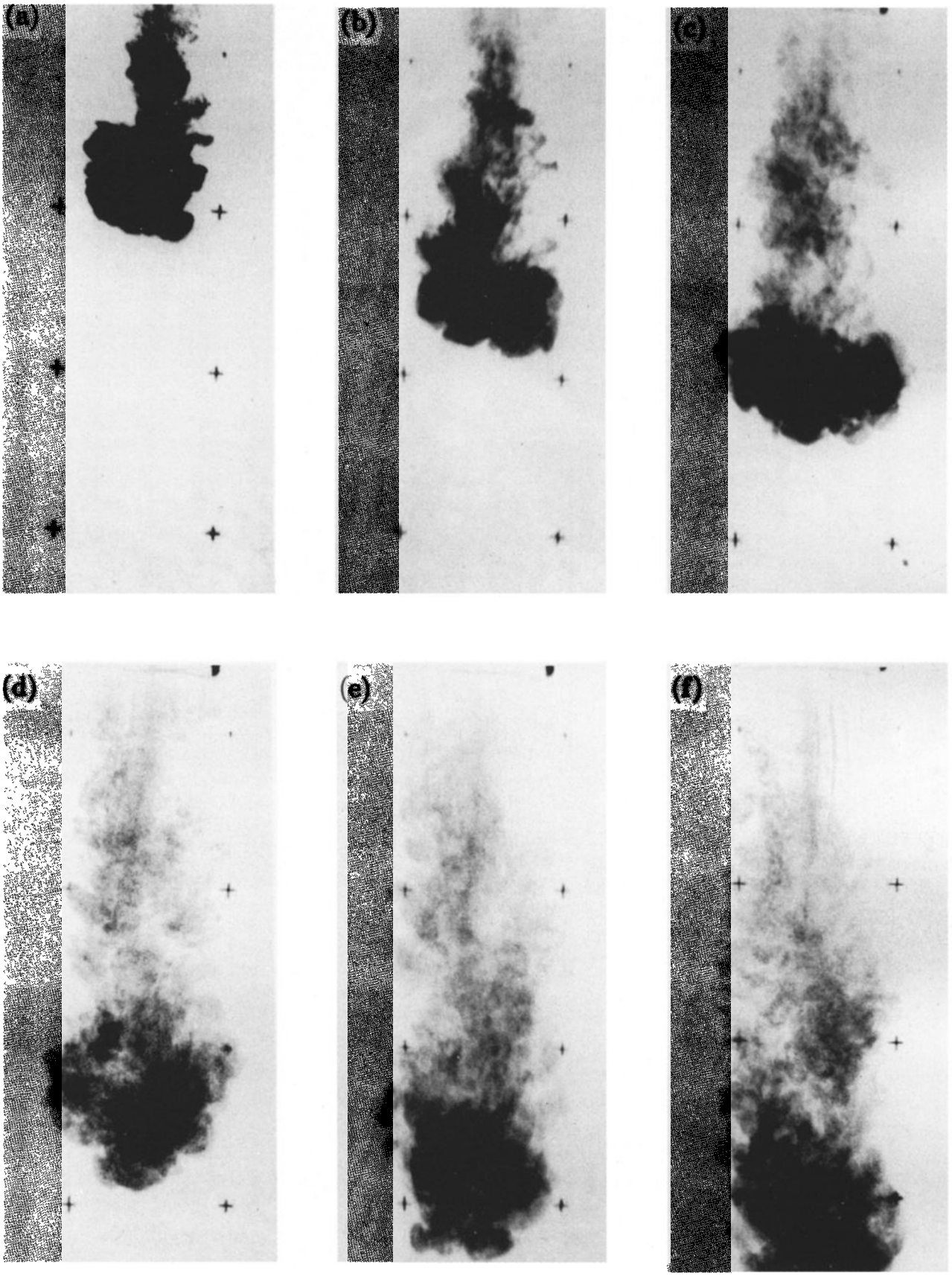

Figure 20. A sequence of photographs from a laboratory experiment carried out by *Helfrich* [1994]. The effects of rotation are evident in Figures 20d through 20f. The radius remains nearly constant, and the front falls to form a columnar structure, which ultimately undergoes geostrophic adjustment to form an anticyclonic conical eddy of dense fluid on the tank bottom.

visualization, was introduced into a rotating volume of fresh water. As the plume sinks it will fold in (entrain) fluid from the surroundings, leading to expansion in the lateral scale of the plume as it reaches farther down. However, if the neutral layer is sufficiently deep, the entraining plume will attain a lateral scale at which it becomes "aware" of rotation before it strikes the bottom. This inhibition of lateral growth in the presence of rotation is a consequence of the existence of "Taylor" columns that impart rigidity to the fluid column and that resist lateral displacement. In view of the foregoing discussion, one might expect this lateral scale to be a function of l_{rot}. In the experiment shown in Figure 20, the buoyancy flux and rotation rate were such that l_{rot} was much less than the water depth. Figures 20a to 20c show the early evolution before rotation becomes important. The effects of rotation are evident in Figures 20d through 20f. The radius remains nearly constant, and the front forms a columnar structure, which ultimately undergoes geostrophic adjustment to form an anticyclonic, conical eddy of convected fluid on the tank bottom. The radius of the column is found to scale very closely with an appropriately defined l_{rot}.

A consideration of angular momentum constraints readily suggests that if rotation is indeed felt on the convective scale, radial inflow at upper levels will spin up cyclonic vorticity and radial outflow below anticyclonic vorticity (see *Chandrasekhar* [1953, 1961]; *Veronis* [1959], who addressed the problem from the perspective of linear theory; and also *Davey and Whitehead* [1981]). Thus, superimposed on the overturning circulation, there will be lateral circulation, cyclonic above, anticyclonic below. The degree of lateral circulation depends on the degree to which the fluid is stiffened by rotation (i.e., the smallness of the natural Rossby number introduced now in section 3.3.2). The horizontal swirling motions may be important agents of horizontal mixing (see *Julien et al.* [1996b] and section 3.5.2).

3.3.2. Nondimensional numbers. We now consider the important nondimensional parameters that govern ocean convection.

3.3.2.1. Natural Rossby number: The considerations discussed above suggest that if l_{rot}/h is small, one might expect to see an upper convective layer beneath which plumes, under rotational control, extend down to the bottom, as shown schematically in Figure 19.

The natural Rossby number [*Maxworthy and Narimousa*, 1994; *Jones and Marshall*, 1993]

$$Ro^* = \frac{l_{rot}}{h} = \left(\frac{\mathcal{B}_0}{f^3 h^2}\right)^{1/2} \qquad (14)$$

is a measure of this ratio, comparing the scale l_{rot}, at which convection comes under the influence of the Earth's rotation, with the total depth of the convective layer h. Some authors [e.g., *Raasch and Etling*, 1991; *Julien et al.*, 1996b] use the term "convective" Rossby number, which differs from (14) only in the value of the exponent (1/3 rather than 1/2). *Julien et al.* [1996b] include a short history of convective Rossby numbers. *Marshall et al.* [1994] discuss the physical content of (14) at length.

How large is Ro^* in the ocean, and how do typical oceanic and atmospheric values compare? Typical vertical heat fluxes achieved by a population of convective elements are comparable in atmospheric and oceanic convection; indeed, they have to be because heat loss to the atmosphere drives convection in the ocean. The buoyancy fluxes are very different, however, with the vertical buoyancy flux in the atmosphere exceeding that in the ocean by many orders of magnitude. If the two fluids achieve the same heat flux, the ratio of the buoyancy flux is

$$\frac{\mathcal{B}_{atmos}}{\mathcal{B}_{ocean}} = \frac{\rho_w c_w}{\rho_a \alpha c_a \vartheta_a} \approx 10^5$$

where ρ is the density, c is the specific heat, and α is the coefficient of thermal expansion of water, with ϑ_a^{-1} the analogous quantity for air (where ϑ_a is a typical air temperature). Subscripts w and a represent water and air, respectively.

Inserting typical meteorological values (see Table 2b), we find that atmospheric buoyancy fluxes are some 10^5 times greater than oceanic buoyancy fluxes, giving an l_{rot} of 100 km or more in the atmosphere, compared with only 100 m or so in the ocean. Typical vertical scales of convection in the atmosphere are set by the depth of the troposphere, $h = 10$ km, giving $Ro^* \approx 10$; the convection "hits the ceiling" before it feels the effect of rotation.

Contrast this with the ocean. At the site of deep convection in the western Mediterranean Sea, for example, where $h \approx 2000$ m, $f \approx 10^{-4}$ s^{-1}, and heat fluxes in excess of 800 W m^{-2} have been observed, $\mathcal{B}_0 \approx 4 \times 10^{-7}$ m^2 s^{-3} [*Leaman and Schott*, 1991] then $Ro^* = 0.3$. Deep convection encompasses regimes from the Labrador Sea to the Weddell Sea, and so relevant ranges for h are 1000 m to 4000 m, $\mathcal{B}_0$ from 10^{-7} m^2 s^{-3} to perhaps 5×10^{-7} m^2 s^{-3} (see Tables 2 and 3) and f from its Mediterranean value up to 1.5×10^{-4} s^{-1} in polar oceans. Consequently values of Ro^* from ~0.01 to 1 are most relevant to oceanic deep convection suggesting that rotation cannot be ignored even on the plume scale (see Table 3). In summary, then, Ro^* is large in the atmosphere but small in the ocean.

Finally, in view of the importance of Ro^* in the development of ideas about the plume-scale and mixed-patch dynamics, it is useful to have a number of interpretations of it. Using the rotational scaling outlined above, Ro^* is a measure of the fraction of the total depth that a particle reaches in a rotation period. Alternatively, one can think of Ro^* as a measure of the number of vertical excursions a particle makes in a rotation period; strong forcing makes the particle undergo many circuits in a day and rotation is felt little. The square of Ro^* is a nondimensional measure of the

strength of the forcing, comparing $\mathcal{B}_0$ with f^3h^2; a velocity scale fh times a measure of acceleration, f^2h. Finally, as we shall see in section 4, its square root is a measure of the radius of deformation relative to the depth of the ocean, pertaining after the convective overturning of an initially unstratified ocean has ceased.

3.3.2.2. Rayleigh, Taylor, and Nusselt numbers: In addition to Ro^* there are a variety of other nondimensional parameters that help us to interpret laboratory and numerical studies in terms of the observations. The influence of diffusion of momentum and buoyancy may be characterized by the flux Rayleigh number (which is independent of f),

$$Ra_f = \frac{\mathcal{B}h^4}{\kappa^2\nu} \tag{15}$$

where ν and κ are the ("eddy") viscosity and thermal diffusivity respectively, or by the Taylor number,

$$Ta = \frac{1}{Ek^2} = \left(\frac{fh^2}{\nu}\right)^2 \tag{16}$$

and Ek is the vertical Ekman number. *Boubnov and Golitsyn* [1990] employed a regime diagram that divides the $(Ra_f - Ta)$ plane into the following regions, for increasing flux Rayleigh number and Taylor number: (1) the conduction regime, in which diffusion suppresses convective instability, (2) a regime of regular structure, in which convection takes the form of uniform cells, (3) a geostrophic turbulence regime, and (4) a fully turbulent regime.

Appropriate values of Ra_f and Ta for oceanic deep convection are not known with any certainty because the turbulent processes must be represented by eddy viscosities and diffusivities, which are not distinct from the convective process itself. For this reason, *Klinger and Marshall* [1995] attempt to characterize the flow in terms of (Ra_f, Ro^*), rather than the more common choice (Ra_f, Ta). The former pairing leads to a tidy division of the external parameters between a viscous/diffusive parameter independent of rotation (Ra_f) and a rotational parameter independent of diffusion (Ro^*). This is especially useful for application to the ocean because although Ro^* is rather readily calculated for convection in the ocean, Ra_f depends on poorly known values of eddy diffusivity.

A Nusselt number can be defined that compares the convective to the diffusive buoyancy transport:

$$Nu = \frac{\mathcal{B}_p}{\kappa\Delta b/h}$$

Here Δb is the buoyancy difference between two flat plates and κ is a diffusivity (for buoyancy). This problem differs considerably from our (and indeed most other) geophysical problems because in nature a buoyancy flux is demanded from the fluid, rather than a Δb imposed, and there is no lower boundary. Nevertheless, suppose that using (15), we substitute for $\mathcal{B}_p$ in to the above expression for the Nusselt number. Then, identifying $Ra = \Delta bh^3/\kappa^2$ as a Rayleigh number, the flux law derived in section 3.1 (equation (8)) implies

$$Nu \sim Ra^{1/2}$$

The $Ra^{1/2}$ dependence is the only one that gives a flux law (that in (8)) that is independent of the diffusivity. This should be contrasted with the 1/3 or 2/7 debate of the "hard turbulence" community, who are attempting to understand laboratory plume convection (see the discussion of *Werne* [1995]). In hard turbulence the nature of the thermal boundary layer (i.e., how the heat gets from the plate in to the body of the fluid) is the rate-controlling process and is crucial in setting the character of the free convective layer between the plate. One is then led to scaling laws that are sensitive to boundary conditions (no-slip 2/7 or slip 1/3) and depend on the molecular diffusivity κ. This makes the relevance of these laws to geophysical fluids problematical (for a further discussion of these issues, see *Emanuel* [1994]).

Given that ocean convection is not in a regime controlled by molecular processes, with momentum and heat being carried by turbulent processes that are not distinct from the convection itself, it is appropriate to set $\nu = \kappa$ and assume that the Prandtl number is unity:

$$Pr = \nu/\kappa \tag{17}$$

where ν and κ are an eddy viscosity and diffusivity, respectively.

3.4. Observations of Plumes in the Ocean

3.4.1. Space and velocity scales of plumes. Given the technical limitations of observing 3-D, small-scale phenomena in the ocean, it is not possible to rigorously test the scaling arguments presented in the last section with field observations; that is more sensibly done by controlled laboratory and numerical experiments as described in section 3.5. However, one can look for broad consistency between observations and the scales set out in Table 3.

In MEDOC 1970, the first field experiment with direct measurements, downward velocities of 12 cm s^{-1} were observed by a rotating float [*Voorhis and Webb*, 1970]. The floats resided at constant depth and were equipped with fins that made them rotate in a field of vertical motion. The character and scale of the convective elements could not be determined. In the Labrador Sea, however, *Gascard and Clarke* [1983] found from two closely separated floats that one showed a downward motion of 9 cm s^{-1} and the other underwent oscillatory motion, suggesting a decorrelation scale of the order of 1 km.

With the advent of self-recording acoustic Doppler current profilers, detailed observations in convection regimes were made possible. Time series of ADCP vertical velocity records from the different convection sites

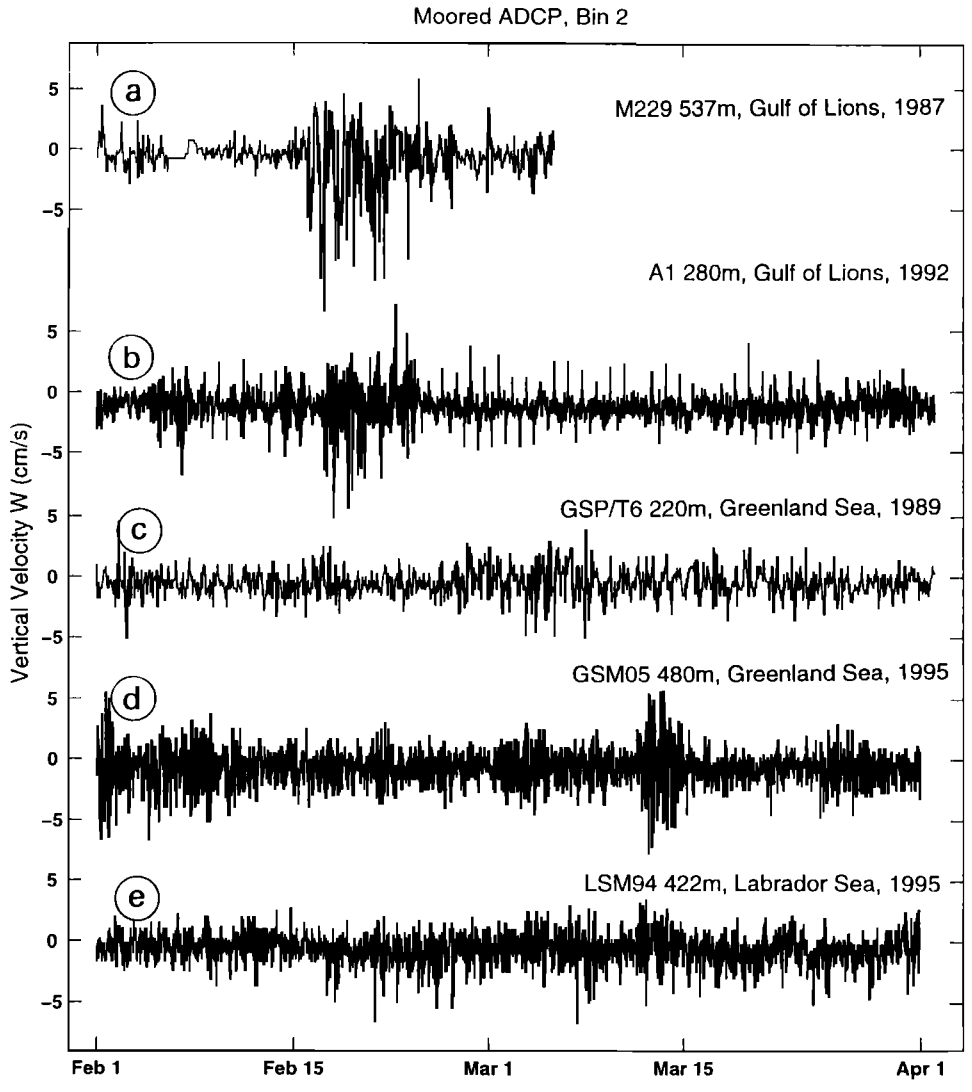

Figure 21. ADCP time series of vertical velocities measured during deep convection events: (a) Gulf of Lions, 1987; (b) Gulf of Lions, 1992; (c) Greenland Sea, 1989; (d) Greenland Sea, 1995; and (e) Labrador Sea, 1995. All show short-period, strong downward motions resulting from the plumes with weaker upward motion in between.

are shown in Figure 21 for the periods of late winter cooling. The first experiment using moored ADCPs was carried out in the Gulf of Lions in early 1987, after deep convection had occurred [*Leaman and Schott*, 1991; *Schott and Leaman*, 1991]. A mistral with heat fluxes reaching 500 W m^{-2} caused vertical motions of up to 13 cm s^{-1} with duration of only 1–2 hours at the moored sites (Figure 21a). Vertically coherent downward flow over the 300-m observational range of the ADCPs was observed. From the advection speeds recorded and the passage time of the plume past the Eulerian measurement, its horizontal scale was estimated to be of O(1 km). Determination of the sense of horizontal rotation of an advected feature from Eulerian measurements is rather difficult because one has to determine how the moored station cuts the plume. Plumes were found to be associated with horizontal circulation but without a preferred sense of rotation [*Schott and Leaman*, 1991].

A plume experiment with moored ADCPs both near the surface (200- to 550-m depth) and at middepth (1100–1400 m) was carried out by *Schott et al.* [1993] in the central Greenland Sea (the position of GSM is marked in Figure 8). Convection there was found to be weaker than in the Mediterranean experiment of 1987 with much more sporadic occurrence of plumes (Figure 21c). One event was found (Figure 22) where vertically sheared advection from the east carried a plume past the site; the plume was slanted westward because of the stronger currents at upper levels. When the upper part of the plume arrived, currents at the 400-m level were deflected to the south, suggesting cyclonic rotation, while currents at ~1200 m were deflected to the north, suggesting anticyclonic rotation and in agreement with angular momentum considerations (see section 3.3.1). Much more intense vertical velocities were observed at that site in winter 1994–1995 (Figure 21d).

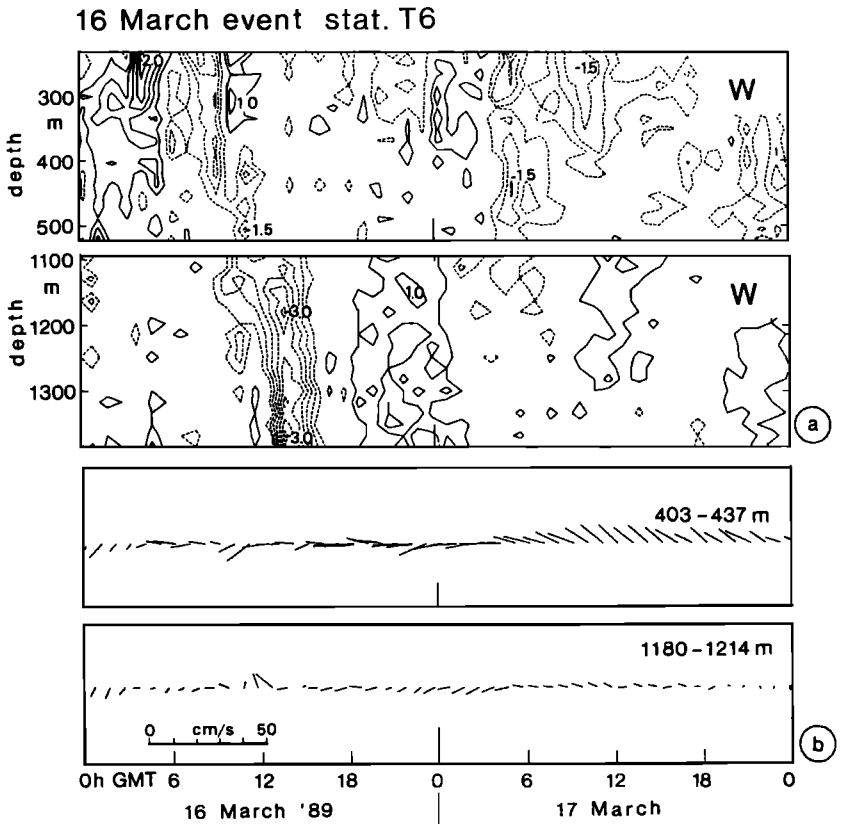

Figure 22. (a) Time-depth plots of vertical velocities during a plume passage in the central Greenland Sea. (b) Horizontal ADCP currents at depths of 403–437 m and 1180–1214 m.

In an experiment with a triangular, 2-km-side array in the Gulf of Lions during winter 1991–1992 (see Figure 9), three ADCPs simultaneously covered the range 200–500 m at the stations, and a fourth one extended the range at one station down to 600 m. A time series of the vertical velocities from the preconditioning period (mid-December 1991 into spring 1992) is shown in Figure 21b for one of the ADCPs at a depth of 280 m. In the early part of winter the ADCP was still located in the stratified intermediate layer, and the mistral of late December caused a burst of internal wave energy. Deep convection occurred during February 18–23 (Figure 21b) within the confines of the region marked in Figure 9, but the mixed patch was much less homogeneous than during 1987.

Another way to estimate horizontal plume scales is to use the beam spreading of the four beam ADCPs (see Figure 23). With a 20° beam angle, the beams are separated horizontally by 200 m at a vertical distance of 300 m from the transducer. Hence the increase of decorrelation with increasing transducer distance allows estimates of the horizontal scale. Comparing the results of artificial plume models with the measured decorrelation scales, M. Visbeck (private communication, 1994) concluded that the plumes indeed had horizontal scales of 500–800 m.

The strong diurnal cycle of the heat flux, changing from 200 W m^{-2} during the day to 400 W m^{-2} cooling at night (Figure 24a), allowed an estimate of the lifetime of plumes that were generated at night. With an rms plume velocity of 2 cm s^{-1}, plumes should begin to be detected at the 300-m level ~4 hours after the cooling begins to be effective (i.e., after the buoyancy gain caused by daytime warming has first been erased, here typically 3 hours). Vertical velocity variance picked up drastically at about 2200 (Figure 24c), in reasonable agreement. After cooling stopped, the vertical velocity variance decayed from a level of 6–9 cm^2 s^{-2} during the night and morning hours to only 1–3 cm^2 s^{-2} in the afternoon and early evening (Figure 24c); this yields a plume decay timescale of a mere 6 hours.

Vertical velocities measured by ADCPs might not be due solely to plumes, because active migration of zooplankton scatterers can amount, on occasions, to several centimeters per second. However, the comparison of the described variances during the mistral with those from the quiet period before (February 5–15) shows that this effect was minor compared with the plume activity (Figure 24c).

In the Labrador Sea, where convective activity had been large in the early 1990s, an ADCP was deployed over the winter 1994–1995, covering the depth range 150–440 m. In early March, vertical velocity events with temporal and vertical velocity scales typical of other sites were observed (Figure 21e). Maximum speeds were 7 cm s^{-1}, and the vertical velocity variance during the forcing phase was 1.5 cm^2 s^{-2}. Despite widespread convection in the Labrador Sea during the observing periods, these vertical motions appear to be somewhat less intense than

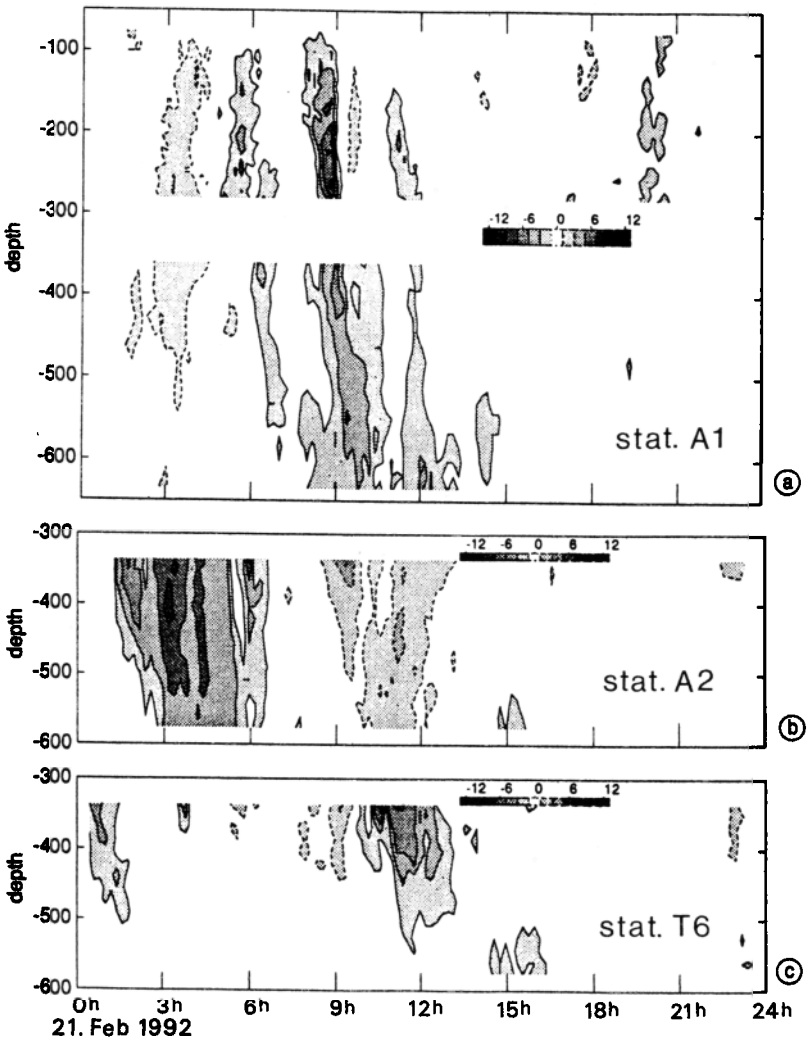

Figure 23. Time-depth plots of vertical velocities from the four ADCPs in the triangular moored array, February 22, 1992, showing duration and depths of plumes (for location see Figure 9): (a) position A1, 100- to 280-m and 360- to 630-m depth; (b) position A2, 320- to 580-m depth; and (c) position T6, 320- to 580-m depth.

those associated with the strong mistral case of the Mediterranean.

Do plumes entrain on their way down? One would then expect to find cells that widen with depth. An increase of horizontal scale with depth could not be established by analysis of the ADCP beam spreading, and neither was there a significant increase of passage timescale with depth [*Visbeck*, 1995]. This issue remains unresolved on the basis of the presently available in situ measurements.

In summary, convection cells of scales between a few hundred meters and 1 km have been observed by direct measurements at all three major convection sites. Plume scales are in reasonable agreement with the scaling arguments presented above based on the observed buoyancy fluxes (see Table 4). The evidence from the observations suggests that the plumes appear to decay before they become subject to the effects of the Earth's rotation. So far there is insufficient evidence to observe lateral entrainment by plumes, but plumes do not seem to entrain significantly at the bottom of the convective column.

3.4.2. Net vertical mass-flux of a population of convective plumes. A law of vertical heat transport for a collection of plumes was developed in section 3.1. We consider here the role of plumes in the net vertical mass transport and deep water formation rate.

On the large scale, stretching/compression of Taylor columns on the rotating Earth generates horizontal circulation, thus enabling one to relate the net vertical velocity over an area to the time rate of change of the circulation around the patch of ocean:

$$\frac{\partial}{\partial t}\oint \mathbf{u}\cdot dl = f\frac{\overline{\partial w}^{\text{area}}}{\partial z}$$

where $\bar{w}^{\text{area}}$ is the vertical velocity averaged over the patch and f is the Coriolis parameter. Observations in the Gulf of Lions [*Schott et al.*, 1996] suggest that the change in circulation around the periphery of a convection patch over a few days does not exceed 20–30 cm s^{-1}. The above formula then yields a net w of less than 0.1 mm s^{-1}, over a patch 50 km in diameter and 1 km deep. This is a very small vertical velocity, tiny compared with

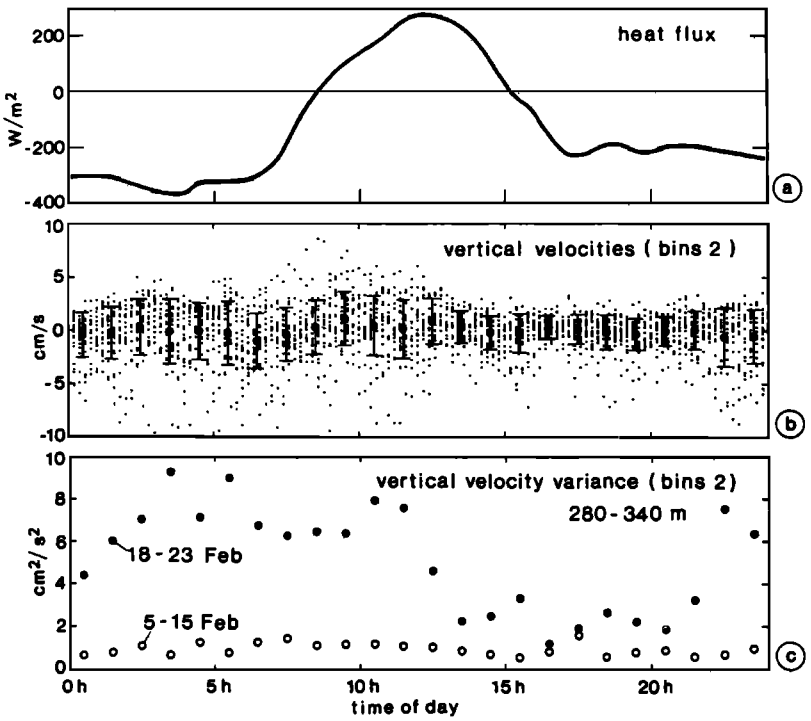

Figure 24. (a) Mean diurnal heat flux cycle during Gulf of Lions convection. February 18–23, 1992; (b) vertical velocity, hourly means, and standard deviations; and (c) vertical velocity variance at 280- to 340-m depth during (February 18–23) and prior to (February 5–15) deep convection showing generation and decay timescales of plumes. (From *Schott et al.* [1996].)

those associated with individual plumes and so small as to be insignificant in the context of deep-water formation. We conclude (the arguments are developed in more detail by *Send and Marshall* [1995]) that the plume scale does not play a significant role in vertical mass transport: downwelling in a plume is almost entirely compensated by upwelling local to that plume. However, the plumes are very efficient mixers of properties (see discussion in section 3.1). This has important implications for the way in which plumes are parameterized in numerical models (see section 5). Evidently, the ultimate sinking of the homogenized column to its neutrally buoyant level occurs on much longer timescales and, we believe, is associated with geostrophic eddy dynamics (Figure 3c). A further implication is that the rates of deep water formation (for example, the number of sverdrups of Labrador Sea Water formed) cannot be computed directly from measurements (or deductions) of vertical velocity w; these are vanishingly small when integrated over the mixed patch. Instead, it is best to relate rates directly to the volumes of homogenized fluid created in the mixing phase.

For example, suppose that convection has created dense water over an area A down to a depth h. The volume created is Ah. Taking, for example, $A = \pi(60\ \text{km})^2$ and $h = 1$ km, values typical of the Mediterranean [see *Send et al.*, 1995], we obtain a deep water formation rate of 1.1×10^{13} m^3 per year. This is ~0.3 Sv, from just one event and in approximate agreement with the observed outflow of deep water through the Strait of

TABLE 4. Comparison of Observed Length and Velocity Scales of Convective Elements, Deduced From ADCP Field Observations, With Scaling Laws Developed in Section 3.3

Parameter	*Labrador Sea (1995)*	*Greenland Sea (1989)*	*Mediterranean (1992)*
Depth of convection, m	1800–2200	800–1500	1100–1500
Buoyancy flux, m^2 s^{-3}	10×10^{-8}	6×10^{-8}	20×10^{-8}
Coriolis parameter, s^{-1}	1.2×10^{-4}	1.4×10^{-4}	0.98×10^{-4}
$Ro^* = \mathcal{B}_0^{1/2}/(f^{3/2}h)$	0.1	0.1	0.4
Nonrotating			
$w = (\mathcal{B}_0 h)^{1/3}$, cm s^{-1}	6.4	4.5	7.7
$l = h$, m	2000	1500	1800
Rotating			
$w_{rot} = (\mathcal{B}_0/f)^{1/2}$, cm s^{-1}	3.2	2.1	5.5
$l_{rot} = (\mathcal{B}_0/f^3)^{1/2}$, m	260	150	560
Observations			
w_{obs}, cm s^{-1}	8	6	10
Plume diameter, m	1000–1500	600–1000	800–1000

Gibraltar [*Bryden and Stommel*, 1984; *Bryden and Kinder*, 1991]. Observed volumes and water mass transformation rates in the Labrador, Greenland, and Mediterranean Seas are reviewed in section 4.1.

3.5. Numerical and Laboratory Studies of Oceanic Convection

3.5.1. Laboratory experiments. Laboratory studies of rotating convection have a long history (see, for example, *Nakagawa and Frenzen* [1955], *Rossby* [1965], and, more recently, *Boubnov and Golitsyn* [1986, 1990], *Fernando et al.* [1991], *Maxworthy and Narimousa* [1994], and the book by *Boubnov and Golitsyn* [1995] and references therein). They can be classified into two broad categories: convection from horizontally homogeneous sources [*Fernando et al.*, 1991] and convection from isolated patches (see the review of *Maxworthy* [1997]). We will postpone a discussion of the latter until section 4.

Fernando et al.'s [1991] rotating experiments from a homogeneous source are in the geostrophic turbulence regime, having an Ra_f in the range of 2×10^{12} to 9×10^{12} and a Ta of 10^9 to 2×10^{11}. The natural Rossby number was not employed by *Fernando et al.* [1991], but we can deduce from their published parameters that Ro^* ranged from 0.0006 to 0.033 in their study and from $\sim 10^{-4}$ to unity in that of *Boubnov and Golitsyn* [1986, 1990].

Fernando et al. [1991] showed that the scaling equations (12) and (13) are appropriate for the nonrotating and rotating (low Ro^*) cases. For the case of horizontally uniform convection, they estimated that the rms velocity and integral length scales of rotationally affected convection is in accord with (13) with scaling factors thus:

$$l = 3.2 l_{\text{rot}} \tag{18a}$$

$$u = 2.4 u_{\text{rot}} \tag{18b}$$

$$b = 1.75 b_{\text{rot}} \tag{18c}$$

The values inferred from numerous other studies are also broadly consistent with (18).

In the rotating case, Fernando and collaborators also found that the convective u and b were independent of depth and time, at least at distances greater than $\sim 5 l_{\text{rot}}$ from the boundary where a heat flux was imposed. Similar experiments were carried out at small Ro^* by *Maxworthy and Narimousa* [1991, 1994] and *Brickman and Kelley* [1993]. Focusing on the first stage of the flow, *Maxworthy and Narimousa* [1994] also found that velocities scaled with u_{rot}. The experiments of *Boubnov and Golitsyn* [1990] also showed that the velocity scale was relatively insensitive to f in the fully turbulent regime.

There remain a number of unresolved issues, however. There is no clear confirmation of the role of l_{rot} in setting the lateral scale of convection; however, see *Helfrich* [1994], *Ayotte and Fernando* [1994], and *Fernando and Ching* [1994], where such dependence is evident in the case of the single plume. *Boubnov and Golitsyn* [1990] present an empirical law for the lateral plume scale, which is dependent on the Rayleigh and Taylor numbers, and has nothing to do with (18).

3.5.2. Numerical experiments. Numerical studies of rotating convection clearly demonstrate the features schematized in Figure 19 and observed in the laboratory (see, for example, Figure 20). Figure 25 shows currents and temperatures in a very high (~50 m) resolution non-hydrostatic numerical experiment 24 hours after vigorous cooling (800 W m^{-2}) was applied at the surface of an initially resting unstratified, rotating ocean where $Ro^* = 0.1$ and $Ra_f = 10^9$ [see *Jones and Marshall*, 1993; *Klinger and Marshall*, 1995]. As the cooling persists, plumes penetrate progressively deeper into the interior, lowering the mean base of the convective layer, and, in time, distribute the influence of intense surface heat loss over the whole depth of the ocean. A linear equation of state (equation (3)) was used, and there was no salt. In Figure 26a the horizontal velocity variance $(\overline{u'^2 + v'^2})^{1/2}$ at day 2 is plotted as a function of depth for this series of experiments, normalized with respect to the nonrotating scaling u_{norot} (equation (12)). Velocities in the (essentially) nonrotating experiment with $f = 10^{-6}$ s^{-1} do indeed scale as u_{norot}: the curve is centered on unity in Figure 26a. However, we see that in the "high-rotation" regime, typical eddy velocities decrease as the rotation rate increases, as is suggested by the scaling (13). Figure 26b again plots $(\overline{u'^2 + v'^2})^{1/2}$ against depth but now normalized with respect to u_{rot} (equation (13)). The normalized velocities from all the high-rotation experiments collapse on to the same line centered on unity; u_{rot} is indeed the velocity scale adopted by the plumes. Note that it is only the velocities in the $f = 10^{-6}$ s^{-1} case (essentially $f = 0$) that appear anomalous when scaled with respect to the rotational velocity u_{rot}.

Laboratory experiments reported by, for example, *Maxworthy and Narimousa* [1994] and *Coates et al.* [1995] suggest that the numerical experiments presented above and those by *Jones and Marshall* [1993] may overemphasize the role played by rotation in oceanic plume-scale dynamics. The consensus of the laboratory experimentalists is that rotational effects are felt only when $Ro^* < 0.1$, rather than $Ro^* < 0.7$ or so in the (rather more diffusive) numerical experiments of *Jones and Marshall* [1993].

Sander et al. [1995] investigate the dependence of plume scaling on numerical diffusivities. As long as the numerical fluid is inviscid enough, the scaling (13) remains pertinent, but the constant of proportionality between, say, the modeled u and the scaled u, u_{rot}, depends on diffusion, as does the transition between rotational and nonrotational regimes. This has some practical relevance because typical values of Ro^* in the ocean are just in this transitional range: $0.1 \rightarrow 1$. It seems that deep convective plumes in the ocean are not dom-

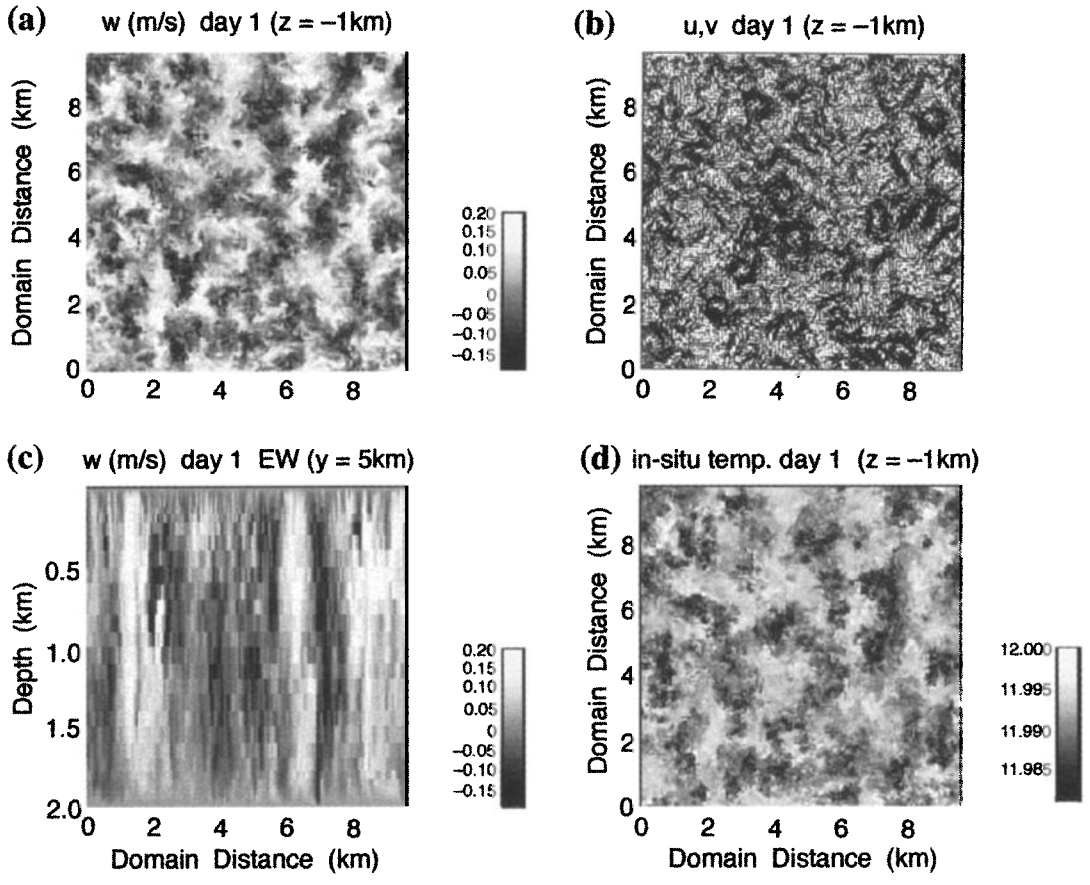

Figure 25. Numerical simulation of convection induced by surface cooling in an initially neutral, unstratified rotating fluid in a 10 × 10 × 2 km doubly periodic box. Fields are plotted after 1 day of integration. The horizontal resolution of the model is 50 m. The vertical resolution varies from 6 m at the surface to 100 m at middepths: (a) horizontal section of vertical velocity at middepths (z = 1 km); (b) pattern of horizontal currents at $z = -1$ km; (c) an east-west section, chosen to pass through the downwelling center apparent at x = 4.5 km; (d) a horizontal section of in situ temperature at middepths ($z = -1$ km).

inated by rotation, but they may be influenced by rotation in important ways (see below).

The approach of *Jones and Marshall* [1993] is that of a large eddy simulation (LES) and uses highly simplified closure assumptions (Laplacian diffusion of heat and momentum with constant diffusivities). Even the most sophisticated LES assume that the turbulence is isotropic and homogeneous, so making gross assumptions about the nature of the small-scale turbulence. (*Mason* [1994] gives a critical review of the method in the atmospheric context; see *Garwood et al.* [1994], *Denbo and Skyllingstad* [1996], and *Paluszkiewicz et al.* [1994] for examples of LES applied to ocean convection.) However, rotating convection is strongly anisotropic, both because of the nature of the plumes, which are stiffened by rotation, and because of the organization of the flow by rotation. The advantage of LES is that simulations with Rayleigh numbers approaching realistic values can be made; its disadvantage is that results obtained using this method may depend on assumptions implicit in the assumed closure hypotheses.

An alternative approach is that of direct numerical simulation (DNS), in which all the dynamically active scales of motion, down to the Kolmogorov scale, are resolved. It is being pursued by *Kerr et al.* [1995] and *Julien et al.* [1996a] but, because of the enormous computational costs, is limited in the range of Ra it can study. However, anisotropies in mixing properties and boundary layer processes can be examined by DNS without any preimposed bias. Because realistic Ra cannot be examined, the DNS approach instead searches for scaling behavior in the solutions and then extrapolates to realistic values, assuming that the flow remains in the same dynamical regime. Studies of Rayleigh-Benard convection using DNS by *Julien et al.* [1996b] push up to $Ra = 10^8$ and $Ta = 10^9$. Although not in a parameter regime directly applicable to the ocean, they nonetheless reveal an important influence of rotation on the dynamics of convective plumes, making them less penetrative than they might otherwise be.

At sufficiently large diffusive timescale compared to advective timescale, convective plumes impinging on

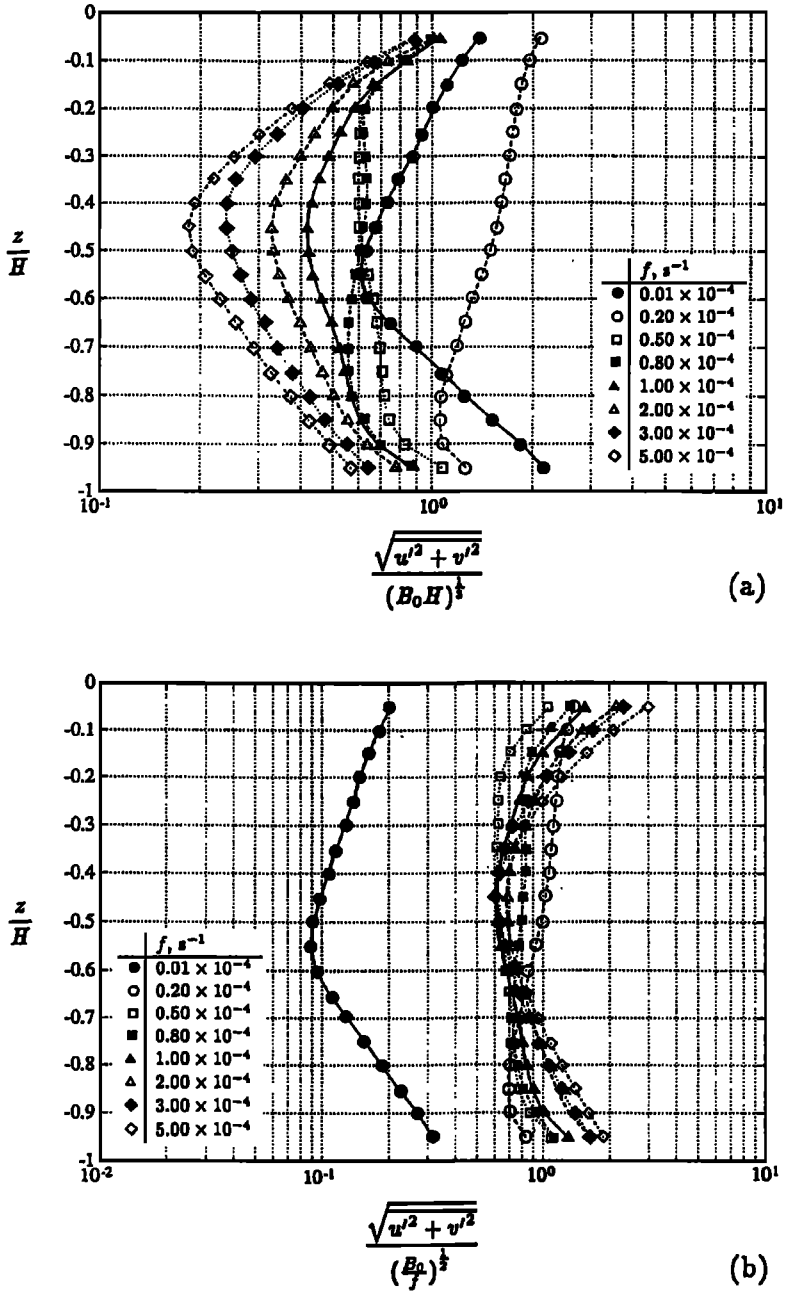

Figure 26. Horizontal velocity variance (a) normalized with respect to the nonrotating scaling u_{norot} and plotted as a function of depth over the convective disk, and (b) normalized with respect to u_{rot} and plotted as a function of depth. From *Jones and Marshall* [1993].

stable stratification may overshoot their neutral buoyancy level and penetrate into the stably stratified region. This may result in entrainment of fluid from below and a reverse buoyancy flux at the base of the convective zone [*Deardorff et al.*, 1980]. This reverse flux can lead to a sharpening of the pycnocline at the base of the mixed layer, a faster rate of deepening of the convective layer, and a transfer of properties between the stable layer and convective layer. Observations, however (see section 3.2.1), suggest that entrainment is not commonly seen at the base of deep mixed layers. The direct numerical simulations of rotating convection by *Julien et al.* [1996a] suggest one possible explanation: they show that rotation significantly decreases entrainment and reduces reverse buoyancy fluxes. The localized cyclonic vortices associated with plumes of low Rossby number lead to a quasi-2-D vortex dynamics, stirring the fluid in horizontal planes (see Figure 27). This enhanced lateral mixing inhibits the vertical transports of density anomalies and leads to the establishment of a finite negative temperature gradient (rather than the homogeneous mixed layer seen in nonrotating convection). The magnitude of the adverse temperature gradient, although enhanced over that seen in the nonrotating case, is rather small, however, for typical oceanographic parameters and conditions [see *Klinger and Marshall*, 1995]. In the field it would be very difficult to isolate from other effects.

We discuss how these results are modified by nonlinearities in the equation of state in section 3.7.

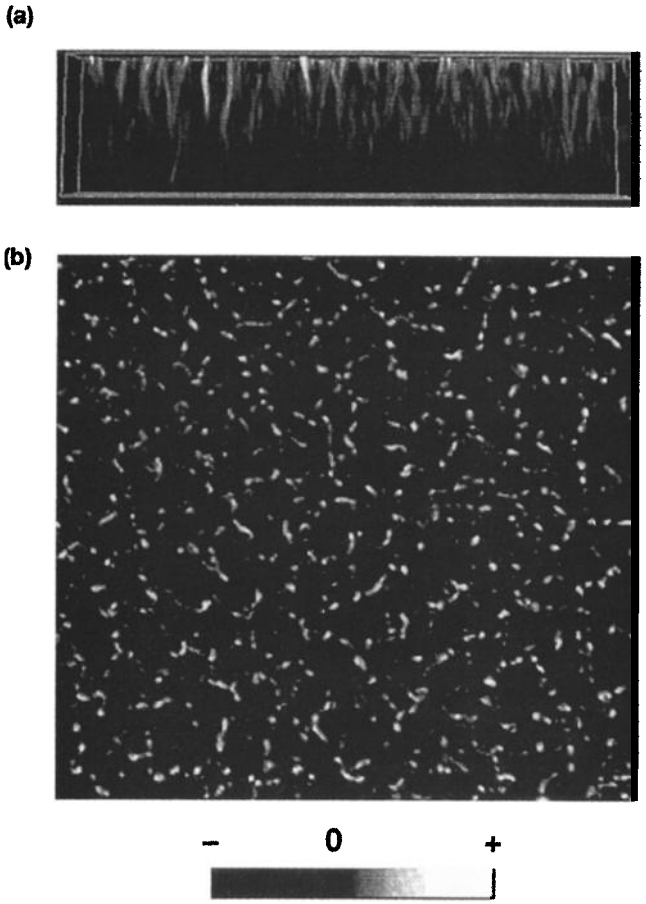

Figure 27. The vertical component of vorticity from direct numerical simulation where the convective Rossby number = 0.21. (a) A vertical section through the convective layer and into the penetration zone. (b) The horizontal section at the top of the convective layer. Cooling corresponding to a flux Rayleigh number of $Ra_f = 1.4 \times 10^8$ is applied at the upper surface, into an initially stably stratified volume. The maximum value on the vorticity scale corresponds to $26f$, where f is the Coriolis parameter. Vertical vorticity is concentrated in surface-intensified, localized cyclonic vortices as a result of fluid convergence into convection plumes. Adapted from *Julien et al.* [1996a] with permission from Elsevier Science.

3.6. Role of Lateral Inhomogeneities

Thus far we have discussed the convective deepening of a mixed layer in the absence of lateral inhomogeneities. In the ocean, however, there are many sources of lateral inhomogeneity, such as lateral shears, fronts, and preexisting eddies. Indeed, the "normal" state of affairs in mixed layers (drawn schematically in Figure 28) is one in which the density varies in the horizontal across the mixed layer (because of more vigorous convection on one side of it than the other, for example). On the large scale, in geostrophic and hydrostatic balance, a "thermal wind" current $u(y, z)$ will develop given by

$$fu_z = -b_y \tag{19}$$

representing the balance between differences in (Coriolis) "overturning forces" (fu_z) and the action of gravity trying to return the b surface to the horizontal ($-b_y$). What are the consequences of the presence of this thermal wind on the convective process?

3.6.1. Slantwise convection. Let us again consider overturning in the (y, z) plane, as sketched in Figure 14, but now in the presence of more generalized rotational and angular momentum constraints (see Figure 28). If there are no downstream (x) variations, then strips of fluid conserve their absolute momentum:

$$m = u - fy \tag{20}$$

where u is the zonal velocity.

If u were zero or a constant then lines of constant m would be vertical: the fluid is stiffened parallel to the rotation vector, and m varies only horizontally. This is the 2.5-D analogue of the rotational stiffness discussed in section 3.3. If m is conserved following fluid elements (here the elements are imagined to be strips of fluid extending in x to $\pm\infty$), then they will acquire a speed $u = -f\delta y$ on moving a distance δy, or u_{rot} on moving a distance l_{rot}, where l_{rot} is the rotational scale given by (13). If fluid sinks in convection the m surfaces are squeezed together at the top inducing cyclonic vorticity, pushed out below generating anticyclonic vorticity there.

Now suppose that the combination of rotation and lateral density gradients leads to a zonal flow in thermal wind balance and so u is not constant. Equation (20) again places important constraints on the convective process. Moreover, the m surfaces are now tilted over if $du/dz \neq 0$, and they will induce fluid particles to move along slanting, rather than vertical, paths; the upright convection of Figure 15 will become slantwise, as is

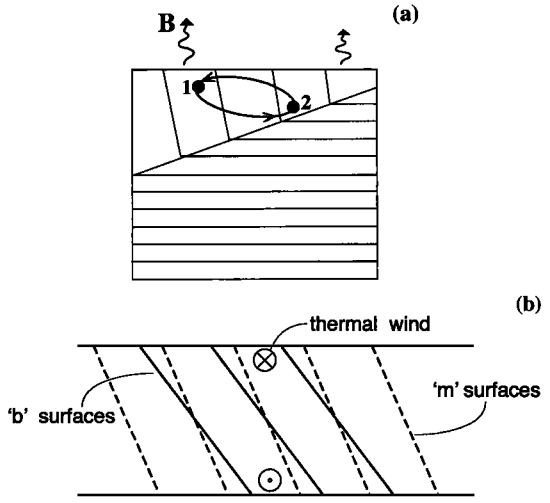

Figure 28. (a) Lateral gradients in mixed-layer depth and density induced by spatial inhomogenities in the buoyancy forcing and/or the preexisting stratification. The mode of buoyancy transfer through the mixed layer can change to one in which fluid parcels are exchanged laterally in, for example, baroclinic instability. (b) Schematic diagram showing angular momentum (m) and buoyancy (b) surfaces in the presence of a thermal wind shear.

sketched in Figure 28b. (In practice, particles may take a "zigzag" route, particularly if the sinking branch is traversed very quickly. Ultimately, however, the particle "realizes" that it is in the "wrong" position and moves across to where its m matches the surroundings.) The stability of the layer will depend on the sign of ∇b measured in the m surface, or the sign of the absolute vorticity normal to the b surface (corresponding to a centrifugal instability). Both viewpoints are complementary and entirely equivalent. *Emanuel* [1994] calls this more general mixed instability "slantwise convection." The stability depends on the sign of the potential vorticity (PV),

$$Q = \frac{1}{g}\eta \cdot \nabla b \tag{21}$$

a measure of the stratification ∇b in the direction of $\eta = 2\Omega + \text{curl } \mathbf{v}$, the absolute vorticity vector, or, equivalently, a measure of η normal to b surfaces.

The present discussion makes it clear that the presence of 2Ω cos (lat) Coriolis terms will also have the effect of tilting over the m surfaces even in the absence of a background zonal flow, because then $m = -fy + az$, where $a = 2\Omega$ cos (lat) is the horizontal component of the Coriolis force [see *Denbo and Skyllingstad*, 1996].

Parcel theory can be readily (and rigorously) employed to analyze the stability of a zonal flow in thermal wind balance to overturning in a vertical plane while conserving angular momentum. It yields exact results (see, for example, *Emanuel* [1994] or *Haine and Marshall* [1998]). It can be shown that, and as is in accord with one's physical intuition, if Q is negative, then the flow is convectively unstable to so-called "symmetric instabilities"; slantwise convection might then be expected to ensue and return the Q of the layer to zero, the state of marginal stability:

$$Q < 0 \Rightarrow \text{convection} \tag{22}$$

Theoretically, then, one has compelling arguments that strongly suggest that (1) if $Q < 0$, then convection will occur, and (2) the end state of the convective process will be one in which $Q \approx 0$. Note, however, that in general, this will correspond to the vanishing of N^2 measured along the m surfaces rather than in the direction of gravity. These ideas are readily borne out in numerical experiments.

Consider again the numerical experiment presented in Figure 15 and discussed in section 3.1.1. We now repeat it but make two changes: (1) we introduce the possibility of rotational control by including f and making the model 2.5-D (y, z) with no x variations, so that zonal strips of fluid conserve angular momentum and (2) introduce a meridional gradient in the cooling to induce lateral buoyancy gradients and so support a zonal wind.

The cooling rate increases across the channel following a hyperbolic tangent variation. Thus there is weak surface forcing in the southern third of the channel, fairly constant densification in the northern third equivalent to a heat loss of 800 W m^{-2}, and a sharp transition in between. A linear equation of state is specified dependent on temperature alone and the resolution is sufficient to represent gross aspects of the convective process. Figure 29a shows the numerical solution after 9 days of cooling of an initially resting stratified fluid in which $N/f = 10$. It is clear from the isotherms and stream function that the overturning motions cause fluid to move systematically in slanting paths and therefore maintain a nonvanishing stratification in the region that is being actively mixed. Here the contours of absolute momentum m are closely aligned with the isotherms, indicating that the potential vorticity (PV) is close to zero. The temperature field alone is ambiguous at highlighting the regions of active overturning. Rather, potential vorticity is the key dynamical variable as shown by Figure 29b. There are distinct plumes, of negative PV, draining the surface source of negative PV into the interior.

The integration was carried on for another 24 hours, but now with the surface cooling switched off. Figure 29c shows that after cessation of cooling the convection rapidly dies away leaving a layer with very small potential vorticity (around 1% of the undisturbed value) but, significantly, nonvanishing vertical stratification. The plumes of negative PV have been mixed away by the symmetric instability, erasing density gradients along absolute momentum surfaces, over a timescale consistent with the prediction of the parcel theory, but leaving the end state vertically stratified.

These ideas help in clarifying, and form a context in which to think about, the effect of convection on the large scale and the parameterization of convection in large-scale models (see section 5).

3.6.2. Switchover from convection to baroclinic instability. We have argued that spatial inhomogeneities in the buoyancy forcing and/or the preexisting stratification induce lateral gradients in mixed-layer depth and density. Now, if the angular momentum constraint of section 3.6.1 is relaxed, the mode of buoyancy transfer through the mixed layer can change to one in which fluid parcels are exchanged laterally in baroclinic instability. Suppose that we perform an experiment identical to that shown in Figure 29 but now in a 3-D domain allowing zonal variations to break the angular momentum constraint. It is found that baroclinic instability ultimately takes over as the primary agency of buoyancy transfer through the convection layer. A typical example of the flow development is shown in the "bird's eye" view of Figure 30. The near-surface fields of temperature reveal a progression from plume-scale convection at day 3 to finite amplitude baroclinic instability at day 6, with a mature field of geostrophic turbulence by day 9. A surface-intensified jet evolves in balance with the across-channel temperature gradient, with the eddying part of the flow dominating. Because there is no stress applied at the ocean surface, the global zonal momentum cannot

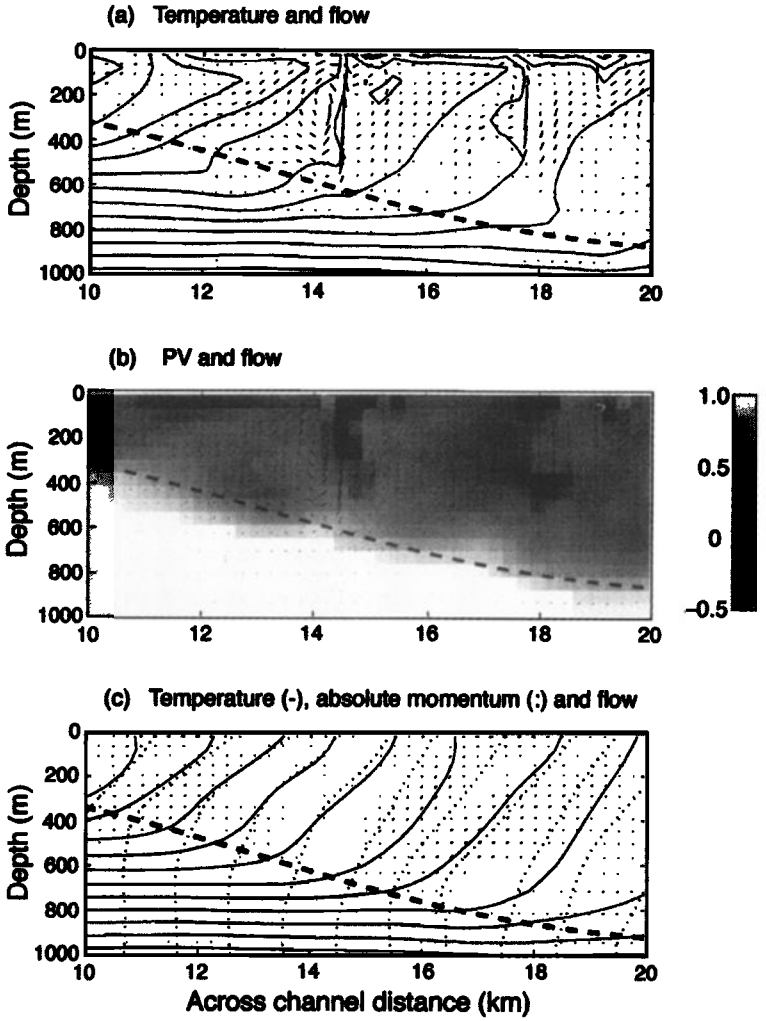

Figure 29. Vertical sections of (a) temperature and (b) Ertel potential vorticity (PV) normalized by the PV of the initial condition, both at day 9, from the 2.5-D integration for the central part of the channel, and (c) the solution at day 10, after the surface cooling has ceased for 24 hours, showing the close alignment of m and b surfaces, indicative of vanishingly small PV. In each figure the flow and 1-D mixed-layer depth are shown as in Figure 14. Peak speeds (v, w) are (0.11, 0.050) m s^{-1} in the (y, z) directions. From *Haine and Marshall* [1998].

change, and eastward flow at the surface is compensated by a westward current below. The length scale for the baroclinic instability at day 6 is ~5 km, somewhat larger than the prediction of *Stone*'s [1970] nonhydrostatic linear instability analysis of ~3 km [see *Haine and Marshall*, 1998]. For typical mixed-layer depths of 200 m, stability analysis predicts, and explicit calculations confirm, that baroclinic waves with length scales of $O(5$ km) develop with timescales of a day or so.

A fascinating and central aspect of the convective process in the ocean, then, is the interaction between convection and baroclinic instability, which we see being played out in Figure 30. As time progresses the fluid finds it more efficient to transfer buoyancy by the latter process rather than the former. Moreover, in the ocean (and unlike the atmosphere) there is no significant scale separation between the convective and the baroclinic eddy scale. Before returning to this theme in section 4, we briefly mention complications that arise from the nonlinearity in the equation of state of seawater.

3.7. Complications Arising From the Equation of State of Seawater

The density of seawater is a rather complicated function of temperature, salinity, and pressure. Often a simplified equation of state of the form (3) can be used. Then, irrespective of whether fresh water or heat fluxes are imposed, the density equation behaves in a symmetrical way. However, this is not always the case, particularly when the water is cold. Then nonlinearities in the equation of state manifest themselves more strongly, and in extreme conditions the water may change phase to form ice (the interaction of convection with ice is outside the scope of the present review, but see *Kaempf and Backhaus* [1998, and references therein] and *Gawarkiewicz et al.* [1997]). In addition, the molecular diffusivity of salt and heat differ by a factor of 100, leading to "double diffusion." We consider now, briefly, how some of these effects may influence and change the "pure" hydrodynamics considered thus far.

3.7.1. Thermobaric effects. The thermobaric effect is the name associated with the pressure dependence of the thermal expansion coefficient α. It is negligible in the Mediterranean Sea, small in the Labrador Sea, but important in the Greenland Sea (see Table 1). For example, evaluation of the equation of state in the roughly 3°C water of the top kilometer of the Labrador Sea shows that $\partial\rho/\partial\theta$ can be approximated to within 12% by a constant value. In colder water, however, such as in

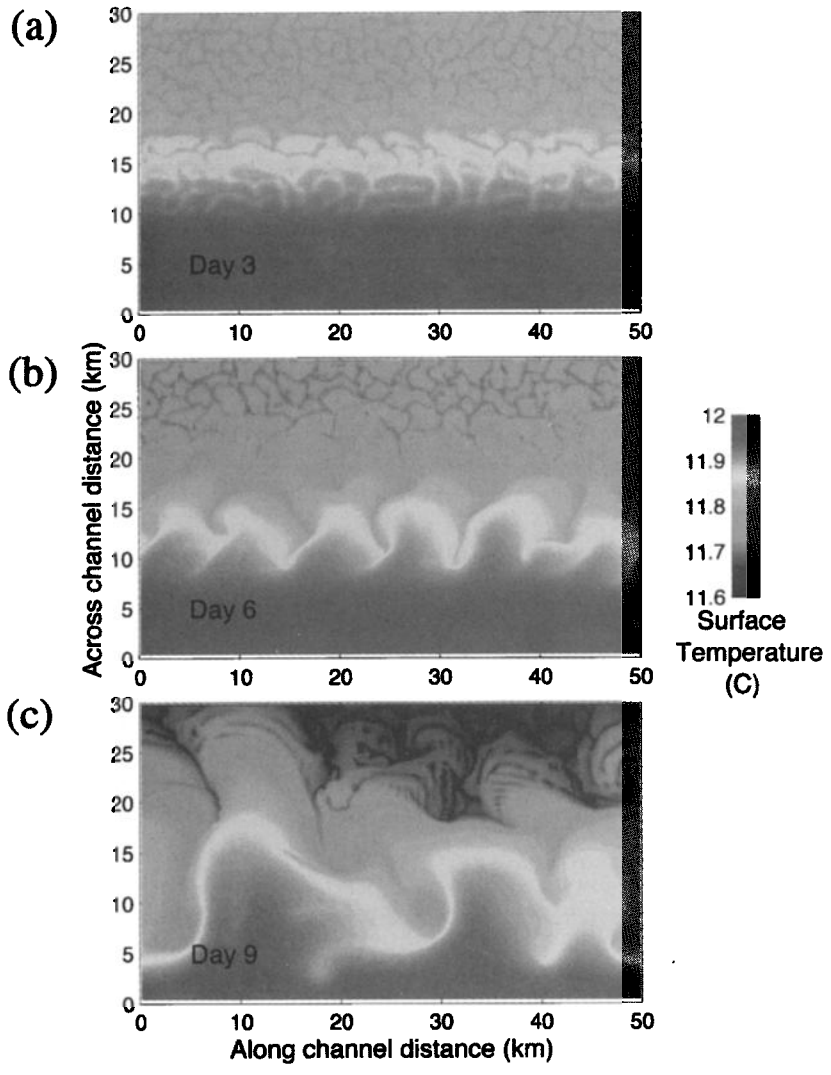

Figure 30. The evolution of the temperature at a depth of 65 m at (a) 3, (b) 6, and (c) 9 days, in which the zonal angular momentum constraint operating in Figure 29 is relaxed. We see the convection evident in Figure 30a give way to baroclinic instability in Figure 30c. The color version of this figure appears on the cover of this issue.

the Greenland and Weddell Seas, $\partial\rho/\partial\theta$ displays a greater sensitivity to pressure.

Gill [1973] and *Killworth* [1979] first recognized the role of thermobaric enhancement of thermal expansion in their calculations/models of hydrostatic stability in the water column in the Weddell Sea. They showed that a plume of saline water could experience an additional decrease in stability as it flows downward because of the thermobaric effect.

Consider, for example, the Greenland Sea. For water with $\theta \approx -1°C$, and $34.8 < S < 35$ psu, typical of the Greenland Sea, a good approximation to the density is (B. Klinger, unpublished manuscript, 1993)

$$\rho = -\alpha'\vartheta + \beta' S - \varepsilon\vartheta p \qquad (23)$$

where α' and β' and ε are constants and constant terms and those that depend on p alone have been subtracted out. The term $-\varepsilon\vartheta p$ in (23) is the thermobaric effect. For water in this range of θ and S, the constants have the value $\alpha' = 0.0329$ kg m^{-3} °C^{-1}, $\beta' = 0.8$ kg m^{-3} psu^{-1}, and $\varepsilon = 0.0306$ kg m^{-3} °C^{-1} (10^7 Pa)$^{-1}$, if p is measured in thousands of decibars (so that a δp of 1 is equivalent to depth change of 1 km), θ is in degrees Celsius, and S is in practical salinity units.

Thermobaric effects make it possible to generate conditional instabilities if salinity stratification is partially balanced by thermal stratification (as is typical in the Greenland Sea, where a cold, fresh layer overlies a warm salty layer). These classes of instability are mathematically analogous to conditional instabilities of a moisture-laden atmosphere (reviewed by *Emanuel* [1994]; see *Garwood et al.* [1994] for a review of thermobaric convection). It appears, though, that such effects are not often driving factors in the water mass transformation process but can act as important modifiers.

Consider, for example, a two-layer fluid in which θ and S jump by an amount $\Delta\theta$, ΔS, across the interface at pressure p_h. From (23) the density jump across the interface is given by

$$\Delta\rho = \beta'\Delta S - (\alpha' + \varepsilon p_h)\Delta\theta \qquad (24)$$

Suppose we displace a particle on one side of the interface by an amount (in pressure) dp, then the difference between the density of the particle and its surroundings

is (again using (23)) $d\rho = -\Delta\rho + \varepsilon\Delta\theta dp$. The condition for thermobaric instability is that $d\rho > 0$ and will occur when

$$dp > \Delta\rho/\varepsilon\Delta\theta$$

which, using (24), can be expressed as (see B. Klinger, unpublished manuscript, 1993)

$$dp_c = \left[\frac{\beta'}{\alpha'}\frac{\Delta S}{\Delta\theta} - \left(1 + \frac{\varepsilon}{\alpha'}p_h\right)\right]\frac{\alpha'}{\varepsilon} \qquad (25)$$

where dp_c is the critical pressure change. For conditions typical of the Greenland Sea, $h = 200$ m, $\Delta\theta = 1.5$°C, and $\Delta S = 0.118$ psu, we find that $dp_c = 78$ bars or 780 m. Thus particles must be displaced a substantial distance to trigger instability in this manner.

Thermobaric effects can readily be detected in numerical simulations of deep-reaching plumes, however. *Sander et al.* [1995] repeat the nonhydrostatic calculations of *Jones and Marshall* [1993] but with a more realistic equation of state and show that thermobaric effects lead to enhanced vertical accelerations in the water column. *Garwood et al.* [1994] and *Denbo and Skyllingstad* [1996], using LES models, also find important modifications to the vertical profile of buoyancy flux in deep polar sea thermal convection.

3.7.2. Double-diffusive convection. The molecular diffusivity of dissolved salt in water is about 100 times less than its thermal conductivity. This can trigger static instability when the vertical heat and salt gradients oppose each other in their effects on density. Because such warm-salty and cold-fresh correlations are so common in the ocean and turbulence is generally weak away from topography, double-diffusive effects are thought to be nearly ubiquitous [*Schmitt*, 1994] and may play a role in water mass transformation. At high latitudes the cold, fresh over warm, salty stratification often observed favors the diffusive-convective instability. In this case a series of thin interfaces alternates with convectively stirred layers to provide an enhanced upward heat flux with only a small salt transport. Numerous observations of such "staircases" have been reported in both Arctic and Antarctic seas. *Padman and Dillon* [1987, 1988] found extensive diffusive layering in the Beaufort Sea and Canadian Basin in the Arctic. *Muench et al.* [1990] report diffusive layering to be a common feature over much of the Weddell Sea. They estimate an upward heat flux of 15 W m^{-2} that helps maintain ice-free conditions in the summer. The effect of such heat loss with little salt exchange is to provide a subsurface cooling of the affected water mass without air-sea exchange. *Carmack and Aagaard* [1973] and *McDougall* [1983] have proposed that this is an important effect for the transformation of Atlantic Water into Greenland Sea Bottom Water. Within the Arctic itself, *Carmack et al.* [1997] have reported on a major recent change in middepth water mass properties because of a strong incursion of warmer, saltier Atlantic Water. This is likely a result of double-diffusively driven lateral intrusions, which can be traced for distances greater than 2000 km across the basin. The water mass transformations caused by double diffusion within the Arctic Basin may play an important role in preconditioning the waters exported through Fram Strait to the convection region of the Greenland Sea.

Another role for the diffusive-convective instability arises when a layer of cool, fresh water "caps off" the upper ocean. This is a common situation in the high-latitude ocean, where coastal runoff and ice melt can have a major impact on near-surface stratification. As a fresh water cap is progressively cooled by winter heat flux, the potential for diffusive convection at the base of the mixed layer increases. Because the double-diffusive process transports heat but not much salt, it has a stabilizing effect on the stratification. This may prevent or delay the convectively driven deepening of the mixed layer that would be expected in the absence of diffusive convection. An implementation of this effect in a 1-D model improved agreement between it and the observed evolution of mixed layer temperature, salinity, and depth in a winter-cooled warm-core ring [*Schmitt and Olson*, 1985]. Only a few preliminary efforts to incorporate such processes in larger-scale circulation models have been made [*Zhang et al.*, 1998], though *Kelley* [1990] provides a suitable parameterization.

4. DYNAMICS OF MIXED PATCHES

The plumes reviewed in section 3 act in concert to homogenize an extensive patch of ocean. We now review what is understood of the dynamics of the mixed patch as a whole. The defining feature of homogeneous patches is that properties (such as T and S) are mixed by convection, leading to a local diminution of property gradients interior to the patch but an enhancement of gradients around the periphery (see the schematic diagram in Figure 3). This localization in space makes the problem distinct from the myriad classical studies of convection rooted in the Rayleigh problem (convection between two plates extending to $\pm\infty$); as one might anticipate, in the ocean edge effects ultimately come to dominate the evolving flow fields. Large horizontal buoyancy gradients on the edge of the convection patch support strong horizontal currents in thermal-wind balance with them: the "rim current." If the patch has a lateral scale greater than the radius of deformation, then baroclinic instability theory (see section 4.3.2) tells us that it must break up into Rossby-radius-scale fragments. We shall see that baroclinic instability plays a dominant role in the dynamics and thermodynamics of the mixed patch, orchestrating the exchange of fluid and buoyancy to and from it. Indeed one can consider the process of water mass transformation in deep convection as an extreme example of the "switchover" from convection to baroclinic instability introduced in section 3.6.2.

After reviewing some of the relevant observations, we

consider the overturning of a neutral, rotating fluid to an extended but localized loss of buoyancy. We then go on to consider the same problem but in a stratified rotating fluid.

4.1. Observed Volumes and Water Mass Transformation Rates

Here we review what is known of the scales, volumes, and water mass transformation rates that are associated with mixed patches. As was emphasized in section 3.4.2, a deep mixed patch is not akin to a chimney, in which a downdraft carries water to deep layers. Rather, it is a volume of water mixed by the action of convection. The rate at which a water mass is formed in a transformation event is thus related to the volume of the mixed patch that is subsequently absorbed into the surrounding waters via geostrophic eddy exchange and deep boundary currents. In a typical winter, perhaps only one deep-mixing event occurs per region and regime, but occasionally a previously mixed site that has already partially exchanged its properties is stirred up again.

4.1.1. Labrador Sea. In the Labrador Sea, monitoring of convection over many years occurred at *Bravo* (Figure 5, site B), but that did not yield information on the lateral extent of the deep-mixed regime. However, during February and March 1997, R/V *Knorr* conducted an extensive hydrographic survey of the Labrador Sea during a period of active convection as part of the Labrador Sea Convection Experiment [see *LabSea Group*, 1998]. The spatial variability in the CTD casts was remarkable. Intrusions were prevalent, and often the downcast trace would differ significantly from that of the upcast. Some of this rich structure may be due to the proximity of the convection to the boundary, where strong contrasts exist between resident water masses (R. Pickart, personal communication, 1997).

In recent years, several repeats of the WOCE AR-7 hydrographic sections have been carried out, which runs through *Bravo* across the Labrador Sea to Greenland. They reveal large mixed patches, of about 500 km in lateral extent (J. R. Lazier, The Labrador Sea after winter convection: 1990–96, submitted to *Journal of Physical Oceanography*, 1997), but these surveys all took place in the summer, many months after mixing occurred (see Figure 7). In 1976, *Clarke and Gascard* [1983] observed a smaller patch of about 200 km in scale when production was low. Combining with observations from 1978, they estimated that the extent of the patch in the alongshore direction was ~450 km (marked in Figure 5). With a depth of 1750 m this gives a volume of 1.2×10^{14} m^3, corresponding to a transformation rate of 3.9 Sv over the year. This estimate is similar to *Wright*'s [1972] deduction of the transformation rate based on heat budget considerations, who obtained 3.5 Sv. *Worthington* [1976] estimated that a volume of water of 6×10^{13} m^3 is cooled every year to below 4°C, which yields a somewhat smaller transformation rate of 2 Sv.

If the deep mixed patch of the early 1990s was of cylindrical shape with a diameter of 500 km and a depth of 2 km, then a water mass of volume 3.8×10^{14} m^3 is transformed, and if this is taken as annually released LSW, the flux would amount to 12.7 Sv. This is an upper limit, appropriate to the period of extremely active LSW thickness and production of the early 1990s. Furthermore, as shown by the summer AR-7 sections, LSW is not "flushed out" each year; subsequent winter convection acts on previously formed LSW, reducing the average annual transformation rate.

4.1.2. Greenland Sea. In the Greenland Sea, deep convection was not active during the 1980s, when intense surveys were made. Indirect evidence from the active convection period of the 1970s, for example from tracer concentrations, has allowed estimates of renewal times to be made [e.g., *Schlosser et al.*, 1991] and these have been compared with those of the subsequent quiescent period [*Rhein*, 1991]. However, direct evidence of the extent of convection regimes is sparse. The 1989 preconditioned patch within which individual plumes subsequently developed is sketched in Figure 8. In 1996 a small patch of about 30-km scale was observed near 75°N, 3°W (J. Backhaus, personal communication, 1997). As was discussed in section 2.2.2, the existence and extent of Greenland Sea deep-mixed regimes are confined to the limits of the Nord Bukta. Transformation rates from the Greenland Sea Project (GSP) surveys of 1989 are still being deduced (J. Meinke, personal communication, 1997).

4.1.3. Mediterranean Sea. The logistical advantage of the closeness of the Gulf of Lions convection regime to the southern coast of France has permitted several observations of the scales and winter development of the deep-mixed regime in different years. Extents of the deep-mixed patches observed in 1969, 1987, and 1992 are sketched in Figure 9. The mixed patch created in 1987 must have been a record one because it occurred in the year of greatest winter heat loss during the past three decades [*Mertens and Schott*, 1998]. However, the observation was taken during February 17–23, when a second mistral had reopened the stratification, which had been evolving from a mixing event associated with the mistral of January 10–12, 1987. In early February, between the two mistrals, the surface expression of the homogeneous water mass had shrunk to about half of the size sketched in Figure 9 [*Leaman and Schott*, 1991]. From hydrography taken in 1992, the volume of transformed water masses was estimated to be 1.5×10^{13} m^3 [*Schott et al.*, 1994]. Inferences from acoustic tomography suggested a lower value of 0.95×10^{13} m^3, however [*Send et al.*, 1995]. These values correspond to 0.5 Sv and 0.3 Sv of annual renewal, respectively.

Recently, *Krahmann* [1997] estimated the water mass transformation rates by calculating a water mass census from a newly composed hydrographic climatology of the western Mediterranean. He estimated a deep water production rate in the northwestern Mediterranean of $1.8 \pm 0.6 \times 10^{13}$ m^3 yr^{-1}, corresponding to 0.6 ± 0.2 Sv. The newly formed deep water comprises 1.3×10^{13} m^3 of

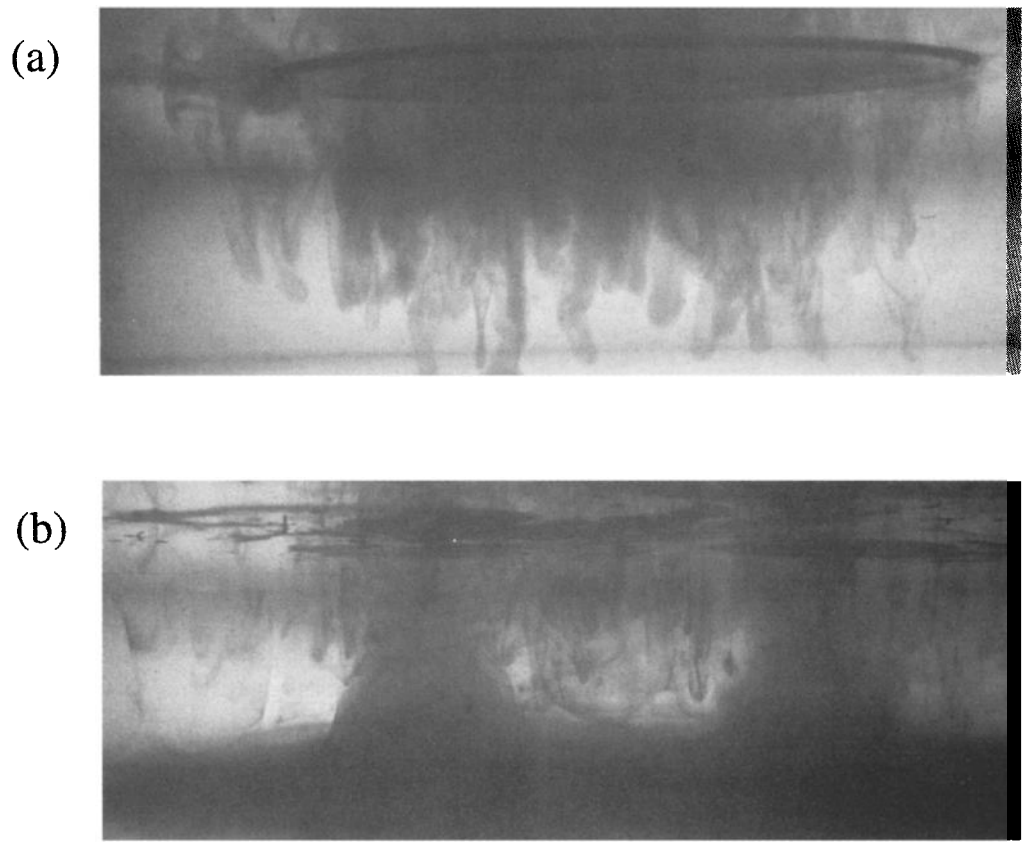

Figure 31. (a) Side view of plumes descending from the disc at the surface under rotational control. This is the most rapidly rotating melting-ice experiment, with $Ro^* = 0.03$ and a 15-s rotation period. (b) Cones marked by dye showing the geostrophically adjusted end state of the convective process after ice has melted and hence cooling has ended.

Levantine Intermediate Water and 0.5×10^{13} m^3 of Modified Atlantic Water. Earlier, *Bethoux* [1980] estimated 1.35×10^{13} m^3 from the evaluation of the then sparser hydrographic database.

4.2. Mixed Patches in Numerical and Laboratory Experiments

In section 3 we described experiments in which convection was induced by uniform buoyancy loss at the surface of the fluid. Here we consider the problem in which convection is induced by an extended but finite patch of cooling.

4.2.1. Mixed patches in unstratified fluids. Studies of the convective overturning of neutral fluids are of importance because they enable one to focus on the role of rotation in isolation from stratification effects. They also have some practical oceanographic relevance because deep convection sites are (almost by definition) rather weakly stratified and well mixed (see section 3.2.1). We shall see that Ro^* emerges again as a key nondimensional parameter of the "patch," along with r/H, a measure of the aspect ratio of the convection patch of lateral scale r and depth H.

4.2.1.1. Laboratory analogues: Convection induced by disk-shaped sources has been studied by *Brickman and Kelley* [1993], *Maxworthy and Narimousa* [1994], *Whitehead et al.* [1996], *Coates and Ivey* [1997], and *Narimousa* [1997], all being motivated, in part, by the oceanographic context. Because of its simplicity (it can be carried out at home using a record player as a turntable and a dyed melting ice disk as a source of buoyancy loss), we now briefly describe a series of experiments performed by J. Whitehead and B. Racine in Woods Hole in 1991. They are described in more detail by *Marshall et al.* [1994].

A disc of colored ice was gently floated on the surface of a rotating tank of water 10 cm or so deep. Convection cells were observed to form and extend to the bottom beneath the ice (see Figure 31a). As the ice melted, small eddies formed and migrated away from the edge of the ice. The melting of the ice induced a buoyancy loss of $\mathcal{B}_0 \approx 6 \times 10^{-6}$ m^2 s^{-3} and with rotation rates of 15 s or so, a rather small $Ro^* = 0.03$. Other rates of rotation were used ranging Ro^* up to a value of unity, the range of interest in the ocean (see Table 3).

By the time the ice was completely melted, the cooled fluid had broken up in to about half a dozen eddies that continued to spread apart with time. A side view of the dyed water is shown in Figure 31b. The eddies are conical in shape, with cold water (tagged with dye)

spreading out over the bottom but "contained" by rotation. Above each conical eddy, pronounced counterclockwise (cyclonic) circulation was observed, with little circulation in the convected fluid itself. This picture is consistent with the upper cyclonic circulation being associated with a low pressure that "holds up" the placid lens of dense fluid. On the large scale, cyclonic circulation built up around the periphery of the ice, and simultaneously, anticyclonic circulation started to develop at the bottom. This is readily understood from a consideration of angular momentum and its conservation because fluid flows inward near the top and outward below. One of the important messages to be taken from this experiment is again that "chimney" is a misleading name: the convection site does not function as a pipe down which fluid flows and thence spreads laterally away. Rather, the plumes act as mixing agents, churning the column vertically. On scales somewhat (but not much) larger than the plume scale, however, rotation has a controlling influence, and the lateral spread of the dense body of convected fluid is constrained almost immediately by the Earth's rotation. The "spreading phase" is a geostrophic process in which baroclinic instability is one of the key mechanisms.

In another important study, *Maxworthy and Narimousa* [1994] combined laboratory experimentation with scaling arguments to determine the size and velocity scales of newly formed baroclinic vortices (the cones seen in Figure 31b) generated by surface buoyancy loss over an extended but finite patch. Salty water was introduced over a central circular region using a shower head so that the convectively processed water could escape the forcing and geostrophically adjust under rotation and gravity, mimicking the fate of convected fluid.

Maxworthy and Narimousa [1994] argued that after convection has ceased, convectively modified fluid is found in geostrophically adjusted cones, the remnants of the mixed patch broken up by baroclinic instability into radius-of-deformation-scale fragments. The aspect ratio of the cones of dense fluid, l_{cone}/h, scales with the (square root of the) natural Rossby number of the system thus:

$$\frac{l_{\text{cone}}}{h} \approx \frac{l_\rho}{h} = \frac{1}{h}\frac{(g'h)^{1/2}}{f} = \frac{\mathcal{B}_0^{1/4}}{f^{3/4}h^{1/2}} = Ro^{*1/2} \qquad (26)$$

where g', the reduced gravity, has been assumed given by b_{rot} from (13c) and Ro^*, depending only on "external" parameters, is the natural Rossby number discussed in section 3.3.2).

The experiments of *Maxworthy and Narimousa* [1994] ranged Ro^* from 0.08 to 1.0, spanning the oceanographically relevant range. The slope of the experimental data could be rationalized in terms of the scaling arguments reviewed in section 3.3. In particular, it was found that the velocity and space scale of eddies shed by the baroclinically unstable, convectively driven vortex could be expressed as a function of Ro^*, consistent with predictions of baroclinic instability theory and the numerical experiments of *Jones and Marshall* [1993] (see below). The experiment also provided constants of proportionality that depend on the nature of the (rotationally influenced) entrainment process.

These laboratory experiments have been followed up and extended by *Brickman* [1995], who studies the temperature of the mixed patch at equilibrium and its dependence on external parameters; we return to this important aspect in section 4.3.3.

Note that these studies adopt aspects of the scaling reviewed in section 3 for an infinite cooling patch, even though the convection patch is of finite size. However, recent experiments by *Coates and Ivey* [1997] and B. M. Boubnov and H. J. S. Fernando (private communication, 1997), suggest that the u_{rot} and l_{rot} scaling (equation (13)) may not be entirely appropriate in the case of cooling over an extended but finite patch. Moreover, both groups find that background rotation indeed affects convective turbulence even when the Rossby number defined in terms of turbulent velocity and length-scales is of $O(1)$.

The reason that the l_{rot} and u_{rot} scales might be modified in the case of convection from isolated sources is the strong horizontal exchange of fluid between the convective region and the ambient fluid, thus imposing the size of the patch r as an additional variable. The experiments of Boubnov and Fernando (private communication, 1997) show that even in the absence of rotation, the scaling under convecting patches is different from that of the horizontally homogeneous case because of strong entrainment flow from the edges of the patches. They suggest that the velocity scale is $(\mathcal{B}_0 r)^{1/3}$, rather than typical free convective scaling $(\mathcal{B}_0 h)^{1/3}$ (equation (12)). Similar scaling needs to be developed for the rotating case, where there is strong lateral exchange because of baroclinic instabilities shed from the convective region [*Jones and Marshall*, 1993; *Maxworthy and Narimousa*, 1994; *Whitehead et al.*, 1996]. To this end, the experimental data of *Coates and Ivey* [1997] will be of utility.

4.2.1.2. Numerical analogues: Numerical simulations of the creation and evolution of patches of mixed fluid in neutral ambient conditions have been carried out using nonhydrostatic ocean models (see, for example, *Jones and Marshall* [1993], *Send and Marshall* [1995], and *Marshall et al.* [1997a]). The implied flux Rayleigh number Ra_f is 10^9, and the Taylor number Ta ranges between 10^2 and 10^8, placing these experiments in the fully developed turbulence–geostrophic turbulence regime (regions 3 and 4 of *Fernando et al.* [1991, Figure 1]). As in the simulations of convection driven by spatially uniform cooling presented in section 3.5.2, the grid spacing of the model is small enough that gross aspects of convective plumes themselves can be resolved. In contrast to those simulations, however, cooling occurs over a patch, and the domain of integration is sufficiently large to permit a study of both the influence of the

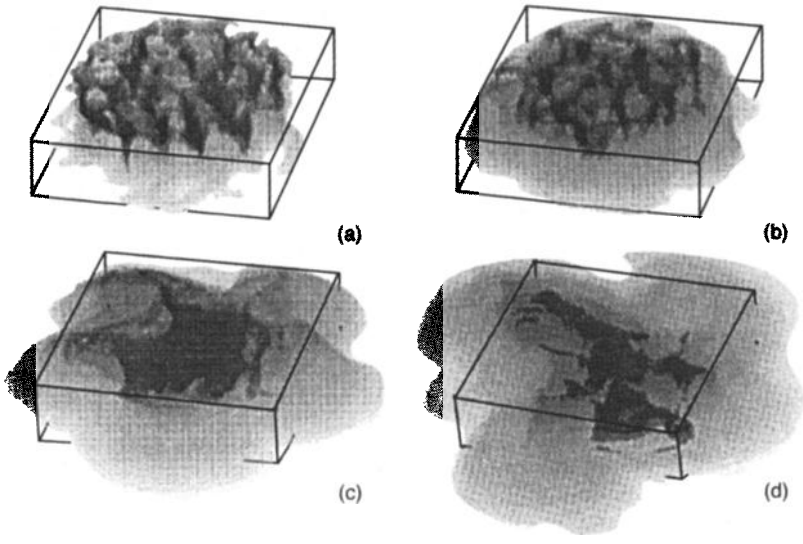

Figure 32. The temperature field rendered in three dimensions at (a) 1 day, (b) 2 days, (c) 4 days, and (d) 6 days, showing the evolution of an initially homogeneous patch of ocean cooled over a 16-km disc at its surface. Cold water is dark, warmer water lighter. As an aid to perspective, a box 16 km on the side and 2 km deep has been outlined.

plumes on the large scale and the geostrophic adjustment/baroclinic instability of the convected water as it moves out of the formation region. An example is presented in Figure 32 simulating the overturning and break-up of a mixed patch. A buoyancy loss of $\mathcal{B}_0 = 4 \times 10^{-7}$ m^2 s^{-3} (corresponding to a heat loss of 800 W m^{-2}) was applied over a 16-km disc centered at the surface of a 32-km, doubly periodic, 2-km-deep ocean. The implied Ro^* is 0.1. The water was initially homogeneous with a linear equation of state dependent on temperature alone.

The sequence of events (sinking in plumes and the subsequent spreading of the convected water in baroclinic structures) can be readily seen in Figure 32, where the temperature is rendered in three dimensions at various stages in the developing mixed patch, resulting in images reminiscent of those obtained in the laboratory using dye (see, for example, Figure 31). As in the laboratory, the combined effect of the plume-scale convection is to drive an increasingly strong, large-scale rim current around the disk of cooling, cyclonic at the surface and anticyclonic beneath. This rim current serves to confine the convected fluid to the volume defined by the disk of cooling. Fluid outside the mixed patch is unmodified, and there is little lateral transfer of fluid between the overturning and the non-overturning regions. By day 2, however, there is evidence of the growth of meanders in the rim current as it becomes baroclinically unstable, an instability that eventually leads to the breakup of the patch of convected water and lateral exchange of fluid with the surroundings. By day 4 the patch of homogenized cold water has broken up into a number of distinct conical structures extending through the depth of the model ocean. These cones have a definite space and velocity scale.

From studies of a number of laboratory and numerical experiments support for the parameter dependence suggested by (26) is found and the constant of proportionality found to be:

$$\frac{l_{\text{cone}}}{h} \approx 5Ro^{*1/2} \tag{27}$$

in accord with the study of *Maxworthy and Narimousa* [1994]. This formula can be used to successfully predict, for example, the scale of the cones produced by the melting ice experiment described in section 4.2.1.1. The scale $l_\rho = hRo^{*1/2}$, is tabulated in Table 3 as a function of the buoyancy flux $\mathcal{B}_0$ for an ocean of depth $h = 2$ km and $f = 10^{-4}$ s^{-1}.

4.2.2. Mixed patches in stratified, rotating fluids. We now consider the evolution of mixed patches forming in initially stratified fluid. Now, in addition to Ro^* and r/H, another nondimensional number, N/f, plays an important role. Here N, the Brunt-Väisälä frequency of the ambient fluid, is measured against f. If N/f is large enough, deepening of the mixed patch can "bottom out" before it feels the bottom, as is often the case in nature. Here we describe some relevant idealized experiments; theory to explain and quantify them is presented in section 4.3.

4.2.2.1. Mixed patches in laboratory experiments: *Whitehead et al.* [1996] (see also *Narimousa* [1996, 1997]) report on a set of laboratory experiments in which buoyancy loss is prescribed over a patch at the surface of a rotating, stratified fluid (see Figure 33). The convective layer penetrated rapidly downward in the early part of the experiment. The dye would typically collect under the source as a rapidly deepening mixed region. After some time, however, the rate of advance of the layer slowed markedly but generally never entirely ceased for the duration of an experiment. Usually, when the advance slowed, the side view revealed considerable lateral slumping of the sides of the dyed region. As time progressed, the patch of dense dyed fluid broke in to a number of eddies, thus arresting the deepening of the mixed patch (see the side view in Figure 33). Much quantitative information was obtained from dozens of such experiments and interpreted in terms of the theo-

retical ideas set out in section 4.3. First, however, we mention parallel numerical studies that have helped shed light on the problem.

4.2.2.2. Mixed patches in numerical models: *Killworth* [1976] realized that mixed patches ought to be susceptible to baroclinic instability and carried out stability analyses of mixed patches to predict the expected scale and growth rate (see section 4.3.2). He reported on attempts to numerically study the breakup of the patch but, for reasons that are not clear, was unable to obtain numerical solutions that exhibited breakup.

The deepening of a mixed layer into an initially stratified, resting fluid was studied numerically by *Jones and Marshall* [1993], as illustrated in Figure 34. Using a fully nonhydrostatic model, they attempt to resolve both the convective and geostrophic scales. As in the laboratory, buoyancy is extracted from the surface over a disc of radius r at a rate $\mathcal{B}_0$. In this calculation, cooling at a rate of 500 W m^{-2} was imposed over a disc of 30-km radius. Initially, the mixed layer deepens by the action of plumes at a rate close to that given by a nonpenetrative convection model (equation (10)). However, just as in the laboratory experiments, as rotation takes over and baroclinic instability sets in, the deepening of the mixed layer is arrested as baroclinic eddies sweep the convected fluid away sideways and draw stratified waters in from the side. The developing eddies can be readily seen in Figure 34.

This line of investigation has been carried further by *Alverson and Owens* [1996], who model the evolution of

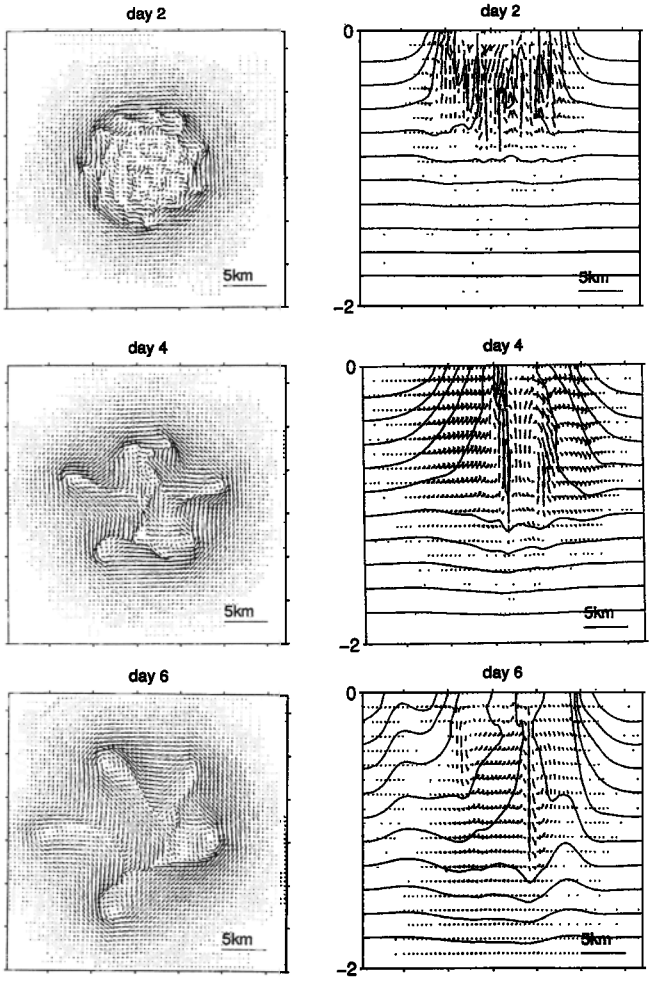

Figure 34. A numerical simulation of a mixed patch induced by a localized but extended patch of cooling applied to the surface of a resting, stratified ocean at days 2, 4, and 6. Plan views at the surface are shown on the left, with hydrographic sections through the evolving mixed patch on the right.

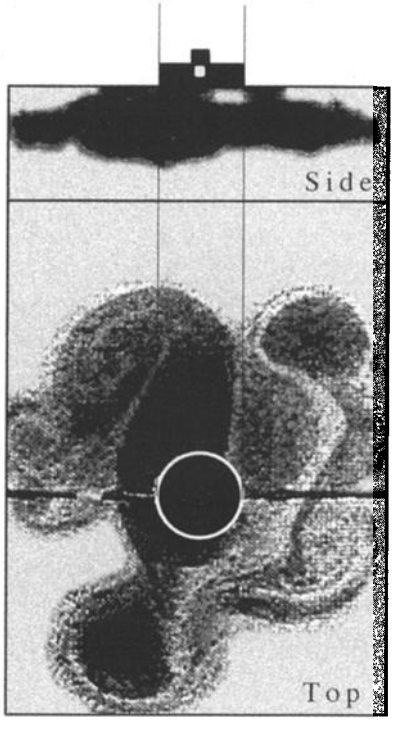

Figure 33. Side and top photographs of the dispersal of convected fluid from away an evolving mixed patch in a linearly stratified laboratory fluid. From *Whitehead et al.* [1996].

a mixed patch trapped over a topographic feature in the presence of a large-scale current (see also *Alverson* [1997]). These may be important factors in the convection sites of the western Mediterranean (preconditioning by the Rhône Fan [*Hogg*, 1973]) and in the Weddell Gyre.

Crepon et al. [1989] and collaborators have used hydrostatic models together with a convective adjustment scheme (see section 5.1.1) to model the formation of deep water in the Gulf of Lions (see Figure 35). Starting from an idealized preconditioned state, *Madec et al.* [1991] were able to obtain deep water with realistic T and S characteristics. Moreover, they demonstrated the impact of meanders generated by baroclinic instability of the mixed patch and its role in advecting lighter waters from the periphery into the convection zone, restratifying the mixed patch at the surface, and inhibiting deep convection. *Madec et al.* [1991] also studied the impact of the variability of the forcing and resolution effects.

Finally, we discuss mixed patches in a numerical model that attempts to remain faithful to some of the

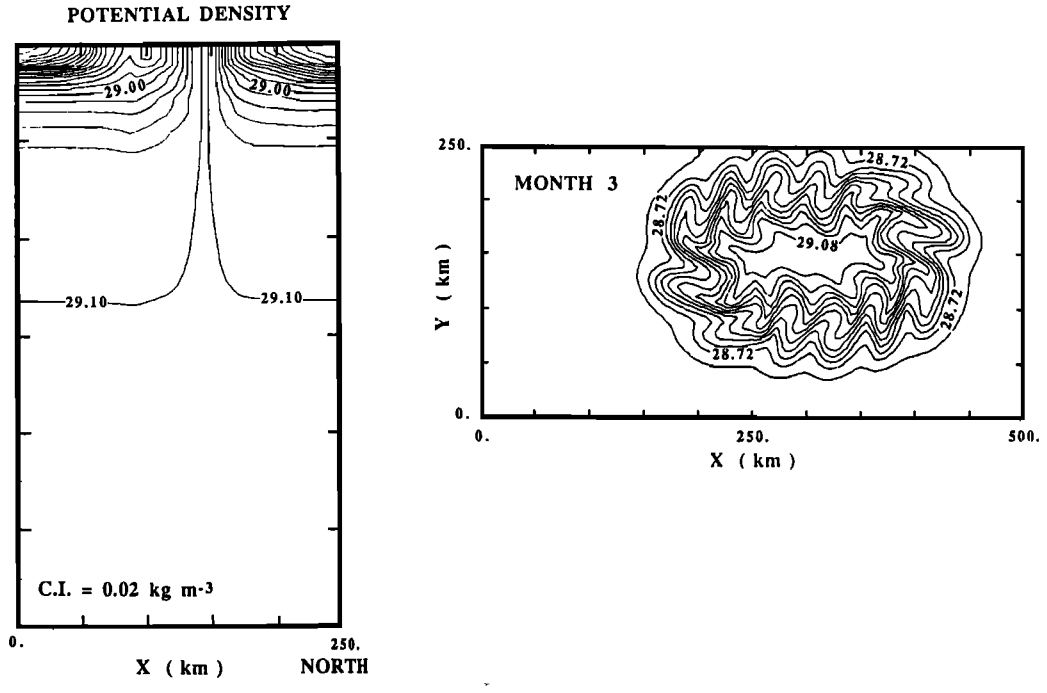

Figure 35. (left) North-south vertical section of potential density induced by a cylindrical patch of cooling after 3 months of integration. (right) Horizontal section of potential density at a depth of 225 m (just above the LIW layer) at the same time. From *Madec et al.* [1991].

geographical detail of one of the important formation regions. Figure 36 shows the pattern of surface currents, mixed-layer depth and a hydrographic section through a mixed patch in the Labrador Sea during March, as captured in a limited area numerical model [see *LabSea Group*, 1998]. The model [*Marshall et al.*, 1997b] was configured with realistic geometry and topography with sufficient horizontal resolution (0.1°) to capture the baroclinic instability of the mixed patch, as is evident in Figure 36b. The mixing by convection cannot be resolved on such a coarse grid and so must be parameterized. A convective adjustment scheme of the kind discussed by *Klinger et al.* [1996] was used; we discuss the rationale behind it in section 5. The model was initialized from a climatological hydrographic data set and driven by twice-daily fluxes of heat, fresh water, and momentum taken from National Meteorological Center (NMC) analyzed fields during a period August 1991 to August 1992. The lateral boundary conditions on the depth-integrated transport were supplied by a 1° global integration of the same model (see section 5 and Figure 47) which itself was driven by twice-daily fluxes over a much longer period from 1979 to 1996.

Figure 36 indicates that many of the features we have been discussing from an observational and, in idealized abstractions, a theoretical point of view, are not obscured by geographical detail. We see an extensive patch of ocean within which properties are remarkably uniform, surrounded by a region of enhanced gradients and strong currents. The rim current and the mixed patch are undergoing vigorous baroclinic instability, which, we will argue, are important in orchestrating the exchange of fluid to and from the patch.

4.3. Theoretical Considerations

4.3.1. Local circulation induced by convection. Mixed patches observed at each of the convection sites of the world ocean have certain common features despite many differences of regional detail: they are surrounded by rim currents, are more cyclonic at the surface than below, and are characterized by doming isopycnals and vigorous eddy activity within and on the edge of the mixed patch. Here we attempt to discuss these general features in the context of, and as a consequence of, the modification of the large-scale potential vorticity field by the convective process.

We have seen how convection in the ocean, as well as convection studied in laboratory and numerical fluids, overturns a previously stratified fluid, mixing away property gradients to create a volume of "convectively processed" water that is very homogeneous in its properties. The stratification is reset to very small values over large areas. It is highly instructive to consider the convective process and the subsequent evolution of the mixed patch from the perspective of the potential vorticity Q, the fundamental property of a rotating, stratified fluid. The potential vorticity has a direct influence on, and is intimately connected to, the hydrodynamics. Insights gained from this PV perspective illuminate the observations

(and models) and motivate simple theoretical abstractions, which point to parametric representations of both the convective (mixing) scale and the eddy (stirring) scale. They thus provide an important theoretical backdrop to the more pragmatic issues of parameterization of section 5.

If on the small scale the convective process sets (in a violent mixing process) the potential vorticity to zero (as discussed in section 3.6.1) and, in the aftermath of convection, fluid now "tagged" with zero Q evolves quasi-adiabatically, what are the consequences for the large scale? To answer that question we invoke the "invertibility principle" [*Hoskins et al.*, 1985]. If the large-scale flow is in geostrophic and hydrostatic balance, then on entering the geostrophic and hydrostatic relation in to (21), Q can be expressed in terms of the pressure field through an elliptic operator. This Q field can then be inverted, subject to boundary conditions, to yield the influence of convection on the large scale.

The top panel of Figure 37a shows the expected Q distribution of a mixed patch schematically, just after convection has ceased. The mixed patch, made up of convected fluid is imagined to have $Q = 0$, and the sea surface is dense; outside of the mixed patch the ambient fluid has $Q = Q_{\text{ref}}$ and the sea surface is at its ambient density. The inverted b and v_g implied by the PV distribution are shown in the middle and bottom panels, respectively.

We see that the highly idealized Q distribution shown in Figure 37a does indeed induce a large-scale flow that has many of the characteristic features of observed and numerically simulated mixed patches. There is a rim current, strong and cyclonic toward the surface, somewhat weaker and anticyclonic below, circumscribing a large, mixed pool of fluid. On the edge of the homogenized pool, isopycnals arch upward to the surface over a lateral scale of the deformation radius Nh/f. Thus by invoking the "invertibility principle," we see that if the convective process mixes Q away to 0, it must induce large-scale flow much as is observed (see, for example, Figure 7 or Figure 10) and much as is seen in numerical models (see Figures 34 and 36).

We can take "PV thinking" further to consider the hydrodynamical stability of the mixed patch by making use of a "mathematical trick" that is due to *Bretherton* [1966]. In the inversion that resulted in Figure 37a, an inhomogeneous Neumann boundary condition that depends on the surface density distribution was employed at the surface. However, it is well known from "potential theory" that any such inhomogeneous boundary condition can be replaced by a homogeneous one, provided that the source function is appropriately modified. Thus in the (numerically obtained) solution shown in Figure 37b, homogeneous Neumann boundary conditions on pressure are applied in conjunction with an appropriately modified source function: a δ function sheet of positive potential vorticity anomaly is added just underneath the surface to represent the cold surface. The strength of the PV sheet, δ_-, is just that required to ensure that the vertical integral of $(Q + \delta_-)$ over each column of ocean vanishes. The Q has been "evacuated" by convection from the interior ($Q \rightarrow 0$ there) and concentrated in to a sheet of Q just beneath the surface. However, now, in Figure 37b, boundary conditions and interior sources are given an equal footing; moreover, they are the potential vorticity distributions that can be inverted subject to homogeneous boundary conditions.

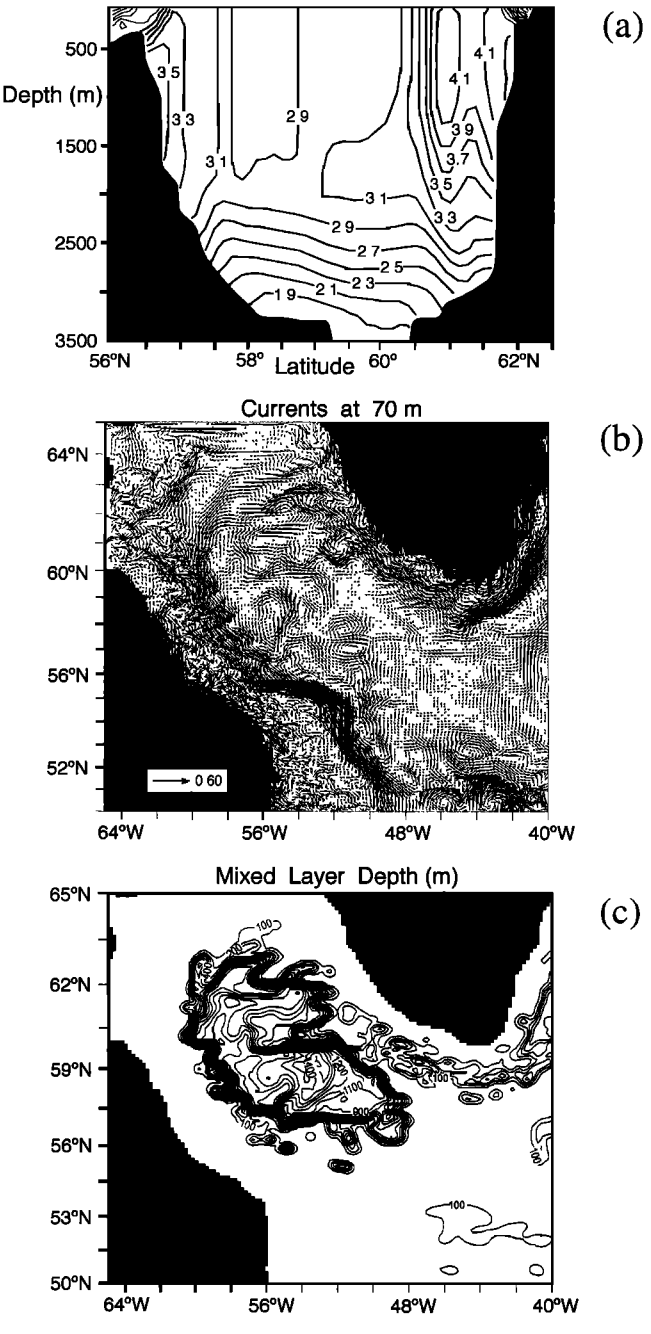

Figure 36. Simulation of water-mass transformation in a high-resolution model of the Labrador Sea: (a) hydrographic section of potential temperature across the Labrador Sea, (b) currents at depth of 100 m, and (c) mixed-layer depth during March 1992.

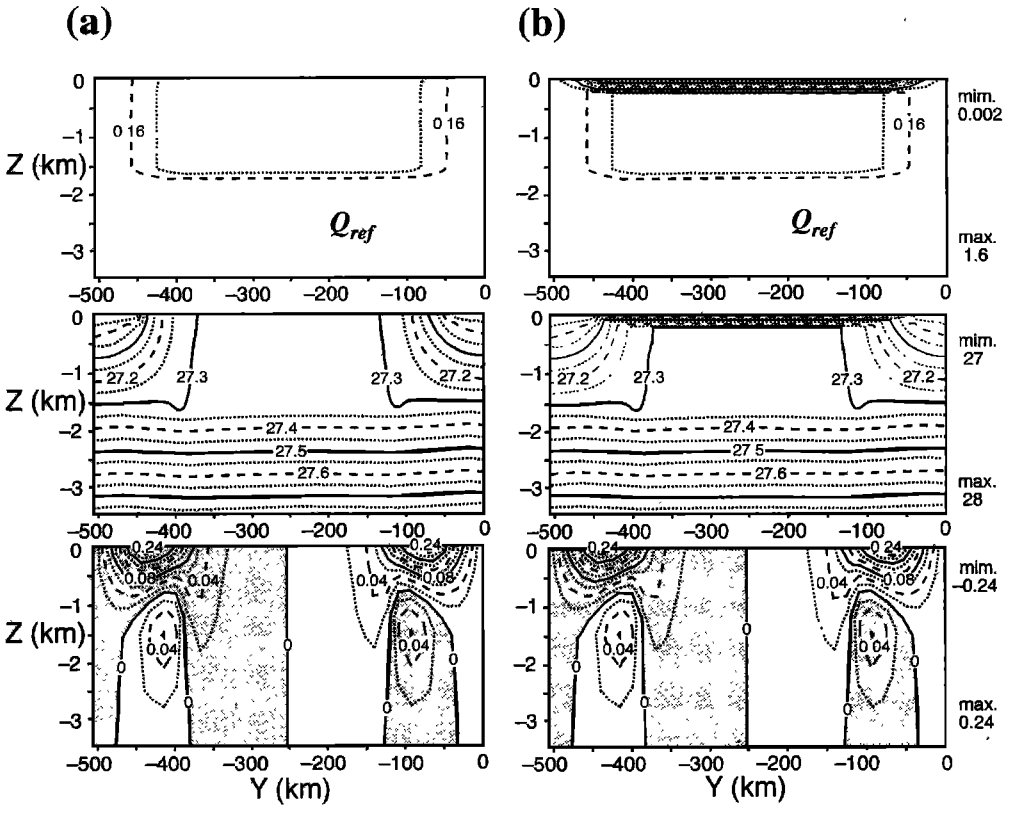

Figure 37. PV inversion for a mixed patch with (a) inhomogeneous and (b) homogenous boundary conditions at the surface. PV distribution, isopycnals, and currents are plotted. In Figure 37a the potential density at the sea surface is specified and an idealized interior PV anomaly inverted to give the hydrography and azimuthal velocity of a baroclinic vortex. In Figure 37b an interior PV field identical to that of Figure 37a is used, but now the cold surface is represented by a sheet of high PV just beneath the upper boundary, which is prescribed to be an isopycnal surface. Note that in Figure 37b, unlike Figure 37a, the isopycnals cannot cut the upper surface, which itself is an isopycnal.

For example, we can now easily see why a dense (cold/and or salty) surface induces cyclonic circulation. It is equivalent to a positive sheet of PV. The low PV of the interior of the mixed patch induces anticyclonic circulation (PV is very small there). Moreover, "Bretherton PV sheet" concepts also clearly indicate that the mixed patch will be subject to baroclinic instability and suggest highly instructive idealized models of the lateral exchange of fluid with its surroundings based on point vortices. These are now discussed in the next section.

4.3.2. Hydrodynamical instability of mixed patches. We have argued that the convective process resets and redistributes the PV of the ambient fluid, resulting in mixed patches that are highly susceptible to, and strongly modified by, baroclinic instability. The homogeneous column of water is cold and dense at the surface relative to its surroundings, and so ∇Q points inward to the δ function disc of high PV at the surface (see Figure 38). The interior of the mixed patch has very low (essentially zero) PV, and so below, ∇Q points outward from the patch. Thus the necessary conditions for baroclinic instability (reversal in sign of ∇Q somewhere within the fluid) are manifestly satisfied. Analytical study of the stability of such structures using the "method of perturbations" can readily be carried out within the confines of quasi-geostrophic theory [e.g., *Killworth*, 1976; *Pedlosky*, 1985; *Helfrich and Send*, 1988]. If the radius of the mixed patch is large in relation to the Rossby radius of deformation, then the analysis asymptotes to that of *Eady* [1949]. The growth rate of the fastest growing mode is

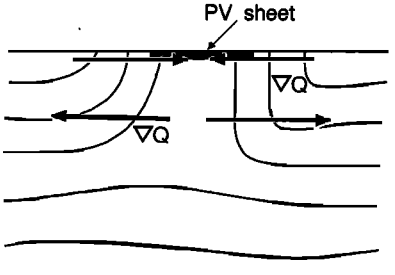

Figure 38. A schematic diagram showing the large-scale potential vorticity (Q) distribution induced by convective mixing of a patch of ocean. The patch is readily susceptible to baroclinic instability; ∇Q points inward at the surface and outward in the interior beneath.

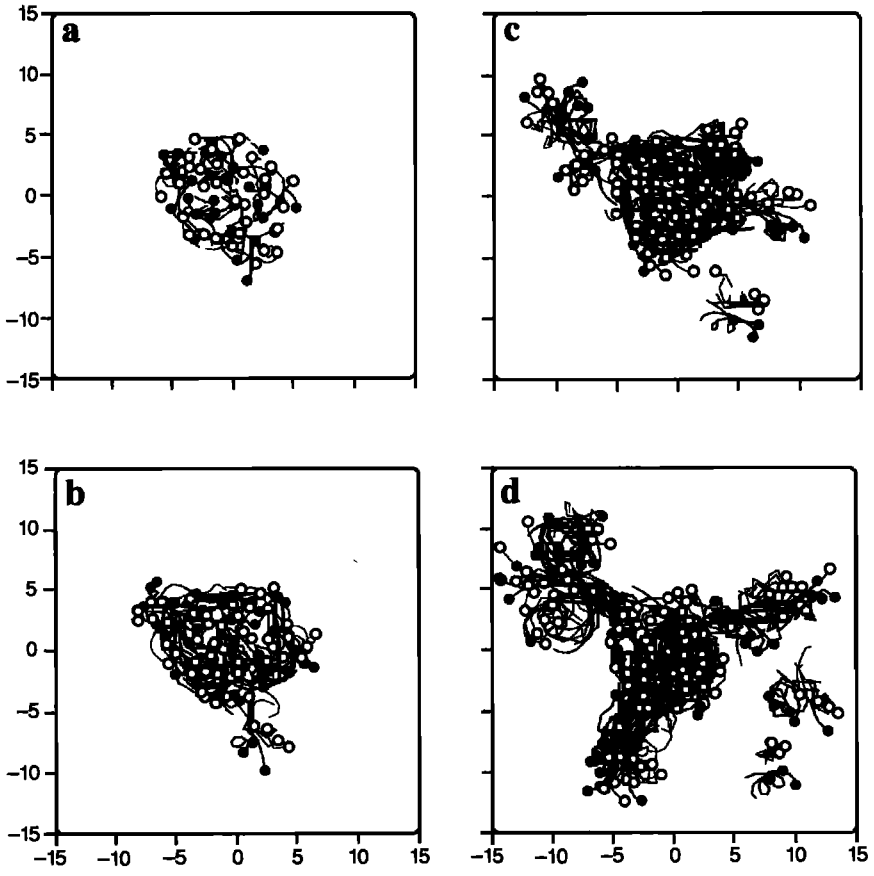

Figure 39. Four pictures charting the development of a mixed patch comprising an evolving cluster of hetons. Each picture shows the trajectories of the hetons over a period of 0.6 days: (a) 0.6–1.2 days, (b) 1.2–1.8 days, (c) 1.8–2.4 days, (d) 2.4–3.0 days. The trajectories of the upper layer vortices are marked by solid circles, while those of the lower layer vortices are shown with open circles. The horizontal scale is presented in units of the deformation radius and the hetons are introduced over a disc of diameter of 5 Rossby radii. From *Legg and Marshall* [1993].

found to be proportional to $f/Ri^{1/2}$ on a scale close to NH/f, where H is the depth of the mixed patch and Ri is the large-scale Richardson number of the ambient fluid. Because the ambient N is relatively small in deep convection sites, $N/f \sim 5$–10, typical Ri values are also small (~10), the growth rates are rapid (a few days), and the scales are small (a few kilometers).

Laboratory and numerical experiments suggest that linear theory is a useful guide in the early growth of instabilities but nonlinear processes soon take hold; eddies mature and merge as the patch disintegrates. *Legg and Marshall* [1993] exploit Bretherton sheets to model the mixed patch as a collection of paired point vortices (called "hetons" by *Hogg and Stommel* [1985]) and so are able to address nonlinearity. In numerical experiments using Green's function techniques in a two-layer model, they pepper the convection site with paired point vortices, one (of strength $q+$) in the upper layer to represent the cold surface and one (strength $q-$) in the lower layer to represent low PV. The rate of introduction of vortices can be directly related to the rate at which buoyancy is lost from the sea surface. In the experiment shown in Figure 39 a constant cooling of 800 W m^{-2} over a disk of diameter 16 km (about 10 times the Rossby radius of deformation) is assumed, consistent with the explicit calculations of *Jones and Marshall* [1993]. Cooling at this rate creates hetons of strength $0.6f$ at a rate of 33 per day. They are introduced with random initial coordinates.

During the first 2 days, most of the hetons remain within the patch of cooling (see Figures 39a and 39b). As the number of hetons within the patch increases, a sheared current develops around the rim, cyclonic above and anticyclonic below, reaching a magnitude of ~20 cm s^{-1}. This rim current effectively constrains the vortices within the disc. Initially, they are prevented from forming self-propelling pairs by this strong shear current: any pairs are torn apart before they can "escape." However, over time the rim current develops waves of mode number 4–5 (see Figures 39b and 39c) through the mechanism of baroclinic instability. After ~2 days we see tilted clusters containing several hetons that burst out of the main cloud, breaking through the sheared rim current (Figure 39c). The convection site therefore breaks up into several smaller tilted clusters, which propagate outward. The heton clusters continue to travel outward (Figure 39d), carrying cold water far from the area of cooling. These extended hetons, clumping together on the radius of deformation scale, are very efficient at fluxing heat laterally into the cooling area (as described in section 4.4.2). Linear theory is very successful in predicting the scale of the clumping. As time progresses and the hetons disperse, the magnitude of the rim current diminishes, and so it is easier for subsequent groupings to move outward. Ultimately, a steady state is reached in which the flux of hetons out of the area of cooling, in the form of tilted clusters, approximately balances the rate at which hetons are generated and so

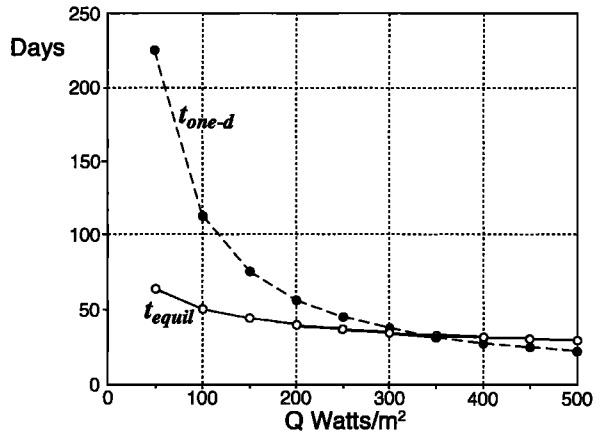

Figure 40. The curve of $t_{1\text{-D}} = (N^2/h^2/2\mathcal{B})$ (equation (10), with $\mathcal{B}$ assumed constant) and t_{equil} (equation (33)) as a function of the cooling rate if $h = 100$ m, $r = 50$ km, and $N = 10^{-2}$ s^{-1}.

the number of hetons in the area of cooling remains approximately constant.

Hetons are used by *Brickman* [1995] to model the lateral transports of heat in baroclinic instability and so reconcile the mean temperature attained over a warm disc in his laboratory models of convection heated over a patch from below. The equilibrium limit in which heat input (or output) is entirely balanced by lateral flux, the one discussed in section 4.3.3 below, is also studied using heton models by *Legg et al.* [1996] and preconditioning effects associated with barotropic flow by *Legg and Marshall* [1998]. Hetons are also useful analogues of the eddies seen in the environs of observed mixed patches.

4.3.3. Equilibrium depth and timescales. The eddies observed in the laboratory and numerical experiments reviewed above carry buoyancy laterally inward and upward to arrest the deepening of the mixed patch (see, for example, Figure 33). *Visbeck et al.* [1996] study and quantify the equilibrium properties of a mixed patch embedded in a linearly stratified ocean, if buoyancy loss through the sea surface, $\mathcal{B}_0$, were entirely balanced by lateral buoyancy flux accomplished by eddies around the periphery of the mixed patch, across the rim current $\overline{v'b'}$:

$$\int \mathcal{B}\, dA = \int_{-h_{equil}}^{0} \oint \overline{v'b'}\, dl\, dz \qquad (28)$$

Here the overbar denotes a time average that is long in comparison with a typical eddy lifetime. Of course, such an equilibrium state may not always be achieved in nature (see below), but it is an interesting limit state and one that is amenable to analysis.

Visbeck et al. [1996] solve (28) for the equilibrium depth h_{equil} using the eddy transfer theory of *Green* [1970] (developed to describe the lateral heat flux by baroclinic eddies in the atmosphere), which relates the eddy buoyancy flux to the large-scale gradient. Green supposed that the eddy velocity v' would scale like a length ℓ multiplied by a growth rate proportional to $f/Ri^{1/2}$, as given by Eady theory, and b' would scale like $M^2\ell$, yielding

$$\overline{v'b'} = \alpha \frac{f}{Ri^{1/2}} M^2\ell^2 \qquad (29)$$

where α is a constant of proportionality; $M^2 = \partial b/\partial y$ is a measure of the stratification in the horizontal, analogous to N^2; the large-scale Richardson number is:

$$Ri = \frac{N^2 f^2}{M^4} \qquad (30)$$

and ℓ is the lateral scale of the eddy transfer process. Using the eddy closure equation (29) they solve (28) for h_{equil} and deduce that

$$h_{equil} = \gamma \frac{(\mathcal{B}r)^{1/3}}{N} \qquad (31)$$

where $\gamma = 1/(2\alpha)^{1/3}$.

In an evaluation of many numerical and laboratory experiments of baroclinically unstable mixed patches, *Visbeck et al.* [1996] confirm the parameter dependence of h_{equil} on $\mathcal{B}$, r, and N suggested by (31) and find that (a fit from experimental data)

$$\gamma = 3.9 \pm 0.9$$

implying an α in (29) that has the value

$$\alpha = 0.008 \pm 0.005 \qquad (32)$$

This is remarkably close to the value obtained by *Green* [1970] in his study of heat transport by baroclinic eddies. These results will be used later, in section 5.2, where we discuss the parameterization of baroclinic eddies.

Visbeck et al. [1996] also show that the time t_{equil} to reach the depth h_{equil} is given by

$$t_{equil} = \beta(r^2/\mathcal{B})^{1/3} \qquad (33)$$

$$\beta = 12 \pm 3$$

where β has been determined empirically from laboratory and numerical data. What are the implications of these results for the dynamics of mixed patches?

In Figure 40 we plot t_{equil} (equation (33)) and $t_{1\text{-D}} = N^2h^2/2\mathcal{B}$, the time it takes for a 1-D nonpenetrative model to get to the depth h, as a function of the cooling rate for $h = 100$ m, $N = 10^{-2}$ s^{-1} (typical of the strongly stratified surface waters; see Figure 2), and $r = 50$ km. We see that for persistent cooling rates in excess of 350 W m^{-2}, the mixed layer will reach a depth of 100 m in less than 30 days, before it is arrested by baroclinic instability. If the cooling rates are smaller than this critical value, however, the deepening will be arrested by baroclinic instability. Choosing somewhat different, but not untypical values (see Figure 2, section 1) $N_{surface} \approx 5 \times 10^{-3}$ s^{-1}, $\mathcal{B}_0 = 7.5 \times 10^{-8}$ m^2 s^{-3}

(corresponding to a heat flux of 150 W m^{-2}), h = 200 m, we find that $t_{1\text{-}D}$ = 60 days. This is long in comparison with typical baroclinic instability timescales, and so for lower cooling rates, perhaps more typical of the climatology, baroclinic instability may indeed control the ultimate depth to which the mixed layer reaches. But if buoyancy is extracted rapidly, in one or two violent events, baroclinic instability will not have sufficient time to limit the depth: 1-D ideas ought to be adequate to determine the depth to which the rapid deepening reaches. The patch of homogeneous fluid will nevertheless subsequently break up by baroclinic instability, and the eddies will disperse and play a role in restratifying the convection site (see section 4.4).

In the winters of 1969 [*MEDOC Group*, 1970] and 1992 [*Schott et al.*, 1994] convection did not reach the bottom but stopped at intermediate levels. Perhaps the deepening of the mixed patch was arrested by lateral, eddy-induced buoyancy flux, which offset the surface cooling. For a Mediterranean mixed patch with width of ~60 km and a typical mistral heat loss (600 W m^{-2}) equation (33) gives $t_{equil} \approx$ 30 days. Therefore it seems unlikely that baroclinic eddies played a central role in arresting the deepening chimney because the period of strong heat loss lasted only 10 days. However, close to the rim current, significant lateral heat and tracer fluxes must have occurred associated with geostrophic eddies.

Baroclinic eddy fluxes are likely to be of great importance, however, on the seasonal (preconditioning) timescale because the geostrophic eddy instability time is then considerably shorter than that of the forcing. If the heat loss is ~200 W m^{-2} and the diameter of the convecting region is ~200 km, parameters perhaps more typical of the Labrador Sea gyre, then (33) yields a breakup timescale of ~60 days. This suggests that by the end of winter baroclinic eddies can influence the mixed-layer budget significantly even at the center of the gyre.

4.4. Restratification and Geostrophic Eddy Effects

4.4.1. Observations. We now briefly review the fragmentary observations of lateral exchange processes between the convection site and its environs.

4.4.1.1. Eddy exchange: While plume development and the creation of mixed patches have been reasonably well observed, the observations that pertain to the integral effects of convection on the large-scale environment are still sparse. The development of geostrophic eddies, their associated timescales, and their exchange with the environmental water masses has not been well documented. *Gascard* [1978] first investigated the role of eddies at the margin of the deep mixed regime and their generation by baroclinic instability, as did *Gascard and Clarke* [1983] for the Labrador Sea convection regime. The scale of the cyclonic eddies traced in these cases corresponded to the local Rossby radius. However, the role of geostrophic eddies in the lateral exchanges between the convective patch and the stratified environment has not yet been quantified by direct observations.

One way of determining the associated exchange rates would be through use of moored stations with temperature-salinity recorders and current meters, from which covariances could be determined. Moored stations were maintained in the Greenland Sea and the Mediterranean during and after convective episodes, but the occurrence of eddies following individual convection events has been observed only infrequently. The eddies appeared to be few in number, and the moored stations did not always happen to be in an optimum position to make such covariances meaningful [e.g., *Schott et al.*, 1996]. Ensemble statistics could perhaps be derived from Lagrangian floats, but until the Labrador Sea Experiment [*LabSea Group*, 1998], coverage of active convection regimes has not been sufficient for statistically meaningful results to be obtained. Moreover, in the northwestern Mediterranean, and probably elsewhere, there exists intense geostrophic eddy activity that is independent of the convective process, possibly associated with topographic waves along the boundary [e.g., *Millot*, 1991], adding further to the difficulty of identifying the eddy flux contribution associated with convection.

An effective way to monitor the 3-D development of water mass transformation in a convection regime and thus indirectly quantify the lateral eddy exchange is through acoustic tomography from sound sources that are distributed within and around the regime. In the 1992 experiment in the Gulf of Lions, good comparisons with hydrographic data were obtained [*THETIS Group*, 1994; *Send et al.*, 1995] that demonstrated the usefulness of the tomographic inversions as a means of measuring the integral development of the mixed patch. However, for the 1988–1989 experiment in the Greenland Sea, discrepancies exist between, on the one hand, the conclusions from the few collected hydrographic profiles and sparsely distributed moored stations and, on the other, the tomographic inversions. The former led to the conclusion that an extended deep mixed patch did not exist during that winter with only a few convective plumes occurring within the mostly stratified environment [*Schott et al.*, 1993]. Tomographic inversions, however, suggested that a mixed patch scale of O(50 km) was present [see *Worcester et al.*, 1993; *Morawitz et al.*, 1996].

The development of the convection regime during early 1992 in the Gulf of Lions, following a period of intense convection during February 18–23, is shown in Figure 41. Surrounding the deep mixed patch there is a zone where the homogeneous properties of the patch are covered by upper layer stratification. This is the region characterized by marked geostrophic eddy exchange. Here vertical profiles revealed homogeneity beneath the stratified top, and freon concentrations were found to correspond to those in the deep mixed patch, identifying the water as recently ventilated [*Rhein*, 1995]. *Send et al.* [1995] measured the development of restrati-

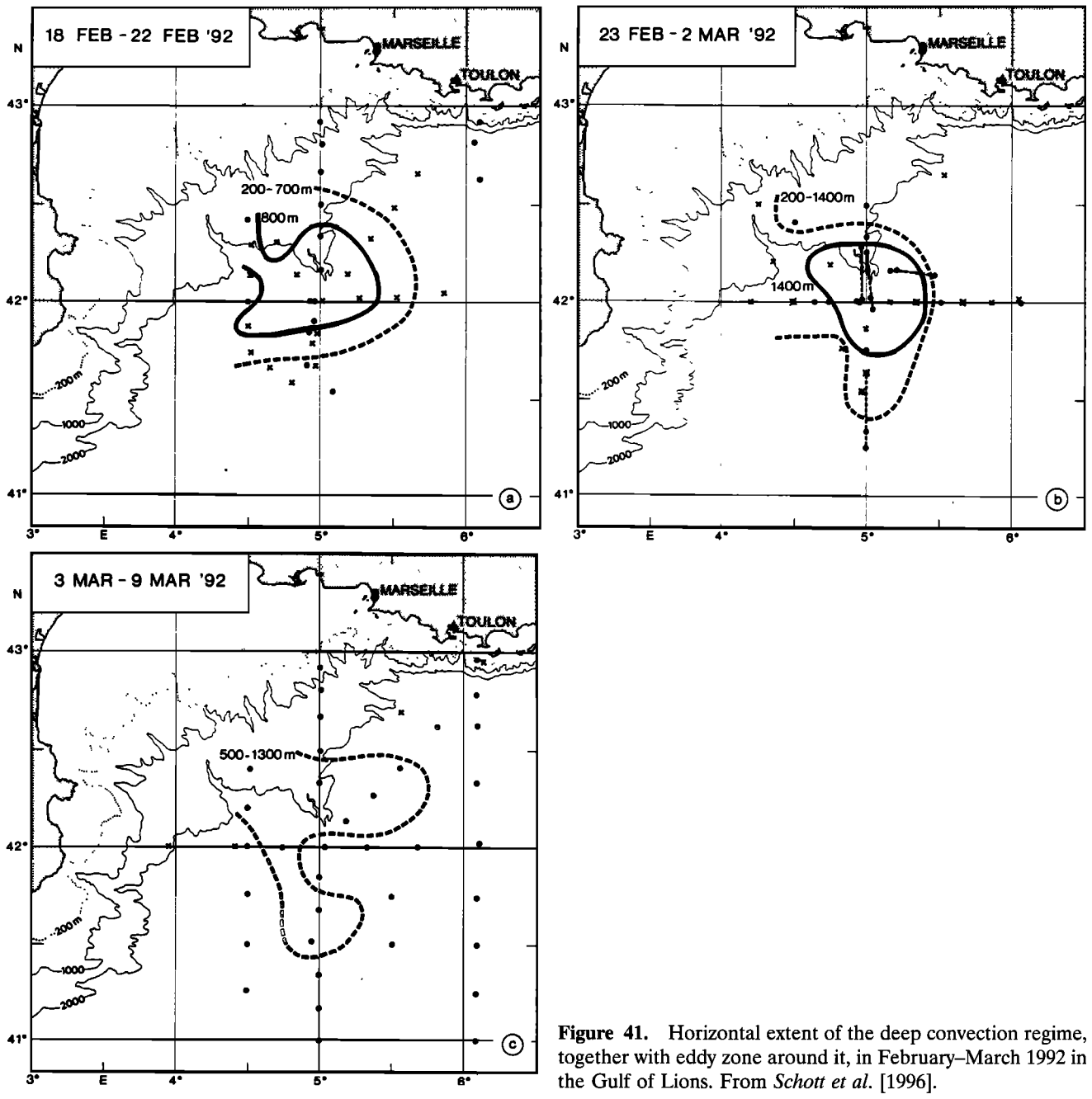

Figure 41. Horizontal extent of the deep convection regime, together with eddy zone around it, in February–March 1992 in the Gulf of Lions. From *Schott et al.* [1996].

fication in the Gulf of Lions by monitoring the presence of the LIW temperature maximum at 150- to 500-m depth using acoustic tomography. They deduced that the deep mixed patch was reoccupied by LIW in about 40 days, not inconsistent with the theory presented by *Jones and Marshall* [1997] (see section 4.4.2). Of course, these integral measurements did not allow the distinction between the effects of horizontal advection and eddy exchange.

4.4.1.2. Surface capping: One result of the experimental work was the finding of "surface capping" [*Leaman and Schott*, 1991; *Send et al.*, 1995]. From hydrographic casts and tomography inversions it was discovered that after cessation of intense cooling, a thin stratified near-surface layer developed on top of the mixed patch (see Figure 42). In 1992 the warm, near-surface water appeared to migrate in from the side, although attempts to measure the near-surface flows by upward looking ADCPs were unsuccessful [*Schott et al.*, 1996]. Because acoustic rays are surface trapped in stratification typical of winter, tomography has its best vertical resolution near the surface and so can readily be used to measure surface capping. The inversion for the average temperature of the upper 150 m by *Send et al.* [1995] showed that to the south of the mixed patch, capping occurred within a few days, while to the north, where the patch abuts the shelf edge, the surface layer restratified within ~1 week.

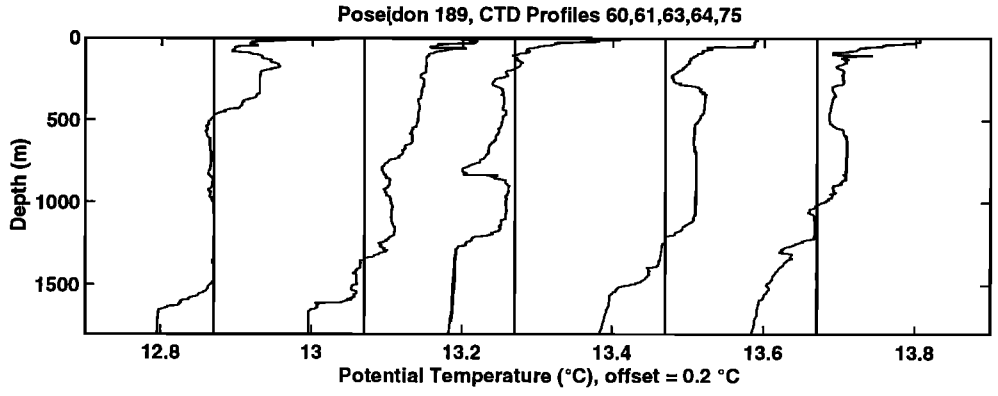

Figure 42. CTD profiles showing "capping" during the restratification phase of convection in the Mediterranean.

We now go on to describe likely physical mechanisms that might be responsible for the rapid restratification.

4.4.2. Restratification and dispersal mechanisms. There are a number of possible restratification and dispersal mechanisms. A mixed body of fluid that abuts a boundary will excite topographic waves that are forerunners of the "bleeding" of the convected fluid away from the reservoir in boundary current. Indeed, the observations presented by *Send et al.* [1996] hint at a boundary "event," the passage of (cold) fluid that, it is surmised, was convectively modified a few weeks before by the mistral. Boundary signals have also been studied in numerical simulations (for example, *Madec et al.* [1991] show such a signal of convected fluid in the boundary current north of the convection site in the Gulf of Lions). While Kelvin waves are possible, indeed inevitable, and do carry away some of the convected fluid, their transport seems quite limited. *Hallberg and Rhines* [1996] emphasize the role of topographic Rossby waves in which the attendant vorticity pattern is transmitted by topographic wave dynamics with considerable recirculation and counterflows adjacent to the main current. By contrast, with a vertical sidewall the "Kelvin wave plume" has a simpler structure. *Hermann et al.* [1989] use contour dynamics and explicit simulation to show how the Kelvin plume develops through nonlinear vorticity dynamics.

Wind-driven Ekman layer processes are likely to play a role in the advective supply of stratified fluid to the convection site. However, it is not yet clear whether ageostrophic advection is of the appropriate sign or magnitude to account for the very efficient restratification process that is observed to occur over a rather deep surface layer.

Jones and Marshall [1997] attempt to quantify the role of geostrophic eddies in the breakup and dispersal of mixed patches. We have seen that if the radius of the mixed patch is greater than the Rossby radius of deformation $L_\rho = Nh/f$, then it is prone to baroclinic instability. Figure 43 presents results from a numerical calculation in which a cylinder of dense homogeneous fluid was placed in an initially resting stratified fluid and allowed to freely evolve in the absence of external forcing. They were inspired by the early "cylinder collapse" experiments of *Saunders* [1973] (see also *Herman and Owens* [1993]). The radius of the cylinder is 50 km, greatly exceeding the deformation radius L_ρ (here 4 km). Initially, the edges of the column merely slump as the dense fluid sinks and spreads under the influence of gravity. The spreading is limited (initially) to a deformation radius by rotation as azimuthal (rim) currents, cyclonic on top and anticyclonic below, are set up in thermal wind balance with the lateral density gradients at the edge of the column. Subsequently, however, baroclinic eddies grow (here a mode 14 instability), reach finite amplitude by day 20, and lead, over a period of a further week or so, to the breakup of the mixed patch. The dense fluid that defined the cylinder at $t = 0$ has, by $t = 50$ days, broken up and been dispersed by geostrophic eddies over the whole of the (doubly periodic) domain at its neutrally buoyant level.

Jones and Marshall [1997] conclude that lateral eddy-transport of fluid from the buoyant boundary current that typically surround convection sites is a likely restratification mechanism. Moreover, by quantifying the efficiency of the lateral eddy transport process, in a manner that parallels the development in section 4.3.3, they are able to deduce and support by numerical experiment, the following restratification timescale. If the mixed layer has a depth h and lateral scale r and is characterized by a density jump at its edge of magnitude Δb, then they find

$$\tau_{\text{restrat}} \approx 56 \frac{r}{(h\Delta b)^{1/2}} \tag{34}$$

Choosing $h = 500$ m; $\Delta b = 2 \times 10^{-3}$ m s^{-2}, and $r = 200$ km, broadly consistent with Labrador Sea conditions, for example, then we find that $\tau_{\text{restrat}} \approx 100$ days, a plausible timescale and not inconsistent with the fragmentary observational evidence that is currently available in the Labrador Sea. Parameters more typical of the

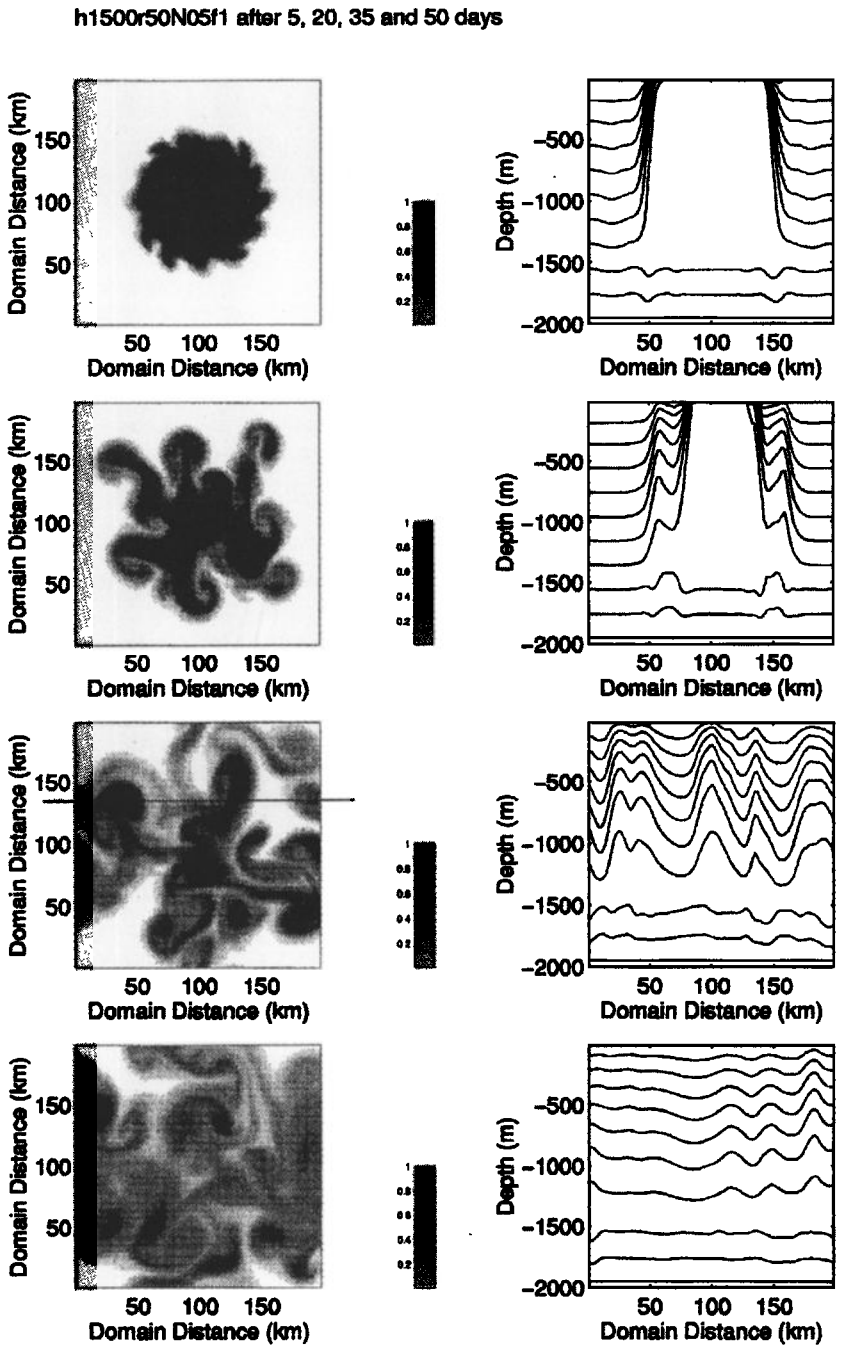

Figure 43. Numerical illustration of the baroclinic instability of a cylinder of dense fluid, of depth 1500 m and radius 50 km in an ambient fluid in which $N/f = 5$. The "plan view" panels on the left chart the development of a passive tracer at the base of the cylinder at a depth of 1400 m at (from top to bottom) 5, 10, 35, and 50 days. On the right we show a "hydrographic section" of density through the center of the patch. (See *Jones and Marshall* [1997].)

Mediterranean ($h = 100$ m; $\Delta b = 2 \times 10^{-3}$ m s^{-2}, and $r = 100$ km) give $\tau_{restrat} \approx 20$ days, again not untypical of what is observed.

The unraveling of the relative importance of these competing processes during each stage of the convective process demands further observations in the light of theoretical and numerical study.

5. PARAMETERIZATION OF WATER MASS TRANSFORMATION IN MODELS

Ocean models used to study the general circulation and, when coupled with atmospheric models, in climate research, typically have horizontal resolutions of several hundreds of kilometers. Then both the convective scale and baroclinic eddy scale are "subgrid scale." Both processes and their interaction must be parameterized. However, water mass transformation in ocean models is, more often than not, discussed solely in terms of the vertical axis and "recipes" of vertical mixing and adjustment. However, we have seen that the process involves lateral exchange between the convection site and its environment by baroclinic instability as well as vertical mixing in localized regions by convection. On the basis of the observations, theory and models described in the previous chapters, and the discussion below, we believe that the ability of low-resolution ocean models to ade-

quately represent water mass transformation is compromised primarily by the rudimentary nature in which lateral rather than vertical processes are parameterized in models.

One way forward is to increase the horizontal resolution of such models down to 5 km or so enabling the small baroclinic scales typical of convection sites to be resolved. Then only the convective scale need be parameterized. Even if rather simple "mixing" or (equivalently) "adjustment" schemes were employed to represent the convective scale in such high-resolution models (as in Figure 36, for example), the water mass transformation process would be much improved over that of coarse-resolution models. With presently available computers, however, this direct approach is possible only in regional models. In ocean climate models the geostrophic scale and its interaction with convection must also be parameterized, and therein lies the intellectual challenge. The parameterization of the convective scale is discussed in section 5.1, followed by in section 5.2, discussion of the concomitant geostrophic scales.

5.1. One-Dimensional Representation of Plumes

5.1.1. Convective adjustment and vertical mixing. The observations suggest, and it has been argued on physical grounds, that convective plumes efficiently mix properties such as temperature, salinity, and density (see sections 3.1.1 and 4.2) rather than acting as an agency of vertical mass exchange. "Convective adjustment" algorithms are often used to remove static instabilities (heavy fluid over light) in general circulation models. While there are several numerical renditions, all adjustment algorithms share the same principle: the potential density of fluid at one model level is compared with the level below, and if it is found to be denser, a vertical mixing of parcels occurs. The first implementations [*Bryan*, 1969; *Cox*, 1984] compared adjacent levels only, in an iterative process, but more recent ones [*Marotzke*, 1991; *Yin and Sarachik*, 1994] mix the whole unstable part of the water column to give a vertically homogeneous state. However, the column is adjusted instantaneously. Enhanced vertical diffusion, with a somewhat arbitrarily chosen value of vertical diffusivity, is also commonly used to parameterize convection [see *Cox*, 1984; *Marotzke*, 1991]. As was shown by *Klinger et al.* [1996, appendix], vertical diffusion is formally the same as "adjustment" with a finite, rather than an instantaneous, adjustment timescale.

The following questions come to mind in regard to the efficacy of adjustment and vertical diffusion schemes to represent plume-scale mixing. If an adjustment scheme is employed, is it reasonable to suppose that adjustment occurs instantaneously? If the mixing process is represented by an enhanced vertical diffusion, how large should the diffusivities be?

Send and Marshall [1995] characterize convective mixing by a timescale, t_{mix}, that determines how long it takes before water properties at the bottom of a mixed layer are significantly changed by buoyancy forcing at the top. This timescale is related to the transit time of a particle as it descends, in a convective plume, from the sea surface to the bottom of the mixed layer. For convective plumes characterized by vertical speed w_{plume}, it takes a time of the order of

$$t_{mix} \approx h/w_{plume} \tag{35}$$

to bring dense surface fluid to the bottom. For vertical velocities typical of deep convection (see Table 4), t_{mix} can be 12 hours or longer, perhaps long enough that setting t_{mix} to zero compromises the scheme.

Klinger et al. [1996] discuss simple parameterizations of convection that attempt to represent this finite t_{mix}. For example, one could employ an appropriately chosen vertical diffusivity of temperature and salinity in statically unstable regions. It would seem desirable to deduce the magnitude of the diffusivity from physical knowledge of t_{mix}. Because a diffusive system takes a time of the order of h^2/k to send a signal a distance h, the diffusivity ought to be [see *Send and Marshall*, 1995]

$$k_v \approx h^2/t_{mix} = hw_{plume} \tag{36}$$

If we assume $w_{plume} = 0.05$ m s^{-1} and $h = 1000$ m, then $k_v \approx 50$ m^2 s^{-1}, significantly larger than, for example, the value of 1 m^2 s^{-1} used by *Marotzke* [1991].

The appropriate scaling for w_{plume} and hence t_{mix} are discussed by *Klinger et al.* [1996], who compared parameterized numerical simulations of mixed patches deepening in to stratified fluid (of the type shown in Figures 31 and 33) with explicit simulations in which the convective plumes themselves are resolved. Results are not sensitive to t_{mix}, provided that it is sufficiently short, suggesting that although simple, convective adjustment has many merits.

Before we go on, it is worth noting the common misconception that convective adjustment (or enhanced vertical diffusion) must be used in hydrostatic ocean models to represent convection because such models, of themselves, cannot overturn. It is the coarseness of the horizontal resolution, rather then the limitation of the dynamical description, that suppresses the convective instability. In fact, the hydrostatic models exhibit more vigorous static instability than nonhydrostatic models when convective scale is resolved [see *Marshall et al.*, 1997a].

5.1.2. Mixed-layer schemes. More often than not deep convection is represented in ocean models in the framework of "mixed-layer models," which are used to represent the surface mixed layer in the ocean, without special treatment of deep mixed layers. There are a large number of mixed layer models that have been comprehensively reviewed by *Nurser* [1998]. Here we only very briefly outline the nature of some of them and their relevance to the deep convection regime.

The first mixed-layer model (due to *Kraus and Turner* [1967]) is a "slab" model and assumes that the mixed layer is fully mixed. It includes, as part of its representation, a convective adjustment scheme of the kind described in section 5.1.1 above. However, the entrainment rate at the base of the layer and the rate of warming of the layer are related to the change of column-integrated potential energy and thence to sources and sinks of turbulent kinetic energy (TKE) and radiative and surface buoyancy fluxes. This model was assumed in the mixed layer calculations presented in Figures 17 and 18 and does remarkably well in the deepening phase of the mixed layer because the assumption that the mixed layer can be treated as a slab when it is cooling is a good one. In the original model of *Kraus and Turner* [1967] the only source of TKE was wind stirring, but *Niiler* [1975] and *Niiler and Kraus* [1977] extended this class of model to include a source that was due to shear instability at the base of the mixed layer.

The family of "Richardson number models" (see, for example, *Pollard et al.* [1973] or *Price et al.* [1986]) are conceptually similar to adjustment schemes but mix only when the Richardson number within the layer falls below a critical value, although when they mix, they mix perfectly. Instead, in the "K profile" model of *Large et al.* [1994] (perhaps the model with greatest fidelity), turbulence partially mixes properties in the vertical rather than mixing them perfectly as in a "slab" mixed layer. However, all of the aforementioned schemes have been developed for shallow mixed layers and not regions of deep convection, where convective plumes may be more intermittent, where the Earth's rotation may be important, and where there is significant localization of the deep mixing region. For this reason, "plume models" have been developed that attempt to address the "plumey" nature of the mixing process in deep convection.

5.1.3. Plume models. Plume-based schemes have recently been developed to parameterize deep ocean convection. Also known as mass-flux schemes, they have a long history of use in the atmosphere, beginning with *Arakawa and Schubert* [1974]. Convection within the grid cell is modeled as an ensemble of convecting plumes. The fraction of fluid contained within the plume is transported from one level to the next, with entrainment of ambient fluid. If the pressure is assumed to be in hydrostatic balance with the mean temperature, the evolution of the plume quantities with height can be predicted using conservation of mass, heat, and momentum following a parcel, modified by entrainment and buoyancy acceleration. Ultimately, the parcel reaches a height at which it is no longer buoyant in relation to the surroundings, and detrainment is assumed to occur. The net effect of the plume-based scheme is a redistribution of density and tracers, which is based on the dynamics of an entraining plume. If a tracer is injected into a plume near the boundary, it will not be mixed into the ambient fluid until detrainment occurs. Hence a significantly nonlocal transport can result, with a property transported directly from the surface to the interior.

While plume schemes attempt to mimic the actual convective elements, many assumptions are made that are difficult to motivate from observations or theory. For example, the *Arakawa and Schubert* [1974] scheme assumes a quasi-equilibrium between convection and large-scale convergence to determine the convective mass fluxes. Another commonly used closure minimizes the available buoyant energy [e.g., *Fritsch and Chappell*, 1980]. Mesoscale atmospheric models more commonly assume local closures, for example, an empirical relationship between the convective instability of the lowest model level and the initial plume mass flux [*Gregory and Rowntree*, 1990].

Two plume-based schemes have recently been adapted for use in ocean models. The first, due to *Paluszkiewisz and Romea* [1997] is based on the scheme of *Fritsch and Chappell* [1980] with modifications for the ocean. The second, due to *Alves* [1995], modifies the atmospheric scheme of *Gregory and Rowntree* [1990]. Both of these schemes appear to generate plausible profiles of density in response to surface buoyancy loss but need to be tested further against observations or explicit numerical simulations to demonstrate that significant added fidelity results from the considerable increase in complexity. Nevertheless, these models attempt to build up a scheme that is rooted in assumptions about the dynamics or kinematics of the plume scale.

5.1.4. Grid-scale instability of vertical mixing schemes. *Cessi* [1996] shows that instantaneous convective adjustment schemes applied at a horizontal matrix of points lead to the spontaneous emergence of the smallest resolved horizontal scale. Because convective adjustment vertically mixes properties at each grid point, irrespective of the horizontal distribution of such properties, horizontal spatial gradients are amplified as long as adjustment is faster than the horizontal diffusion (or advection) time between neighboring grid points. This is a very stringent condition. For example, if the horizontal currents associated with the large-scale flow are 30 cm s^{-1} and the timescale for the adjustment assumed to be 12 hours, then the horizontal grid must be finer than 15 km if the amplification is not to occur.

5.2. Geostrophic Eddies and the Spreading Phase

How does one parameterize the geostrophic eddy scale that, as we have seen, plays a central role in the transformation of water masses? One way forward, conceptually at least, is to view the spreading phase of water-mass transformation as one of redistribution of potential vorticity on isopycnal surfaces. The PV of water particles, set to very low values in convection, is subsequently advected away, conserving PV, at least on synoptic timescales. In many ways the "hetonic" description of *Legg and Marshall* [1993] is much more than a representational tool: it gets to the heart of the spreading mechanism. Convection modifies the preexisting PV

distribution, creating one that is prone to baroclinic instability (see Figures 37 and 38). The mixed patch breaks up into fragments, and the fragments, clusters of paired point vortices in the heton model, disperse, carrying away the convectively modified water tagged with its anomalously low PV that then influences its surroundings through the "invertibility principle." Indeed, PV has been used to vividly map the dispersal of convective fluid away from its source region [see *Talley and McCartney*, 1982]. Although simple to describe, the representation of this process in ocean models (in which primitive variables, rather than potential vorticity, are the prognostic variables) is not straightforward. One must attempt to represent the spreading process as an adiabatic, advective one, in which the properties of fluid particles are conserved. If one likens the spreading of convected water by geostrophic eddies to an "eddy-diffusive" process, in which properties are diffused away in to the background, one might adopt a "Fickian diffusion" description

$$D\tau/Dt = K\nabla^2\tau \tag{37}$$

where K is an "eddy diffusion coefficient" for the tracer quantity τ.

However, unless very special forms are chosen for the K, equation (37) is not faithful to important conservation properties because it likens the redistribution process to a diffusive, rather than an advective one. For example, in the limit that small-scale mixing is vanishingly small, the quantity of tracer between two isopycnal surfaces ought to be conserved.

Instead, it makes more physical sense to frame the dispersal process as an advective, rather than a diffusive one, by associating an "eddy-induced" velocity to it. The appropriate theoretical framework is provided by the transformed Eulerian mean (TEM), first introduced in the study of tracer transport in the stratosphere [e.g., *Andrews et al.*, 1987] and used to great effect by *Gent and McWilliams* [1990] in large-scale models of ocean circulation.

Representing the eddy transfer process in the tracer equation using TEM, we obtain [see *Andrews et al.*, 1987]

$$\frac{\partial\tau}{\partial t} + \mathbf{V}\cdot\nabla\tau + W\frac{\partial\tau}{\partial z} = ISO \tag{38}$$

where

$$\mathbf{V} = \mathbf{v}_h + \mathbf{v}^*$$

$$W = w + w^*$$

are the advecting velocities comprising $(\mathbf{v}_h, w)$, the Eulerian velocities of the non-eddy-resolving large-scale model, together with $(\mathbf{v}^*, w^*)$, the eddy-induced velocities. Note that in (38) and following *Gent and McWilliams* [1990], an along-isopycnal stirring term ISO is employed on the rhs to represent the isopycnal stirring of tracer.

If the eddy-induced velocities $(\mathbf{v}^*, w^*)$ are constructed so as to satisfy a nondivergent condition

$$\nabla\cdot\mathbf{v}^* + \frac{\partial w^*}{\partial z} = 0 \tag{39}$$

then the large-scale flow can evolve in a manner that, unlike (37), conserves the quantity of tracer between isentropic sheets.

As is shown by the formalism of the TEM, the $(\mathbf{v}^*, w^*)$ are given by

$$\mathbf{v}^* = \frac{\partial\mathbf{M}}{\partial z}; \qquad w^* = -\nabla_h\cdot\mathbf{M} \tag{40a}$$

where

$$\mathbf{M} = \frac{1}{N^2}(\overline{u'b'}, \overline{v'b'}, 0) \tag{40b}$$

is a vector stream function that depends on the eddy buoyancy flux $(\overline{u'b'}, \overline{v'b'})$. It should be noted that (40) and TEM theory assume, and are only formally valid in, the zonal average and the quasi-geostrophic limit, a point that should be borne in mind when applying it in the context of the convective process in the ocean.

If, following *Gent and McWilliams* [1990], it is assumed that

$$\overline{v'b'} = -K\nabla\bar{b} \tag{41}$$

where K is an eddy transfer coefficient whose variation has to be prescribed (see section 5.2.2), then (40) implies that

$$\mathbf{M} = -K\frac{\nabla_h b}{N^2} \tag{42}$$

If K is set to zero on all boundaries, then $\mathbf{M}$ is zero there, ensuring that the component of $\mathbf{v}^*$ normal to the boundary vanishes. The imposition of $K = 0$ at the surface is intimately related to, and can be rationalized in terms of, the use of an isothermal upper boundary in association with [*Bretherton*, 1966] PV sheets at the surface of the model; see section 4.3.1.

We now go on to consider the dispersal of a mixed patch of ocean in terms of the pattern of eddy-induced velocity.

5.2.1. Eddy-induced velocity in a mixed patch. Let us return to the statistically steady mixed patch overlying an adiabatic thermocline in which surface buoyancy loss over the patch is compensated by a lateral influx of buoyancy by transient geostrophic eddies (as discussed in section 4.3.3). The cylindrically symmetrical patch is sketched in Figure 44, taken from *Marshall* [1997]. There is no mechanical forcing due to the wind. Buoyancy loss results in a deep mixed layer within the patch, and upward doming of isopycnals towards its center. The Eulerian mean circulation is identically zero because the net vertical and radial Eulerian motion in the patch is vanishingly small as a result of vorticity

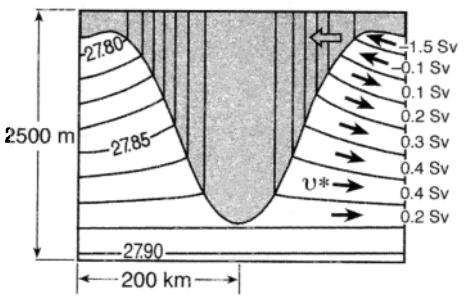

Figure 44. The solution obtained by *Marshall* [1997] for the eddy-induced velocity associated with the instability of a mixed patch. The eddy-induced circulation carries fluid from below up to the surface, where it is exposed and changed by convection. The convectively modified water slides down into the interior, out, and away. The buoyancy carried laterally by the eddy-induced circulation is just that required to offset buoyancy loss from the surface. The contour interval for the isopycnals is 0.0125 kg m^{-3}.

constraints that preclude any significant stretching of vortex tubes (see *Send and Marshall* [1995] and section 3.4.2). All of the circulation is eddy induced. The convectively modified water is carried away below by eddies and replaced with ambient fluid from the side by eddies. The pattern of eddy-induced velocity can be deduced using (40) and (42), noting that $K \equiv 0$ at the surface. The eddy buoyancy flux is directed radially inward and is a maximum at the radius of the rim current. The **v*** computed by *Marshall* [1997] making use of (40)–(42) is sketched in Figure 44. The eddy-induced circulation carries fluid up from below to the surface, where it is exposed and its properties are changed by convection. The convectively modified water slides down into the interior, out, and away.

After the buoyancy loss has ceased, the eddy transfer process continues until the conditions for baroclinic instability are no longer satisfied. It is clear from the sense of the eddy-induced velocity sketched in Figure 44 that buoyant, ambient fluid will be drawn in from the periphery sealing over the mixed-patch, and the convected fluid will be drawn away in to the interior below—just as it is sketched schematically in Figure 3c. The sealing over of the surface anomaly on cessation of the surface cooling removes the conditions for instability (i.e., removes the surface PV anomaly sketched in Figure 38) and "quenches" it.

Figure 45 shows the distribution of convection as modeled in the world ocean using the Geophysical Fluid Dynamics Laboratory (GFDL) ocean model by *Danabasoglu and McWilliams* [1995] and two different eddy parameterizations but the same vertical mixing scheme. When horizontal diffusion is used to represent eddy transfer one observes (see Figure 45a) extensive regions of convection, particularly in the Southern Ocean, and much more extensive than is observed to occur in nature. When a transformed Eulerian mean is used, however, the convection sites contract dramatically in horizontal extent and have a more realistic distribution. The mixed layers are kept shallow in the Antarctic Circumpolar Current by the "eddy-induced velocity" that is directed southward across the current, carrying buoyant fluid and stabilizing the column. The same eddy-induced circulation in part cancels out the Deacon Cell, reducing the strength of the (transformed) circulation.

The TEM clearly provides a fruitful framework for discussing "adiabatic" aspects of the spreading phase of deep convection. There are a number of outstanding theoretical questions, however. The TEM has yet to be placed on a firm theoretical basis in three dimensions even in quasi-geostrophic theory. Moreover, the quasi-geostrophic assumption clearly breaks down in mixed patches, where even the hydrostatic approximation must be questioned. Furthermore, geostrophic eddies are also important diabatic transferring agents in the mixed patches and not just responsible for adiabatic rearrangements. The interaction of an adiabatic interior with a mixed layer has been touched on in the recent study by *Treguier et al.* [1997].

5.2.2. How strong are the eddy-induced velocities? What sets the strength of the eddy-induced velocity shown in Figure 44? In section 4.3.3 we discussed the depth a mixed patch reaches before the deepening is arrested by eddies. At this depth, lateral transfer of buoyancy by eddies exactly balances loss from the surface. The depth reached leads directly to information

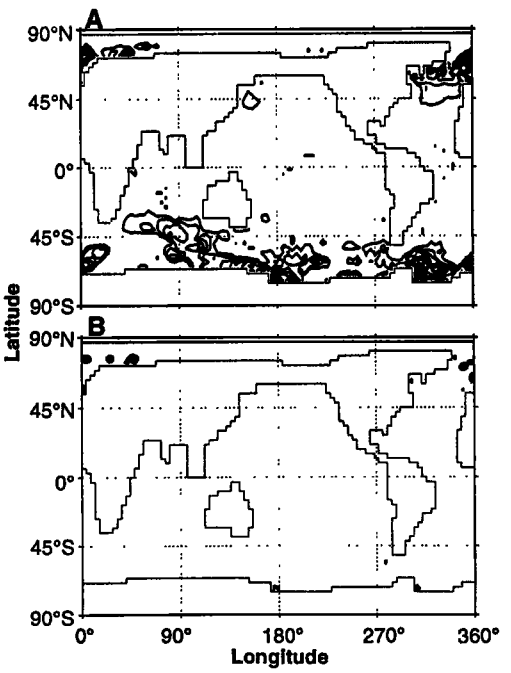

Figure 45. The % of all times and level when convection occurs when geostrophic eddy transfer is represented in the GFDL model using (a) horizontal diffusion and (b) a transformed Eulerian mean. From *Danabasoglu and McWilliams* [1995].

about the efficiency of eddy transfer (essentially the strength of the eddy-induced circulation in Figure 44) and its dependence on large-scale stratification parameters. In particular, the closure for the buoyancy flux, equation (29), led *Visbeck et al.* [1996] to a prediction of the dependence of the equilibrium depth h_{equil} on the external parameters, $\mathcal{B}$, r, and N, and a quantification of the constant of proportionality, α, a measure of the efficiency of buoyancy transfer by baroclinic eddies (see equation (32)). These predictions have now found support in numerous laboratory and numerical experiments reported by *Visbeck et al.* [1996], *Whitehead et al.* [1996], *Haine and Marshall* [1998], *Jones and Marshall* [1997], *Narimousa* [1997], *Chapman and Gawarkiewicz* [1997], and *Chapman* [1998]. The latter two papers apply these ideas to coastal regions.

Turning the argument around, one may interpret the above studies as providing solid "experimental" support for an eddy-transfer closure of the form of (29). The eddy fluxes in (41) may be characterized by a transfer coefficient K, which depends on large-scale parameters thus:

$$K = \alpha \frac{f}{Ri^{1/2}} l^2 \qquad (43)$$

where f is the Coriolis parameter, l is a measure of the lateral scale over which parcels of fluid are transferred by baroclinic eddies, α is the constant of proportionality in (29) whose value was determined by laboratory and numerical experiment, and Ri is the (large-scale) Richardson number given by (30).

Spall and Chapman [1998] present a different derivation of the eddy flux relationship proposed by *Green* [1970] and employed by *Visbeck et al.* [1997] by considering how baroclinic eddies are formed in frontal zones and how they interact after they are formed. They obtain the same functional relationship proposed by *Green* [1970] and also find that the scaling coefficient α in (43) is indeed a nondimensional number. They deduce α to be 0.046. This is to be compared with the empirical value of 0.015 deduced by *Visbeck et al.* [1996] making use of Figure 45.

Visbeck et al. [1997] attempt to parameterize the eddy-induced velocity associated with the restratification and dispersal of a mixed patch. They compare their parameterized model with an eddy resolving nonhydrostatic simulation of a mixed patch in which both plumes and baroclinic instability are resolved. A linearly stratified volume of water is cooled at the surface over a disc as described in section 4 (see Figure 34). Azimuthally averaged sections across the baroclinic zone in the resolved model show the generation of a mixed patch due to convective mixing and its breakup by lateral fluxes due to baroclinic eddies. As time progresses, the lateral buoyancy transfer grows in magnitude until it is of sufficient magnitude to offset the surface buoyancy loss and establish a quasi-steady state (see section 4.3.3).

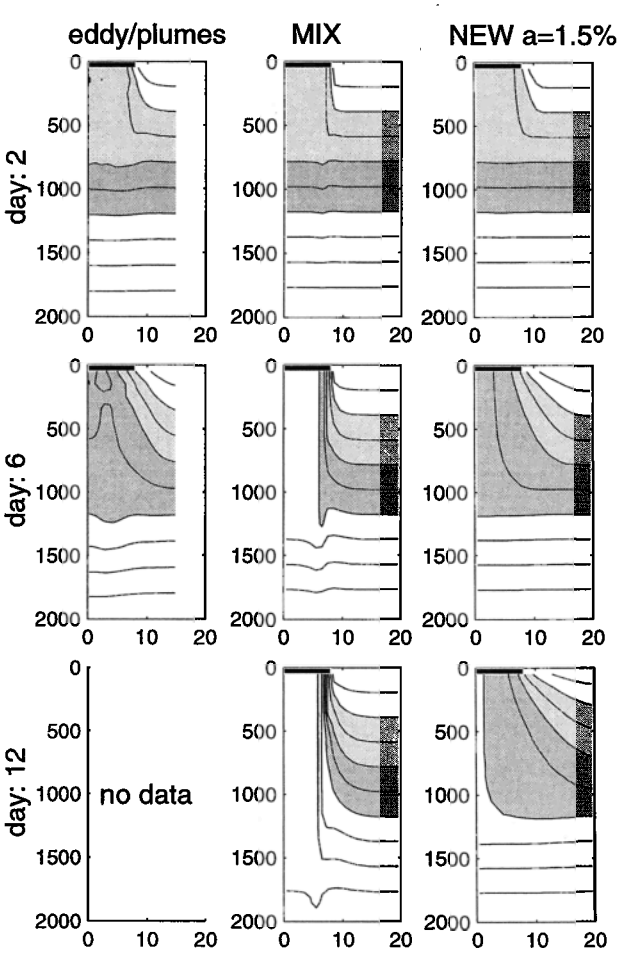

Figure 46. Azimuthally averaged density as a function of depth and radius at day 6 in a nonhydrostatic eddy-resolving model (left column), in a parameterized model using NEW (right), and horizontal diffusion (middle). The contour interval is 0.005 and two isopycnal layers are shaded. The black bar at the surface indicates the cooling region. From *Visbeck et al.* [1997].

In the right column of Figure 46 we show results from the parameterized model; a 2-D model was configured for an azimuthally averaged domain in which convective mixing in the vertical is represented by a convective adjustment scheme and eddy transfer is parameterized. A number of eddy parameterization schemes were compared, but the one that employed (38)–(43) was found to be the most satisfactory. This scheme, called "NEW" by *Visbeck et al.* [1997], combines the best elements of *Gent and McWilliams* [1990] (hereinafter referred to as GM) with *Green* [1970] and *Stone* [1972] (referred to collectively as GS): transfer coefficients that vary in space and time according to (43) (GS), together with the adoption of a transformed Eulerian mean formalism (GM). It predicts a large lateral buoyancy flux near the surface associated with the strong baroclinic zone of the rim current. At depth the convected fluid is advected outwards and appears as a layer of reduced stratification (see Figures 44 and 46).

In these mixed-patch simulations the eddy transfer scale l is set equal to the radius of the patch, and so the scheme has essentially only one tunable parameter, α. It was tuned to obtain the "best" results judged by comparison with the resolved experiment. The optimum value of α is 0.015 for the NEW scheme; the K implied by (43) is then 300 m^2 s^{-1} for the experiment shown in Figure 46 and is within a factor of 2 of that determined from laboratory experiments of mixed patches (see equation (32)).

Finally, note how poor is the "diffusive" parameterization (middle panel in Figure 46). Just as is observed in the global model of *Danabasoglu and McWilliams* [1995] (see Figure 45), the mixed patch is too deep, much deeper than in the resolved model.

5.3. Putting It All Together

Our comparison of resolved and parameterized models in sections 5.1 and 5.2 leads us to the following conclusions concerning the representation of the water mass transformation in large-scale models. We believe that gross aspects of the mixing process associated with convection can be captured by vertical adjustment schemes (or through the use of enhanced vertical mixing coefficients). The adjustment is never instantaneous, of course, and as was described in section 5.1.1, arrested adjustment schemes can be implemented and have satisfying properties. However, from the perspective of the large-scale flow, the mixing timescale (at most 12 hours) is essentially instantaneous; we find that the arrested and instantaneous schemes show no significant differences in parameter ranges of interest. Rather, it seems that the fidelity of water mass transformation in large-scale models is compromised largely by the representation of the exchange of the fluid and fluid properties to and from the convection site. Comparison of explicit and parameterized models clearly shows that (1) the "transformed Eulerian mean" representation advocated by *Gent and McWilliams* [1990] is an appropriate framework for describing the adiabatic dispersal of convectively modified fluid and (2) the transfer theory of Green and Stone is a useful closure to get at the magnitude and spatial variation of the eddy-induced velocity.

There are many outstanding questions, however, the most urgent of which is to understand what controls the eddy-transfer scale l. The importance of equation (43), however, is that it ascribes physical attributes to K and therefore a context for inquiry and further refinement of a transfer scale l, a timescale associated with baroclinic eddies M^2/N, and a proportionality constant α that measures the efficiency of the transfer process. A deeper understanding of those processes that determine these key factors [see *Larichev and Held*, 1995] is required before a more complete representation of K can be deduced.

To conclude our discussion of the parameterization of the water mass transformation process in models, we present results from a global 1° × 1° calculation using the Massachusetts Institute of Technology ocean circulation model (the model is described by *Marshall et al.* [1997a, b]). The ideas set out above have been implemented in that height coordinate model: a convective adjustment scheme of the kind described by *Klinger et al.* [1996] is used to represent convective mixing, and the NEW parameterization of geostrophic eddies described by *Visbeck et al.* [1997] is implemented (equations (38)–(43) above). The model, extending from 80°S to 80°N at 1° horizontal resolution, is configured with 20 levels in the vertical, ranging from 20 m at the surface to 500 m at the deepest level, typical of the oceanic component of coupled global models. Full spherical geometry and topography was employed.

Figure 47a shows the mixed-layer depth in March 1997, and Figure 47b shows the spatial variation in K given by the NEW parameterization, evaluated using the depth average of the stratification parameters over the top kilometer of the ocean, together with (43) and (30), as

$$K_h = \alpha l^2 \frac{1}{H} \int_{-H}^{0} \frac{M^2}{N} dz \qquad (44)$$

where H = 1 km and l was set to 400 km.

The general pattern of mixed-layer depth is not unrealistic: we see deep convecting regions (in excess of 2 km) in the Greenland and Labrador Seas with a tongue of shallower mixed layers (~200 m thick) extending southwestward across the basin to the south. The pattern of K shown in Figure 47b picks out regions that are known to be high in eddy activity (the Gulf Stream and North Atlantic Current, for example) falling to low background values of ~300 m^2 s^{-1} in the quiescent interiors of the subtropical gyres. The winter of 1991–1992 was indeed characterized by huge buoyancy loss over the Labrador Sea, and deep water was observed to a depth of 2500 m. However, there was no evidence that the mixed layer in the Greenland Sea during 1992 was as deep as is seen in Figure 47a. Thus although the model seems to be able to capture the preferred sites of deep convection (compare Figure 47 with Figure 1, for example), the depth of the mixing and the volume of fluid "processed" by it are sensitive to factors such as the prevailing meteorological fluxes, the underlying stratification, and the parameterization of lateral exchange.

6. CONCLUSIONS AND OUTLOOK

In this review we have attempted to draw together results of observations and of laboratory and numerical experiments and, in the context of relevant theory, summarize our current understanding of the underlying hydrodynamic processes at work at ocean convection sites and the interplay between the convective and geostrophic scales. We have seen that there is a complex interplay of scales, ranging from plumes at scales of <1 km, through eddies on and above the Rossby radius of de-

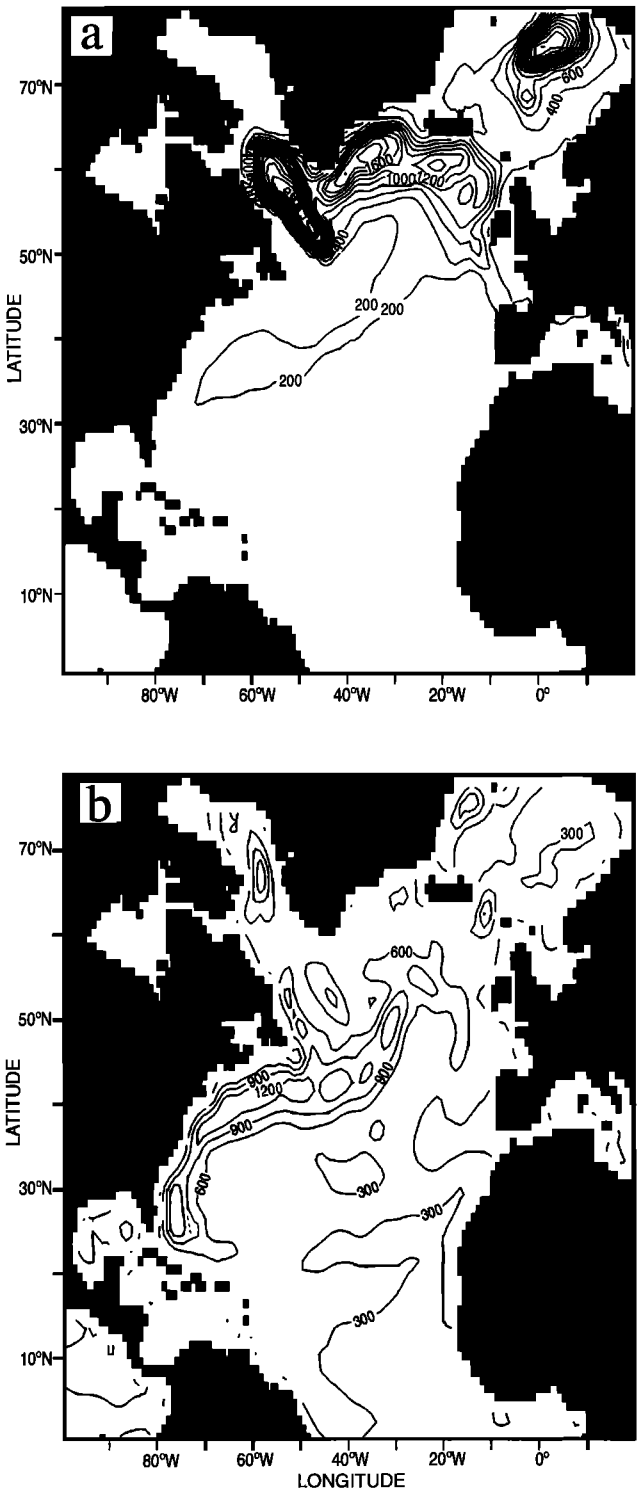

Figure 47. (a) Mixed layer depth in March in the Atlantic sector of a global integration of the MIT model at 1° horizontal resolution. (b) Spatial variation of the K values predicted by the NEW parameterization in the same calculation.

formation, right up to the scale of the general circulation. These key elements appear to be common to all open-ocean convection sites that have been studied. Moreover, the phenomenology that we have described in the context of deep convection goes on, we believe, in mixed layers all the time, everywhere in the ocean. However, the localized and deep-reaching nature of the convection regime exposes, in an exaggerated form, the role of lateral inhomogeneities and baroclinic instability. In the ocean there is little scale separation between the mixing (up-down) and geostrophic (lateral) processes: l_{rot}, H, and L_ρ are not very disparate, and the fluid is "stiffened" by rotation even on the convective scale itself. Herein lies the reason why water mass transformation is such a fascinating phenomenon from a theoretical point of view and why it is such a challenging and demanding process to observe and model.

It is worth remarking on the central role that new technologies and diverse methodologies have played in improving our description and understanding of the processes at work. Artful use of the ADCP and techniques of acoustic tomography have given us novel information about the dynamical processes at work as a function of scale. In the ongoing Labrador Sea experiment these techniques are being supplemented by profiling floats, Lagrangian floats that track fluid parcels in three dimensions, surface drifters, profiling CTDs, autonomous underwater vehicles, as well as hydrography and moorings, the stalwarts of observational oceanography [see *LabSea Group*, 1998].

It is interesting to note the central role played by laboratory experiments, such as those by *Maxworthy and Narimousa* [1994], in the development of the ideas reviewed here. These not only illuminated and exposed key theoretical questions in beautiful ways, but have also been a central thrust of the recent resurgence of interest in the general problem of rotating convection. Ocean convection has also been the context in which, for the first time, nonhydrostatic ocean models were developed and applied to the ocean [*Brugge et al.*, 1991; *Jones and Marshall*, 1993; *Marshall et al.*, 1997a, b].

The challenge for the future is to transform these insights in to parametric representations that address the complex 3-D nature of the processes at work. Representations widely used in large-scale models today remain stubbornly one dimensional and bear little relation to what we know of the process. Curiously, the more detailed our description becomes, from observations, laboratory, and numerical studies, the more it seems that the mixing process plays "second fiddle" to preexisting quasi-horizontal processes that are rapidly and vigorously energized as the convection proceeds.

As is often the case, the fidelity of our description of processes in models is severely compromised by inadequate resolution. Although in principle one could resolve down to the plume scale, this is neither possible (in the foreseeable future) nor desirable. In limited-area models, such as the one of the Labrador Sea shown in Figure 36, horizontal resolutions of a few kilometers can be achieved. We believe that the fidelity of the representation of the water mass transformation process will then depend largely on the quality of the forcing fluxes (of heat, fresh water and momentum) and knowledge of

the preexisting stratification, rather than the details of assumed vertical mixing scheme. However, in the global models used for climate research it is the representation of the geostrophic scales that remain the key. Use of the transformed Eulerian mean as advocated by *Gent and McWilliams* [1990] provides a solid basis on which to contemplate the adiabatic part of the process. Use of an eddy-induced velocity, which depends on the large-scale Richardson number following *Green* [1970], provides a context for quantifying the vigor of the lateral exchange process.

What are the outstanding problems? The fluid dynamics and interplay of scales that we have described are very complex, involving nonhydrostatic phenomena, mixing, phase changes and nonlinearity in the equation of state, rotation effects, intermittency in space and time, etc. There are many matters of detail to sort out, but there also remain a number of important unsolved "conceptual" problems: What is the fate of convected water in the months and years after it has been created? How does it "feed" the thermohaline circulation, and how is it accommodated into the general circulation of the ocean? There does not appear to be a straightforward connection between the "sinking branch" of the thermohaline circulation and the convective activity at the sites shown in Figure 1. Finally, there is the question of the extent to which the thermohaline circulation is "pulled" by mixing processes in the interior, rather than "pushed" by the convective process discussed here.

ACKNOWLEDGMENTS. We acknowledge numerous conversations with colleagues and collaborators that contributed to the ideas, methods and data that are presented and explored in this review. We thank A. Eisele and B. Brown for their drafting work, L. McFarren for help in the preparation of the text, C. Mertens for his assistance in the data analysis, and J. Lazier for letting us use section data from R/V *Dawson*. J.M. has received support from NSF, NOAA, ONR and the TEPCO Electric Power Company for his studies of convection and thermohaline circulation. F.S. acknowledges support from DFG and from BMBF.

Tommy Dickey is the Editor responsible for this paper. He thanks Shafiqui Islam and three anonymous referees for their reviews.

REFERENCES

Adkins, J. A., and E. A. Boyle, Changing atmospheric $\Delta^{14}C$ and the record of deep water paleoventilation ages, *Paleoceanography*, *12*, 337–344, 1997.

Alverson, K., Mechanisms for lateral exchange with oceanic convection sites, *J. Phys. Oceangr.*, *27*, 1436–1446, 1997.

Alverson, K., and B. Owens, Topographic preconditioning of open-ocean deep convection, *J. Phys. Oceangr.*, *26*, 2196–2213, 1996.

Alves, J. O. S., Open-ocean deep convection: Understanding and parameterizations, Ph.D. thesis, Univ. of Reading, Reading, England, 1995.

Andrews, D., J. Holton, and C. Leovy, *Middle Atmosphere Dynamics*, 489 pp., Academic, San Diego, Calif., 1987.

Arakawa, A., and W. Schubert, Interaction of cumulus cloud ensemble with the large-scale environment, I, *J. Atmos. Sci.*, *31*, 674–701, 1974.

Astraldi, M., and G. P. Gasparini, The seasonal characteristics of the north Mediterranean Basin and their relationship with atmospheric-climatic conditions, *J. Geophys. Res.*, *97*, 9531–9540, 1992.

Ayotte, B., and H. Fernando, The motion of a turbulent thermal in the presence of background rotation, *J. Atmos. Sci.*, *51*(13), 1989–1994, 1994.

Benard, H., Les tourbillons cellulaires dans une nappe liquide, *Rev. Gen. Sci. Pures Appl.*, *11*, 1261–1271, 1309–1328, 1900.

Bethoux, J. P., Mean water fluxes across sections in the Mediterranean Sea, evaluated on the basis of water and salt budgets and of observed salinities, *Oceanol. Acta*, *3*(1), 79–88, 1980.

Bignami, F., S. Marullo, R. Santoleri, and M. E. Schiano, Longwave radiation budget in the Mediterranean Sea, *J. Geophys. Res.*, *100*(C2), 2501–2514, 1995.

Boubnov, B. M., and G. S. Golitsyn, Experimental study of convection structures in rotating fluids, *J. Fluid Mech.*, *167*, 503–531, 1986.

Boubnov, B. M., and G. S. Golitsyn, Temperature and velocity field regimes of convective motions in a rotating plane fluid layer, *J. Fluid Mech.*, *219*, 215–239, 1990.

Boubnov, B. M., and G. S. Golitsyn, *Convection in Rotating Fluids*, 224 pp., Kluwer Acad., Norwell, Mass., 1995.

Boyle, E. A., Cd and $\delta^{13}C$ paleochemical ocean distributions during the stage 2 glacial maximum, *Annu. Rev. Earth Planet. Sci.*, *20*, 245–287, 1992.

Bretherton, F. P., Critical layer instability in baroclinic flows, *Q. J. R. Meteorol. Soc.*, *92*, 325–334, 1966.

Brickman, D., Heat flux partitioning in open-ocean deep convection, *J. Phys. Oceangr.*, *25*, 2609–2623, 1995.

Brickman, D., and D. Kelley, Development of convection in a rotating fluid: Scales and patterns of motion, *Dyn. Atmos. Oceans*, *19*, 389–405, 1993.

Brugge, R., H. L. Jones, and J. C. Marshall, Non-hydrostatic ocean modeling for studies of open-ocean deep convection, in *Proceedings of the Workshop on Deep Convection and Deep Water Formation in the Oceans*, *Elsevier Oceanogr. Ser.*, edited by J.-C. Gascard, pp. 325–340, Elsevier, New York, 1991.

Bryan, K., A numerical model for the study of the circulation of the world ocean, *J. Comput. Phys.*, *4*, 347–376, 1969.

Bryden, H. L., and T. H. Kinder, Steady two-layer exchange through the Strait of Gibraltar, *Deep Sea Res.*, *38*, *Part A*, suppl., 445–463, 1991.

Bryden, H. L., and H. M. Stommel, Limiting processes that determine basic features of the circulation in the Mediterranean Sea, *Oceanol. Acta.*, *7*(3), 289–296, 1984.

Bunker, A. F., Computations of surface energy flux and annual air-sea interaction cycles of the North Atlantic, *Mon. Weather Rev.*, *116*, 809–823, 1976.

Carmack, E., and K. Aagaard, On the deep water of the Greenland Sea, *Deep Sea Res.*, *20*, 687–715, 1973.

Carmack, E., K. Aagaard, J. H. Swift, R. W. MacDonald, F. A. McLaughlin, E. P. Jones, R. G. Perkin, J. N. Smith, K. M. Ellis, and L. R. Killius, Changes in temperature and tracer distributions within the Arctic Ocean: Results from the 1994 Arctic Ocean section, *Deep Sea Res.*, *Part II*, *44*, 1487–1502, 1997.

Cayan, D., Latent and sensible heat flux anomalies over the northern oceans: The correction to monthly atmospheric circulation, *J. Clim.*, *5*, 354–369, 1992.

Cessi, P., Grid-scale instability of convective-adjustment schemes, *J. Mar. Res.*, *54*, 407–420, 1996.

Chandrasekhar, S., The instability of a layer of fluid heated

below and subject to Coriolis forces, *Proc. R. Soc. London., Ser. A, 217*, 306–327, 1953.
Chandrasekhar, S., *Hydrodynamic and Hydro Magnetic Stability*, 652 pp., Clarendon Press, Oxford, England, 1961.
Chapman, D. C., Setting the scales of the ocean response to isolated convection, *J. Phys. Oceanogr., 28*, 606–620, 1998.
Chapman, D. C., and G. Gawarkiewicz, Shallow convection and buoyancy equilibration in an idealized coastal polynya, *J. Phys. Oceanogr., 27*, 555–566, 1997.
Clarke, R. A., and J.-C. Gascard, The formation of Labrador Sea water, I, Large-scale processes, *J. Phys. Oceanogr., 13*, 1764–1788, 1983.
Coates, M. J., and G. N. Ivey, On convective turbulence and the influence of rotation, *Dyn. Atmos. Oceans, 25*, 217–232, 1997.
Coates, M. J., G. V. Ivey, and J. R. Taylor, Unsteady, turbulent convection in to a rotating linearly stratified fluid: Modeling deep ocean convection, *J. Phys. Oceanogr., 25*, 3032–3050, 1995.
Cox, M., A primitive equation, three-dimensional model of the ocean, *Rep. 1*, Ocean Group, Geophys. Fluid Dyn. Lab., Princeton, N. J., 1984.
Crepon, M., M. Boukthir, B. Barnier, and F. Aikman, Horizontal ocean circulation forced by deep-water formation, I, Analytical study, *J. Phys. Oceanogr., 19*, 1781–1793, 1989.
Curry, W. B., J. C. Duplessy, L. D. Labeyrie, and N. J. Shackleton, Changes in the distribution of ^{13}C of deep water CO_2 between the last glaciation and the Holocene, *Paleoceanography, 3*, 317–342, 1988.
Danabasoglu, G., and J. C. McWilliams, Sensitivity of the global ocean circulation to parameterization of mesoscale tracer transports, *J. Clim., 8*, 2967–2980, 1995.
Davey, M. K., and J. A. Whitehead Jr., Rotating Rayleigh-Taylor instability as a model for sinking events in the ocean, *Geophys. Astrophys. Fluid Dyn., 17*, 237–253, 1981.
Deardorff, J. W., Mixed-layer entrainment: A review, in *The Symposium in Turbulence and Diffusion*, edited by J. C. Weil, pp. 39–42, 1985.
Deardorff, J. W., G. E. Willis, and B. H. Stockton, Laboratory studies of the entrainment zone of a convectively mixed layer, *J. Fluid Mech., 100*, 41–64, 1980.
Denbo, D. W., and E. D. Skyllingstad, An ocean large eddy model with application to deep convection in the Greenland Sea, *J. Geophys. Res., 101*, 1095–1111, 1996.
Dickson, R., J. Lazier, J. Meinke, P. Rhines, and J. Swift, Long-term coordinated changes in the convective activity of the North Atlantic, *Prog. Oceanogr., 38*, 241–295, 1996.
Duplessy, J.-C., M. Arnold, E. Bard, A. Juillet-Leclerc, N. Kallel, and L. Labeyrie, AMS ^{14}C study of transient events and of the ventilation rate of the Pacific intermediate water during the last deglaciation, *Radiocarbon, 31*, 493–502, 1989.
Eady, E. T., Long waves and cyclone waves, *Tellus, 1*, 33–52, 1949.
Emanuel, K., *Atmospheric Convection*, 580 pp., Oxford Univ. Press, New York, 1984.
Emery, W. J., W. G. Lee, and L. Magaard, Geographical and seasonal distribution of Brunt-Väisälä frequency and Rossby radii in the N. Atlantic and N. Pacific, *J. Phys. Oceanogr., 14*, 294–317, 1994.
Fernando, H. J. S., and C. Y. Ching, Effects of background rotation on turbulent plumes, *J. Phys. Oceanogr., 23*, 2115–2129, 1994.
Fernando, J. S. F., R. Chen, and D. L. Boyer, Effects of rotation on convection turbulence, *J. Fluid Mech., 228*, 513–547, 1991.
Fritsch, J. M., and C. F. Chappell, Numerical prediction of convectively driven mesoscale pressure systems, 1, Convective parameterization, *J. Atmos. Sci., 37*, 1722–1733, 1980.
Garwood, R. W., S. M. Isakari, and P. Gallacher, Thermobaric convection, in *The Polar Oceans and Their Role in Shaping the Global Environment: The Nansen Centennial Volume, Geophys. Monogr. Ser.*, vol. 85, edited by O. M. Johannessen, R. D. Muench, and J. E. Overland, 199–206, AGU, Washington, D. C., 1994.
Gascard, J.-C., Mediterranean deep water formation, baroclinic eddies and ocean eddies, *Oceanol. Acta., 1*, 313–315, 1978.
Gascard, J.-C., and A. C. Clarke, The formation of Labrador Sea water, II, Mesoscale and smaller-scale processes, *J. Phys. Oceanogr., 13*, 1779–1797, 1983.
Gawarkiewicz, G., T. Weingartner, and D. C. Chapman, Sea ice processes and water mass modification and transport over Arctic shelves, in *The Sea*, vol. 10, *The Global Coastal Ocean*, edited by K. H. Brink and A. R. Robinson, pp. 171–190, John Wiley, New York, 1997.
Gent, P., and J. McWilliams, Isopycnal mixing in ocean circulation models, *J. Phys. Oceanogr., 20*, 150–155, 1990.
Gill, A., Circulation and bottom water in the Weddell Sea, *Deep Sea Res., 20*, 111–140, 1973.
Golitsyn, G. S., Geostrophic convection (in Russian), *Dokl. Akad. Nauk. SSSR, 251*, 1356–1360, 1980.
Gordon, A. L., Weddel deep water variability, *J. Mar. Res., 40*, suppl., 199–217, 1982.
Green, J. A., Transfer properties of the large-scale eddies and the general circulation of the atmosphere, *Q. J. R. Meteorol. Soc., 96*, 157–185, 1970.
Gregory, D., and P. R. Rowntree, A mass flux convection scheme with representation of cloud ensemble characteristics and stability dependent closure, *Mon. Weather Rev., 118*, 1483–1506, 1990.
Haine, T., and J. Marshall, Gravitational, symmetric and baroclinic instability of the ocean mixed layer, *J. Phys. Oceanogr., 28*, 634–658, 1998.
Hallberg, R., and P. Rhines, Buoyancy-driven circulation in an ocean basin with isopycnals intersecting the sloping bottom, *J. Phys. Oceanogr., 26*, 913–940, 1996.
Heburn, G. W., The dynamics of the western Mediterranean Sea: A wind forced case study, *Ann. Geophys., Ser. B, 5*(1), 61–74, 1987.
Helfrich, K., Thermals with background rotation and stratification, *J. Fluid Mech., 259*, 265–280, 1994.
Helfrich, K., and U. Send, Finite-amplitude evolution of two-layer geostrophic vortices, *J. Fluid Mech., 197*, 331–348, 1988.
Herman, O., and B. Owens, Energetics of gravitational adjustment for mesoscale chimneys, *J. Phys. Oceanogr., 23*, 346–371, 1993.
Hermann, A. L., Rhines, and E. R. Johnson, Nonlinear Rossby adjustment in a channel: Beyond Kelvin waves, *J. Fluid Mech., 205*, 460–502, 1989.
Hogg, N., The preconditioning phase of MEDOC 1969, II, Topographic effects, *Deep Sea Res., 20*, 449–459, 1973.
Hogg, N., and H. Stommel, Hetonic explotions: The breakup and spread of warm pools as explained by baroclinic point vortices, *J. Atmos. Sci., 42*, 1456–1476, 1985.
Hoskins, B., M. McIntyre, and A. Robertson, On the use and significance of isentropic potential vorticity maps, *Q. J. R. Meteorol. Soc., 111*, 877–946, 1985.
Howard, L. N., Convection at high Rayleigh number, *Proc. Int. Congr. Appl. Mech., 11th*, 405–432, 1964.
Jones, H., and J. Marshall, Convection with rotation in a neutral ocean: A study of open-ocean deep convection, *J. Phys. Oceanogr., 23*, 1009–1039, 1993.
Jones, H., and J. Marshall, Restratification after deep convection, *J. Phys. Oceanogr., 27*, 2276–2287, 1997.
Julien, K., S. Legg, J. McWilliams, and J. Werne, Penetrative convection in rapidly rotating flows: Preliminary results from numerical simulation, *Dyn. Atmos. Oceans, 24*, 237–249, 1996a.
Julien, K., S. Legg, J. McWilliams, and J. Werne, Rapidly

rotating turbulent Raleigh-Benard convection, *J. Fluid Mech.*, *322*, 243–273, 1996b.

Kaempf, J., and J. O. Backhaus, Shallow brine-driven free convection in polar oceans: Nonhydrostatic process studies, *103*(C3), 5577–5593, 1998.

Keigwin, L. D., North Pacific Deep Water formation during the latest glaciation, *Nature*, *330*, 362–364, 1987.

Kelley, D. E., Fluxes through diffusive staircases: A new formulation, *J. Geophys. Res.*, *95*(C3), 3365–3371, 1990.

Kerr, R. M., J. R. Herring, and A. Brandenburg, Large-scale structure in Rayleigh-Benard convection with impenetrable sidewalls, *Chaos Solitons Fractals*, *5*(10), 20–47, 1995.

Killworth, P. D., The mixing and spreading phase of MEDOC 1969, *Prog. Oceanogr.*, *7*, 59–90, 1976.

Killworth, P. D., On chimney formation in the ocean, *J. Phys. Oceanogr.*, *9*, 531–554, 1979.

Killworth, P. D., Deep convection in the world ocean, *Rev. Geophys.*, *21*(1), 1–26, 1983.

Klinger, B., and J. Marshall, Regimes and scaling laws for rotating deep convection in the ocean, *Dyn. Atmos. Oceans*, *21*, 227–256, 1995.

Klinger, B., J. Marshall, and U. Send, Representation of convective plumes by vertical adjustment, *J. Geophys. Res.*, *101*(C8), 18,175–18,182, 1996.

Krahmann, G., Saisonale und zwischenjhrliche Variabiltim westlichen Mittelmeer—Analyse historischer Daten, dissertation, 168 pp., Univ. Kiel, Kiel, Germany, 1997.

Kraus, E. B., and J. S. Turner, A one-dimensional model of the seasonal thermocline, II, The general theory and its consequences, *Tellus*, *19*, 98–105, 1967.

LabSea Group, The Labrador Sea Deep Convection Experiment, *Bull. Am. Meteorol. Soc.*, *79*(10), 2033–2058, 1998.

Large, W., J. McWilliams, and S. Doney, Oceanic vertical mixing: A review and a model with a nonlocal boundary layer parameterization, *Rev. Geophys.*, *32*, 336–403, 1994.

Larichev, V., and I. Held, Eddy amplitudes and fluxes in a homogenous model of fully developed baroclinic instability, *J. Phys. Oceanogr.*, *25*, 2285–2297, 1995.

Lascaratos, A., R. G. Williams, and E. Tragou, A mixed-layer study of the formation of Levantine Intermediate Water, *J. Geophys. Res.*, *98*(C8), 14,739–14,749, 1993.

Lazier, J. R., The renewal of Labrador Sea Water, *Deep Sea Res.*, *20*, 341–353, 1973.

Lazier, J. R., Oceanographic conditions at ocean weather ship *Bravo*, 1964–1974, *Atmos. Ocean*, *18*, 227–238, 1980.

Lazier, J. R., Temperature and salinity changes in the deep Labrador Sea, 1962–1986, *Deep Sea Res.*, *35*, 1247–1253, 1988.

Lazier, J. R., The salinity decrease in the Labrador Sea over the past thirty years, *Ocean Obs.*, 295–304, 1995.

Leaman, K. D., and F. Schott, Hydrographic structure of the convection regime in the Golfe du Lion, *J. Phys. Oceanogr.*, *21*, 575–598, 1991.

Legg, S., and J. Marshall, A heton model of the spreading phase of open-ocean deep convection, *J. Phys. Oceanogr.*, *23*, 1040–1056, 1993.

Legg, S., and J. Marshall, The influence of the ambient flow on the spreading of convected water masses, *J. Mar. Res.*, *56*, 107–139, 1998.

Legg, S., H. Jones, and M. Visbeck, A heton perspective on baroclinic eddy transfer in localised ocean convection, *J. Phys. Oceanogr.*, *26*, 2251–2266, 1996.

Levitus, S., and T. Boyer, *World Ocean Atlas*, vol. 4, *Temperature, NOAA Atlas NESDIS 4*, 150 pp., U.S. Gov. Print. Off., Washington, D. C., 1994.

Levitus, S., R. Burgett, and T. Boyer, *World Ocean Atlas*, vol. 3, *Salinity, NOAA Atlas NESDIS 4*, 150 pp., U.S. Gov. Print. Off., Washington, D. C., 1994.

Macdonald, A., and C. Wunsch, A global estimate of the ocean circulation and heat fluxes, *Nature*, *382*, 436–439, 1996.

Madec, G., M. Chartier, P. Delecluse, and M. Crepon, A three-dimensional numerical study of deep-water formation in the northwestern Mediterranean Sea, *J. Phys. Oceanogr.*, *21*, 1349–1371, 1991.

Mammerickx, J., A deep-sea thermohaline flow path in the northwest Pacific, *Mar. Geol.*, *65*, 1–19, 1985.

Marotzke, J., Influence of convective adjustment on the stability of the thermohaline circulation, *J. Phys. Oceanogr.*, *21*, 903–907, 1991.

Marshall, D., Subduction of water masses in an eddying ocean, *J. Mar. Res.*, *55*, 201–222, 1997.

Marshall, J. C., A. J. G. Nurser, and R. G. Williams, Inferring the subduction rate and period over the North Atlantic, *J. Phys. Oceanogr.*, *23*, 1315–1329, 1993.

Marshall, J., J. A. Whitehead, and T. Yates, Laboratory and numerical experiments in oceanic convection, *Ocean Processes in Climate Dynamics: Global and Mediterranean Examples*, edited by P. Malanotte-Rizzoli and A. Robinson, 437 pp., Kluwer Acad., Norwell, Mass., 1994.

Marshall, J., C. Hill, L. Perelman, and A. Adcroft, Hydrostatic, quasi-hydrostatic, and nonhydrostatic ocean modeling, *J. Geophys. Res.*, *102*(C3), 5733–5752, 1997a.

Marshall, J., A. Adcroft, C. Hill, L. Perelman, and C. Heisey, A finite-volume, incompressible Navier-Stokes model for studies of the ocean on parallel computers, *J. Geophys. Res.*, *102*(C3), 5753–5766, 1997b.

Mason, P. J., Large-eddy simulation: A critical review of the technique, *Q. J. R. Meteorol. Soc.*, *120*, 1–26, 1994.

Maxworthy, T., Convection into domains with open boundaries, *Annu. Rev. Fluid Mech.*, *29*, 327–371, 1997.

Maxworthy, T., and S. Narimousa, Vortex generation by convection in a rotating fluid, *Ocean Modell.*, *92*, pp. 1007–1008, Hooke Inst., Univ. of Oxford, Oxford, England, 1991.

Maxworthy, T., and S. Narimousa, Unsteady, turbulent convection into a homogeneous, rotating fluid, with oceanographic application, *J. Phys. Oceanogr.*, *24*, 865–887, 1994.

McDougall, T. J., Greenland Sea Bottom Water formation: A balance between advection and double-diffusion, *Deep Sea Res., Part A*, *30*, 1109–1118, 1983.

MEDOC Group, Observations of formation of deep-water in the Mediterranean Sea, 1969, *Nature*, *227*, 1037–1040, 1970.

Mertens, C., Winterliche Deckschichtentwicklung und ihre zwischenjahrliche Variabilität im nordwestlichen Mittelmeer, Diploma thesis, Kiel Univ., Kiel, Germany, 1994.

Mertens, C., and F. Schott, Interannual variability of deep convection in the northwestern Mediterranean, *J. Phys. Oceanogr.*, *28*, 1410–1424, 1998.

Millot, C., The circulation of the Levantine Intermediate Water in the Algerian Basin, *J. Geophys. Res.*, *92*(C8), 8265–8276, 1987.

Millot, C., Mesoscale and seasonal variabilities of the circulation in the western Mediterranean, *Dyn. Atmos. Oceans*, *15*, 179–214, 1991.

Moore, G. W. K., Atmospheric forcing of deep convection in the Labrador Sea, 23 pp., Univ. of Toronto, Toronto, Ont., Canada, 1996.

Morawitz, W. M. L., P. J. Sutton, P. F. Worcester, B. D. Cornelle, J. F. Lynch, and R. Pawlowicz, Three-dimensional observations of a deep convective chimney in the Greenland Sea diving during winter 1988/89, *J. Phys. Oceanogr.*, *26*, 2316–2343, 1996.

Muench, R. D., H. J. S. Fernando, and G. R. Stegan, Temperature and salinity staircases in the northwestern Weddell Sea, *J. Phys. Oceanogr.*, *20*, 295–306, 1990.

Nakagawa, Y., and P. Frenzen, A theoretical and experimental study of cellular convection in rotating fluids, *Tellus*, *7*, 1–21, 1955.

Narimousa, S., Penetrative turbulent convection into a rotating two-layer fluid, *J. Fluid Mech.*, *321*, 299–313, 1996.

Narimousa, S., Dynamics of mesoscale vortices generated by turbulent convection at large aspect ratios, *J. Geophys. Res.*, *102*(C3), 5615–5624, 1997.

Narimousa, S., Turbulent convection into a linearly stratified fluid: The generation of subsurface anticyclones, *J. Fluid Mech.*, *354*, 101–121, 1998.

Niiler, P. P., Deepening of the wind-mixed layer, *J. Mar. Res.*, *33*, 405–421, 1975.

Niiler, P. P., and E. B. Kraus, One-dimensional models of the upper ocean, in *Modelling and Prediction of the Upper Layers of the Ocean*, edited by E. B. Kraus, pp. 143–172, Pergamon, Tarrytown, New York, 1977.

Nurser, A. J. G., *Models and Observations of the Oceanic Mixed Layer, Elsevier Oceanogr. Ser.*, edited by D. Halpern, 254 pp., Elsevier, New York, 1998.

Padman, L., and T. M. Dillon, Vertical fluxes through the Beaufort Sea thermohaline staircase, *J. Geophys. Res.*, *92*(C10), 10,799–10,806, 1987.

Padman, L., and T. Dillon, On the horizontal extent of the Canada Basin thermohaline steps, *J. Phys. Oceanogr.*, *18*, 1458–1462, 1988.

Paluszkiewicz, T., and R. D. Romea, A one-dimensional model for the parameterization of deep convection in the ocean, *Dyn. Atmos. Oceans*, *26*, 95–130, 1997.

Paluszkiewicz, T., R. Garwood, and D. W. Denbo, Deep convective plumes in the ocean, *Oceanography*, *7*, 37, 1994.

Pedlosky, J., The instability of a continuous heton cloud, *J. Atmos. Sci.*, *42*, 1477–1480, 1985.

Pickart, R. S., Water mass components of the North Atlantic deep western boundary current, *Deep Sea Res., Part A*, *39*, 1553–1572, 1992.

Pollard, R. T., P. B. Rhines, and R. O. R. Y. Thompson, The deepening of the wind-mixed layer, *Geophys. Fluid Dyn.*, *3*, 381–404, 1973.

Price, J. F., R. A. Weller, and R. Pinkel, Diurnal cycling: Observations and models of the upper ocean response to diurnal heating, cooling and wind mixing, *J. Geophys. Res.*, *91*(C7), 8411–8427, 1986.

Raasch, S., and D. Etling, Numerical simulation of rotating turbulent thermal convection, *Contrib. Atmos. Phys.*, *3*, 1–15, 1991.

Rahmstorf, S., A zonal-averaged model of the ocean's response to climatic change, *J. Geophys. Res.*, *96*(C4), 6951–6963, 1991.

Rayleigh, O. M., On convection currents in a horizontal layer of fluid, when the higher temperature is on the lower side, *Philos. Mag., Ser. 6*, *32*, 529–546, 1916.

Rhein, M., Ventilation rates of the Greenland and Norwegian Seas derived from distributions of the chlorofluoromethanes F11 and F12, *Deep Sea Res., Part A*, *38*, 485–503, 1991.

Rhein, M., Deep water formation in the western Mediterranean, *J. Geophys. Res.*, *100*(C4), 6943–6959, 1995.

Roach, A. T., K. Aagaard, and F. D. Carsey, Coupled ice-ocean variability in the Greenland Sea, *Atmos. Ocean*, *31*, 319–337, 1993.

Rogers, J. C., Patterns of low-frequency monthly sea level pressure variability (1899–1986) and associated wave cyclone frequencies, *J. Clim.*, *3*, 1364–1379, 1990.

Rossby, H. T., A study of Benard convection driven by nonuniform heating from below. An experimental study, *Deep Sea Res.*, *12*, 9–16, 1965.

Rudels, B., Haline convection in the Greenland Sea, *Deep Sea Res.*, *37*(9), 1491–1511, 1990.

Rudels, B., D. Quadfasel, H. Friedrich, and M.-N. Houssais, Greenland Sea convection in the winter of 1987–1988, *J. Geophys. Res.*, *94*(C3), 3223–3227, 1989.

Sander, J., D. Wolf-Gladrow, and D. Olbers, Numerical studies of open-ocean deep convection, *J. Geophys. Res.*, *100*(C10), 20,579–20,600, 1995.

Sandven, S., O. M. Johannessen, and J. A. Johannessen, Mesoscale eddies and chimneys in the marginal ice zone, *J. Mar. Syst.*, *2*, 195–208, 1991.

Saunders, P. M., The instability of a baroclinic vortex, *J. Phys. Oceanogr.*, *3*, 61–65, 1973.

Schiano, M. E., R. Santoleri, F. Bignami, R. M. Leonardi, S. Marullo, and E. Bohm, Air-sea interaction measurements in the west Mediterranean Sea during the Tyrrhenian Eddy Multiplatform Observations experiment, *J. Geophys. Res.*, *98*(C2), 2461–2474, 1993.

Schlosser, P., G. Bvnisch, M. Rhein, and R. Bayer, Reduction of deepwater formation in the Greenland Sea during the 1980s: Evidence from tracer data, *Science*, *251*, 1054–1056, 1991.

Schmitt, R. W., Double diffusion in oceanography, *Annu. Rev. Fluid Mech.*, *26*, 255–285, 1994.

Schmitt, R. W., and D. B. Olson, Wintertime convection in warm core rings: Thermocline ventilation and the formation of mesoscale lenses, *J. Geophys. Res.*, *90*, 8823–8837, 1985.

Schott, F., and K. D. Leaman, Observations with moored acoustic Doppler current profilers in the convection regime in the Golfe du Lion, *J. Phys. Oceanogr.*, *21*, 558–574, 1991.

Schott, F., M. Visbeck, and J. Fischer, Observations of vertical currents and convection in the central Greenland Sea during the winter of 1988/89, *J. Geophys. Res.*, *98*(C8), 14,401–14,421, 1993.

Schott, F., M. Visbeck, and U. Send, Open ocean deep convection, Mediterranean and Greenland Seas, in *Ocean Processes on Climate Dynamics: Global and Mediterranean Examples*, edited by P. Malanotte-Rizzoli and A. R. Robinson, pp. 203–225, Kluwer Acad., Norwell, Mass., 1994.

Schott, F., M. Visbeck, U. Send, J. Fischer, L. Stramma, and Y. Desaubies, Observations of deep convection in the Gulf of Lions, northern Mediterranean, during the winter of 1991/92, *J. Phys. Oceanogr.*, *26*, 505–524, 1996.

Send, U., and J. Marshall, Integral effects of deep convection, *J. Phys. Oceanogr.*, *25*, 855–872, 1995.

Send, U., F. Schott, F. Gaillard, and Y. Desaubies, Observation of a deep convection regime with acoustic tomography, *J. Geophys. Res.*, *100*(C4), 6927–6941, 1995.

Send, U., J. Font, and C. Mertens, Recent observation indicates convection's role in deep circulation, *Eos Trans. AGU*, *77*(7), 61–65, 1996.

Smethie, W. M., Jr., H. G. Ostlund, and H. H. Loosli, Ventilation of the deep Greenland and Norwegian Seas: Evidence from krypton-85, tritium, carbon-14 and argon-39, *Deep Sea Res., Part A*, *33*, 675–703, 1986.

Smith, S. D., Coefficients for sea surface wind stress, heat flux, and wind profiles as a function of wind speed and temperature, *J. Geophys. Res.*, *93*(C12), 15,467–15,472, 1988.

Smith, S. D., Water vapor flux at the sea surface, *Boundary Layer Meteorol.*, *47*, 277–293, 1989.

Smith, S. D., and F. W. Dobson, The heat budget at ocean weather ship *Bravo*, *Atmos. Ocean*, *22*, 1–15, 1984.

Spall, M. A., and D. C. Chapman, On the efficiency of baroclinic eddy heat transport, *J. Phys. Oceanogr.*, *28*, 2275–2287, 1998.

Sparnocchia, S., P. Picco, G. M. R. Manzella, A. Ribotti, S. Copello, and P. Brasey, Intermediate water formation in the Ligurian Sea, *Oceanol. Acta*, *18*(2), 151–162, 1995.

Stommel, H., A. Voorhis, and D. Webb, Submarine clouds in the deep ocean, *Am. Sci.*, *59*, 717–723, 1971.

Stone, P., Baroclinic instability under nonhydrostatic conditions, *J. Fluid Mech.*, *45*, 659–671, 1970.

Stone, P., A simplified radiative-dynamical model for the static stability of rotating atmospheres, *J. Atmos. Sci.*, *29*, 405–418, 1972.

Swallow, J. C., and G. F. Caston, The preconditioning phase of

MEDOC 1969, 1, Observations, *Deep Sea Res.*, *20*, 429–448, 1973.

Talley, L. D., and M. S. McCartney, Distribution and circulation of Labrador Sea water, *J. Phys. Oceanogr.*, *12*, 1189–1205, 1982.

THETIS Group (F. Schott et al.), Open-ocean deep convection explored in the Mediterranean, *Eos Trans. AGU*, *75*(19), 217–221, 1994.

Treguier, A., I. Held, and V. Larichev, On the parameterization of quasigeostrophic eddies in primitive equation ocean models, *J. Phys. Oceanogr.*, *27*, 567–580, 1997.

Turner, J. S., *Buoyancy Effects in Fluids*, 368 pp., Cambridge Univ. Press, New York, 1973.

van Loon, H., and J. C. Rogers, The seesaw in winter temperatures between Greenland and northern Europe, I, General description, *Mon. Weather Rev.*, *106*, 296–310, 1978.

Veronis, G., Cellular convection with finite amplitude in a rotating fluid, *J. Fluid Mech.*, *5*, 401–435, 1959.

Veronis, G., On properties of sea water defined by temperature, salinity and pressure, *J. Mar. Res.*, *30*, 227–255, 1972.

Vinje, T., Sea ice conditions in the European sector of the marginal seas of the Arctic, 1966–75, *Aarb. Nor. Polarinst.*, 163–174, 1977.

Visbeck, M., Observations of convective "plumes" in the ocean, paper presented at GFD Summer School on Rotating Convection, Woods Hole Oceanogr. Inst., Woods Hole, Mass., 1995.

Visbeck, M., J. Fischer, and F. Schott, Preconditioning the Greenland Sea for deep convection: Ice formation and ice drift, *J. Geophys. Res.*, *100*(C9), 18,489–18,502, 1995.

Visbeck, M., J. Marshall, and H. Jones, Dynamics of isolated convective regions in the ocean, *J. Phys. Oceanogr.*, *26*, 1721–1734, 1996.

Visbeck, M., J. Marshall, T. Haine, and M. Spall, Specification of eddy transfer coefficients in coarse-resolution ocean circulation models, *J. Phys. Oceanogr.*, *27*, 381–402, 1997.

Voorhis, A. D., and D. C. Webb, Large vertical currents observed in a winter sinking region of the northwestern Mediterranean, *Cah. Oceanogr.*, *22*, 571–580, 1970.

Wadhams, P., J. C. Comiso, E. Prussen, S. Wells, M. Brandon, E. Aldworth, T. Viehoff, R. Allegrino, and D. R. Crane, The development of the Odden Ice Tongue in the Greenland Sea during winter 1993 from remote sensing and field observations, *J. Geophys. Res.*, *101*(C8), 18,213–18,235, 1996.

Wallace, J. M., and D. S. Gutzler, Teleconnections in the geopotential height field during the northern-hemisphere winter, *Mon. Weather Rev.*, *109*, 784–812, 1981.

Werne, J., Turbulent rotating Rayleigh-Benard convection (with comments on 2/7), course lecture, GFD Summer School, Woods Hole, Mass., 1995.

Whitehead, J. A., J. Marshall, and G. E. Hufford, Localized convection in rotating stratified fluid, *J. Geophys. Res.*, *101*(C10), 25,705–25,721, 1996.

Worcester, P. F., et al., Evolution of the large-scale temperature field in the Greenland Sea during 1988–89 from tomographic measurements, *Geophys. Res. Lett.*, *20*(20), 2211–2214, 1993.

Worthington, L. V., *On the North Atlantic Circulation*, 110 pp., Johns Hopkins Univ. Press, Baltimore, Md., 1976.

Wright, W. R., Northern sources of energy for the deep Atlantic, *Deep Sea Res.*, *19*, 865–877, 1972.

Yin, F. L., and E. S. Sarachik, An efficient convective adjustment scheme for ocean general circulation models, *J. Phys. Oceanogr.*, *24*, 1425–1430, 1994.

Zhang, J., R. W. Schmitt, and R. X. Huang, Sensitivity of GFDL Modular Ocean Model to the parameterization of double-diffusive processes, *J. Phys. Oceanogr.*, *28*, 589–605, 1998.

J. Marshall, Department of Earth, Atmospheric, and Planetary Sciences, Room 54-1524, Massachusetts Institute of Technology, Cambridge, MA 02139-4307. (marshall@gulf.mit.edu)

F. Schott, Institut für Meereskunde an der Universität Kiel, Düsternbrooker Weg 20, 24105 Kiel 1, Germany.